

TECHNISCHE UNIVERSITÄT MÜNCHEN

Lehrstuhl für Numerische Mechanik

Predictive Computational Modeling of Patient-Specific Cardiac Mechanics

Martin Rupert Pfaller

Vollständiger Abdruck der von der Fakultät für Maschinenwesen der Technischen Universität München zur Erlangung des akademischen Grades eines

Doktor-Ingenieurs (Dr.-Ing.)

genehmigten Dissertation.

Vorsitzender: Prof. Dr.-Ing. Boris Lohmann

Prüfer der Dissertation:

1. Prof. Dr.-Ing. Wolfgang A. Wall
2. Directeur de recherche Inria Dominique Chapelle, Ph.D.

Die Dissertation wurde am 15.11.2018 bei der Technischen Universität München eingereicht und durch die Fakultät für Maschinenwesen am 25.03.2019 angenommen.

Abstract

Diseases such as myocardial infarction can severely impair cardiac function. The resulting damage to the cardiac muscle is mostly permanent, as the heart's regenerative abilities are limited. However, in the surrounding myocardial tissue, infarction triggers many compensatory mechanisms characterized by growth and remodeling (G&R). Long-term prognosis of cardiac function would be a valuable tool in therapy planning, but a prediction by clinical measurements is currently not possible. Furthermore, the underlying G&R mechanisms are not fully understood. In the future, cardiac computer simulations could provide insights into G&R processes and predict a patient's response to specific therapies.

In this thesis, cardiac contraction is modeled as a structural elastodynamic initial boundary value problem formulated with large deformations, nonlinear hyperelastic anisotropic material, and active stress component. The structural model is monolithically coupled with a lumped-parameter Windkessel model of blood flow. The coupled model is solved with a high-performance parallel code using the Finite Element Method. A patient-specific four-chamber heart geometry is used, which is reconstructed from 3D magnetic resonance imaging (MRI).

The physiologically correct prediction of local stresses is essential for G&R of the heart. Boundary conditions, which are dictated by the pericardium on the outer surface of the heart, influence the contraction of the heart significantly. However, there is no consensus about physiologically correct and at the same time efficient pericardial boundary conditions. In this work, the performance of such pericardial boundary conditions is demonstrated and compared to the commonly used model of a fixed apex.

In a parameter study, the influence of the unknown pericardial stiffness is examined, and an optimal value is determined. The comparison of simulation results with measurements from Cine MRI showed that the use of pericardial boundary conditions gave a better prediction of the movement of the atrioventricular plane, atrial filling, and spatial approximation error. In contrast to the fixed apex model, when using pericardial boundary conditions, the stresses on the epicardium were consistent with measurements and evenly distributed.

Predictive cardiac models, such as the monolithically coupled structure-Windkessel model used in this work, require a large number of structural degrees of freedom. However, high computational demands slow model calibration and thus limit the use of cardiac simulations in clinical practice. Furthermore, for clinical questions, a large number of simulations with different parameter sets are often required, which is why a single solution is usually insufficient.

In this thesis, a novel approach to model order reduction is developed, which significantly speeds up the solution of the model. By projection into a low-dimensional subspace, only the structural dimension of the monolithically coupled structure-Windkessel system is reduced, using proper orthogonal decomposition. Also, various subspace interpolation methods are compared to integrate changes of the parameter set into the reduced model. The displacement field, as well as relevant scalar cardiac output quantities, were approximated well, even for varying parameter sets.

Finally, it is shown how parametric projection-based model order reduction can be easily integrated into gradient-based optimization using finite differences by approximating the gradients with a reduced order model. The performance of this method is investigated in a multivariate inverse analysis scenario. Compared to the standard approach of calculating the gradient with the

full order model, this approach enabled significantly shorter simulation times while maintaining approximation accuracy.

Zusammenfassung

Krankheiten wie beispielsweise Herzinfarkte können die Herzfunktion stark beeinträchtigen. Die dabei entstehende Schädigung des Herzmuskels ist meist dauerhaft, da die Fähigkeiten des Herzmuskelgewebes zur Regeneration begrenzt sind. Im umliegenden Herzmuskelgewebe löst der Myokardinfarkt jedoch eine Reihe von Kompensationsmechanismen aus, die durch Wachstum und Anpassung (engl. 'growth and remodeling', G&R) gekennzeichnet sind. Eine langfristige Prognose der Herzfunktion wäre ein wertvolles Instrument bei der Therapieplanung, jedoch ist eine Vorhersage durch klinische Messungen derzeit nicht möglich. Weiterhin sind die zugrunde liegenden G&R-Mechanismen nicht vollständig verstanden. In Zukunft könnten Computersimulationen des Herzens Erkenntnisse über G&R-Prozesse liefern und die Reaktion eines Patienten auf bestimmte Therapien vorhersagen.

In dieser Arbeit wird die Herzkontraktion als strukturelles elastodynamisches Anfangsrandwertproblem modelliert, das mit großen Deformationen, nichtlinearem hyperelastischem anisotropen Material und aktiver Spannungskomponente formuliert wird. Das Strukturmodell ist monolithisch mit einem dimensionsreduzierten Windkessel-Modell des Blutflusses gekoppelt. Das gekoppelte Modell wird in einem parallelen Hochleistungscode mithilfe der Finiten-Elemente-Methode gelöst. Hierbei wird eine patientenspezifische Vier-Kammer-Herzgeometrie verwendet, die aus 3D-Magnetresonanztomographie (MRT) rekonstruiert wird.

Die physiologisch korrekte Vorhersage lokaler Spannungen ist für G&R des Herzens essentiell. Randbedingungen, die durch das Perikard an der Außenfläche des Herzens vorgegeben sind, bestimmen die Herzkontraktion maßgeblich. Es besteht jedoch kein Konsens über physiologisch korrekte und gleichzeitig effiziente perikardiale Randbedingungen. In dieser Arbeit wird die Leistungsfähigkeit solcher perikardialen Randbedingung demonstriert und mit dem häufig verwendeten Modell eines fixierten Apex verglichen.

In einer Parameterstudie wird der Einfluss der unbekannt Perikardsteifigkeit untersucht und ein optimaler Wert ermittelt. Der Vergleich von Simulationsergebnissen mit Messungen aus Cine-MRT zeigte, dass die Verwendung von perikardialen Randbedingungen eine bessere Vorhersage hinsichtlich der Verschiebung der atrioventrikulären Ebene, der Vorhoffüllung und des räumlichen Approximationsfehlers ergab. Im Gegensatz zu dem Modell mit fixiertem Apex stimmten bei Verwendung von perikardialen Randbedingungen die auf das Epikard wirkenden Spannungen mit Messungen überein und waren gleichmäßig verteilt.

Prädiktive Herzmodelle, wie das in dieser Arbeit verwendete monolithisch gekoppelte Struktur-Windkessel Modell, erfordern eine Vielzahl struktureller Freiheitsgrade. Hohe Rechenanforderungen verlangsamten jedoch die Modellkalibrierung und erschweren daher die Verwendung von Herzsimulationen in der klinischen Praxis. Für klinische Fragestellungen werden auch häufig eine Vielzahl von Simulationen mit unterschiedlichen Parametersätzen benötigt, weswegen eine einzelne Lösung meist nicht ausreichend ist.

In dieser Arbeit wird deswegen ein neuartiger Ansatz zur Modellreduktion entwickelt, der die Lösung des Modells stark beschleunigt. Mittels Projektion in einen niederdimensionalen Unterraum wird nur die strukturelle Dimension des monolithisch gekoppelten Struktur-Windkessel-Systems durch Verwendung einer orthogonalen Zerlegung reduziert. Zusätzlich werden verschiedene Unterraum-Interpolationsmethoden verglichen, um Änderungen des Parametersatzes in das reduzierte Modell zu integrieren. Dabei wurden das Verschiebungsfeld sowie entscheidende skalare Ausgangsgrößen des Herzens gut angenähert, auch für variierende Parametersätze.

Abschließend wird gezeigt, wie parametrische projektionsbasierte Modellreduktion einfach in eine gradientenbasierte Optimierung mit finiten Differenzen integriert werden kann, indem die Gradienten mit einem dimensionsreduzierten Modell angenähert werden. Die Leistungsfähigkeit dieser Methode wird in einem multivariaten inversen Analyseszenario untersucht. Im Vergleich zum Standardansatz, die Gradienten mit dem vollen Modell zu berechnen, ermöglicht dieser Ansatz deutlich kürzere Simulationszeiten bei unveränderter Ergebnisqualität.

Acknowledgments

First of all, I would like to thank very warmly my Doktorvater Wolfgang A. Wall for sparking my interest in (computational) mechanics and especially biomechanics. He inspired me with his excitement for science and teaching and I thank him for his scientific integrity and for allowing me to learn from my own mistakes.

Another big thank you goes out to Cristóbal Bertoglio. Beyond his position as a Postdoc at LNM, he was always motivated to discuss all my major and minor issues with cardiac mechanics. His critical and pertinent remarks were important for continuously improving the quality of my work.

I extend my warmest thanks to Dominique Chapelle for agreeing to be my second examiner. His comprehensive expertise on all subjects covered in this thesis was a valuable resource for my research. His interest in my work is a special honor to me. I also thank Boris Lohmann for chairing my examining committee.

I thank my fellow *LNM heart group* members and office mates, Julia Hörmann and Andreas Nagler, for countless discussion on concerns of the heart. I have also received lots of valuable practical advice on coupled cardiac mechanics from Marc Hirschvogel at MHPC. I am grateful to have worked alongside Maria Cruz Varona, whose expertise on model order reduction combined with her interest in cardiac modeling proved to be a very inspiring collaboration. This work would not have been possible without the input by doctors and medical imaging. Here, I especially wish to thank Radomir Chabiniok and Eva Sammut for providing the cardiac MRIs I used throughout my work and displayed proudly on many occasions.

At LNM, I wish to thank all admins for their help in many Linux- or cluster-related emergencies. Lots of thanks also go out to all proof-readers of my thesis. I am thankful for having worked with many bright and talented students, whose own scientific work provided valuable contributions to this thesis.

I feel privileged having worked with many smart and interesting people in a very stimulating and positive environment at LNM. I am deeply thankful for the many friendships that started here. To just name a few: Alex, Andi, Birzly, Brändy, Bräumeister, Chris, Don Karlos, Foxy, Harry W, Jonas, JuJu, Julia, Creamy, Luca, Lukas, Maggy, Maxi, Schmidty, and Sweet Caroline. Special thanks go out to Andy, Dhruba, Hirschi, and Rui for countless *after-lunches* and *Männer-abende*, where essential matters of life were brought up for debate. Some of these friendships brought me to remote and exotic places like Abruzzo, East Belgium, West Bengal, North and South Tyrol, Giengen (an der Brenz), or the Oberpfalz. The availability of training partners for a variety of sports, hiking, swimming, running, climbing, road and mountain biking, (backcountry) skiing, or yoga, was always a welcome distraction from research. I also thank my fellow members of the *LNM Pro Racing Team* for many epic cycling adventures and for bringing the competitiveness of research to the road.

Last but not least, I thank Clemens Hoyos and Michael Schimpe for being there for me over the last decades. From the bottom of my heart, I would like to thank my family for their emotional support, without which this research project would have never been finished. Thank you, Gisela, Rupert, Sabine, Simone, and Thomas for lifting me up in moments of doubt.

Munich, April 2019

Martin R. Pfaller

Contents

1	Introduction	1
1.1	Motivation	1
1.2	Background	2
1.3	Research objective	4
1.3.1	Model accuracy	4
1.3.2	Computational efficiency	5
1.3.3	Model personalization	6
1.4	Contributions of this work	8
1.5	Outline	9
2	Cardiac mechanics	11
2.1	Continuum mechanics	11
2.1.1	Nonlinear kinematics	11
2.1.2	Stresses and constitutive behavior	13
2.1.3	Balance equations	14
2.1.4	Initial boundary value problem	15
2.2	Finite element method	15
2.2.1	Weak formulation	15
2.2.2	Discretization in space	16
2.2.3	Discretization in time	18
2.3	Geometrical models	18
2.3.1	Patient-specific four-chamber geometry	18
2.3.2	Generic prolate spheroid geometry	20
2.4	Modeling cardiac tissue	20
2.4.1	Local anisotropy	21
2.4.2	Passive behavior	25
2.4.3	Active behavior	27
2.4.4	Prestress	28
2.5	Modeling the circulatory system	29
2.6	Coupled structure-Windkessel system	31
3	Pericardial boundary conditions	35
3.1	The pericardium	35
3.1.1	Anatomy	35
3.1.2	Mechanical physiology	37
3.1.3	Current pericardial boundary conditions	39
3.2	Modeling the pericardium	39
3.3	Boundary condition cases	41

3.4	Numerical results with a prolate spheroid geometry	42
3.4.1	Model definition	42
3.4.2	End-systolic results	43
3.5	Numerical results with a patient-specific four-chamber geometry	44
3.5.1	Model definition	45
3.5.2	Assessment of cardiac function	45
3.5.3	Selection of pericardial parameters	48
3.5.4	Model personalization	52
3.5.5	Validation with cine MRI	53
3.6	Discussion	60
3.7	Conclusion	66
4	Model order reduction	67
4.1	Nonlinear parametric model order reduction by projection	67
4.1.1	Subspace projection	68
4.1.2	Cardiovascular reduced order model	70
4.1.3	Subspace computation via POD	71
4.2	Interpolation of subspaces	73
4.2.1	Weighted concatenation of bases	74
4.2.2	Weighted concatenation of snapshots	74
4.2.3	Adjusted direct basis interpolation	75
4.2.4	Basis interpolation on a Grassmannian manifold	76
4.3	Numerical results and discussion	77
4.3.1	Model definition	77
4.3.2	Implementation details	78
4.3.3	Model order reduction	80
4.3.4	Parametric model order reduction	85
4.4	Conclusion	90
5	Inverse analysis	91
5.1	Parameter identification based on reduced models	91
5.2	Numerical results and discussion	94
5.3	Conclusion	95
6	Summary and Outlook	99
A	Simulation parameters	105
A.1	Pericardial boundary conditions: Prolate spheroid geometry	105
A.2	Pericardial boundary conditions: Patient-specific four-chamber geometry	107
A.3	Model order reduction: Patient-specific four-chamber geometry	108
	Bibliography	111

Nomenclature

Mathematical operators and symbols

$\nabla_{\mathbf{X}}$	Material gradient
\det	Determinant
Div	Material divergence
$\delta(\bullet)$	Virtual quantity
\otimes	Dyadic product
\times	Cross product
$\ (\bullet)\ _2$	L_2 -norm
$\ (\bullet)\ _\infty$	Infinity norm
span	Linear span

Domains and boundaries

$\mathcal{B}_0, \mathcal{B}_t$	Reference (material) and current (spatial) configuration
$\partial\mathcal{B}_0, \partial\mathcal{B}_t$	Boundary in current and reference configuration
Γ_u	Dirichlet partition of boundary in reference configuration
Γ_σ	Neumann partition of boundary in reference configuration

Kinematics

\mathbf{X}	Position in reference configuration
\mathbf{x}	Position in current configuration
\mathbf{u}	Displacement
$\dot{\mathbf{u}}$	Velocity
$\ddot{\mathbf{u}}$	Acceleration
\mathbf{F}	Deformation gradient
J	Jacobian determinant, determinant of \mathbf{F}
V, v	Reference and current volume
A, a	Reference and current surface area
\mathbf{N}, \mathbf{n}	Unit normal vector in reference and current configuration
$\mathbf{R}, \mathbf{U}, \mathbf{v}$	Rotation tensor, material and spatial stretch tensors
\mathbf{C}	Right Cauchy-Green deformation tensor
$\mathbf{E}, \dot{\mathbf{E}}$	Green-Lagrange strain tensor and its rate

Stresses

T, t	Surface traction in reference and current configuration
σ	Cauchy stress tensor
P	First Piola-Kirchhoff stress tensor
S	Second Piola-Kirchhoff stress tensor
S_{visco}	Viscous stress
S_{act}	Active stress
S_{pass}	Passive stress

Constitutive laws

ψ	Strain energy density function
ψ_{NH}	Strain energy density function for isotropic Neo-Hooke material
ψ_{MR}	Strain energy density function for isotropic Mooney-Rivlin material
ψ_{exp}	Strain energy density function for anisotropic exponential material
$\psi_{\text{vol,a}}$	Strain energy density function for potential volumetric penalty
$\psi_{\text{vol,b}}$	Strain energy density function for quadratic volumetric penalty
ψ_{visco}	Viscous pseudo-potential
I_1, I_2	Invariants
\bar{I}_1, \bar{I}_2	Isochoric invariants
$I_{4,i}, I_{8,i}$	Anisotropic pseudo-invariants of constituent i
μ	Neo-Hooke stiffness parameter
C_1, C_2	Mooney-Rivlin stiffness parameters
a_i, b_i	Exponential material parameters of constituent i
κ	Volumetric penalty parameter
η	Viscosity

Initial boundary value problem

t	Time
T	Total simulation time
m	Mass
ρ_0	Reference mass density
$\hat{\mathbf{b}}_0$	Body force in reference configuration
$\hat{\mathbf{t}}_0$	Prescribed traction in reference configuration
$\hat{\mathbf{u}}$	Initial displacement at time $t = 0$
$\hat{\mathbf{v}}$	Initial velocity at time $t = 0$
\mathcal{W}	Work

Finite elements

n_{ele}	Number of elements
n_{nod}	Number of nodes
N_k	FE shape function of node k
ξ	Position in FE parameter space
\mathbf{X}, \mathbf{x}	Discrete nodal positions in reference and current configuration
\mathbf{d}	Discrete nodal displacements
\mathbf{v}	Discrete nodal velocities
\mathbf{a}	Discrete nodal accelerations
h	Characteristic element size
\mathbf{M}	Mass matrix
\mathbf{f}	Discrete force vector
\mathbf{K}	Tangential stiffness matrix

Time integration

Δt	Time step size
n	Time step index
\mathbf{d}_n	Discrete nodal displacements at time t_n
\mathbf{v}_n	Discrete nodal velocities at time t_n
\mathbf{a}_n	Discrete nodal accelerations at time t_n
γ, β	Parameters of Newmark's method
α_f, α_m	Parameters of generalized- α method
θ	Parameter of one-step- θ method

Active stress

τ	Active stress
u	Activation function
f	Systole indicator function
S	Sigmoid function
γ	Steepness parameter of sigmoid function
σ_0	Cardiac contractility
α_{max}	Myocyte binding rate
α_{min}	Myocyte unbinding rate
t_{sys}	Onset of systole
t_{dias}	Onset of diastole

Hemodynamics

p	Pressure
q	Flow
R	Resistance
C	Capacitance
L	Inertance
$(\bullet)_p$	Index proximal part
$(\bullet)_d$	Index distal part
R_{\max}	Maximum valve resistance
R_{\min}	Minimum valve resistance
R_{av}	Atrioventricular valve resistance
R_{sl}	Semilunar valve resistance

Pericardial boundary conditions

g	Gap function
W	Spring potential
k_a, c_a	Apical stiffness and viscosity
k_p, c_p	Pericardial stiffness and viscosity
k_v, c_v	Vessel attachment stiffness and viscosity
Γ_0^{apex}	Apical surface
Γ_0^{epi}	Epicardial surface
Γ_0^{vess}	Outsides of vessels surface
ϵ	Spatial error in Dice metric
$\bar{\mathbf{t}}_{\text{apex}}$	Mean apical stress vector
\bar{t}_{epi}	Mean scalar epicardial stress

Reduced order model

\mathbf{P}	Projector
\mathbf{x}_P	Projected point
q	Reduced dimension
\mathcal{V}, \mathcal{W}	Reduced-dimensional subspaces
\mathbf{V}, \mathbf{W}	Projection matrices
\mathbf{v}_i	Basis vector i
\mathbf{c}	Coefficient vector
e_P	Projection error
\mathbf{d}_r	Reduced discrete displacements
\mathbf{R}_r	Reduced discrete residual
\mathbf{K}_r	Reduced tangential stiffness matrix
n_p	Number of parameters
$\boldsymbol{\mu}$	Parameter set
$\epsilon_{\infty, \infty}$	Spatial approximation error
α	Reduced order model speedup

Proper orthogonal decomposition

n_s	Number of snapshots
\mathbf{D}	Snapshot matrix
\mathbf{U}	Matrix containing left singular vectors
$\boldsymbol{\Sigma}$	Matrix containing singular values
\mathbf{T}	Matrix containing right singular vectors
σ_i	Singular value i
\mathbf{u}_i	Left singular vector i
e	Cut-off approximation error

Inverse analysis

$\hat{\boldsymbol{\mu}}$	Optimal parameter set
S	Optimization objective function
\mathbf{r}	Optimization residual
\mathbf{J}	Optimization Jacobian
λ	Optimization damping parameter
β	Reduced order optimization speedup
t^i	Simulation time of method i
T^i	Optimization time of method i

Abbreviations

AVPD	Atrioventricular plane displacement
BACI	Bavarian advanced computational initiative
CoB	Concatenation of bases
CoS	Concatenation of snapshots
CPU	Central processing unit
CRT	Cardiac resynchronization therapy
DEIM	Discrete empirical interpolation method
DOF	Degree of freedom
ECSW	Energy conserving mesh sampling and weighting method
EF	Ejection fraction
FOM	Full order model
GB	Gigabyte
GMRES	Generalized minimal residual method
G&R	Growth and remodeling
LM	Levenberg-Marquardt algorithm
LV	Left ventricle
MAC	Modal assurance criterion
MI	Myocardial infarction
MOR	Model order reduction
MRI	Magnetic resonance imaging
pMOR	Parametric model order reduction
POD	Proper orthogonal decomposition
PTC	Pseudo-transient continuation
RAM	Random access memory
RIC	Relative information content
ROM	Reduced order model
RV	Right ventricle
SVD	Singular value decomposition
UKF	Unscented Kalman filter

1 Introduction

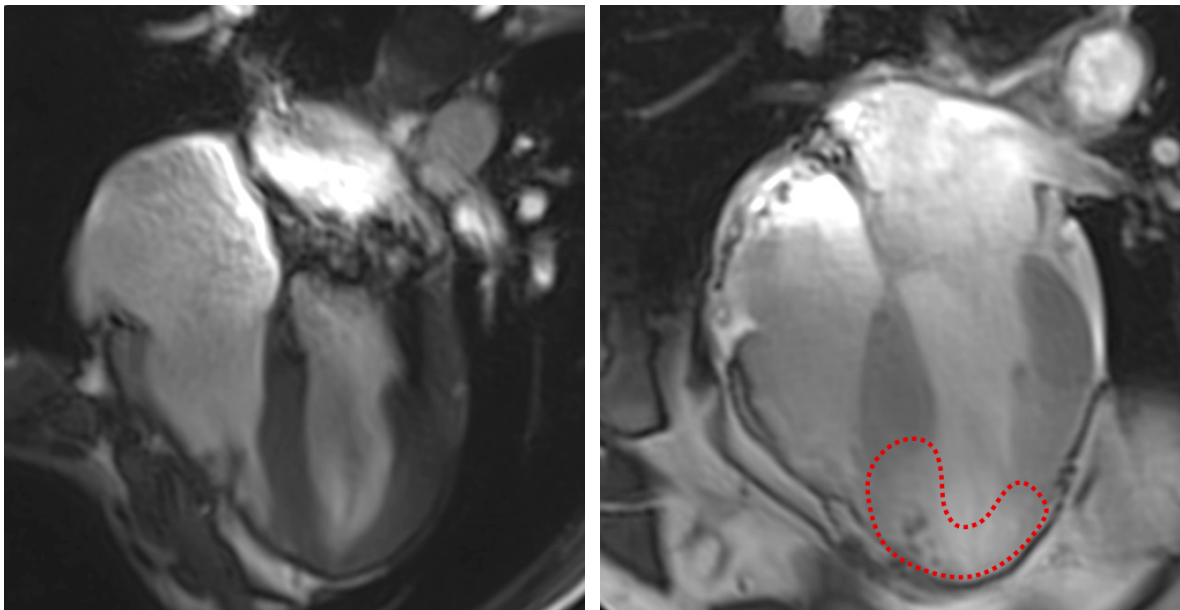
From a mechanical engineer's perspective, the human heart is nothing more than a pump, although a very sophisticated one. Over the lifetime of a 90-year-old human, it beats about three billion times and moves approximately 300 million liters of blood, ideally without external maintenance. If that pump ever fails it immediately threatens life. Computational modeling can be a valuable tool in predicting the heart's function to enable personalized therapies.

1.1 Motivation

Cardiovascular diseases are the leading cause of death in developed countries and increasingly so in developing countries, with more than seven million people each year diagnosed with myocardial infarction (MI), also called *heart attack* [184]. The heart requires a continuous supply with nutrients and oxygen, ensured by blood perfusion of the cardiac tissue. A severely perturbed or even blocked blood perfusion in parts of the cardiac tissue, for example, due to coronary artery disease, frequently results in MI. MI is visible in magnetic resonance imaging (MRI). By comparing a healthy heart to an infarcted heart in Figures 1.1a and 1.1b, respectively, the infarcted myocardium can be detected as the non-perfused region (dotted area in Figure 1.1b).

MI leads to tissue damage or tissue death, limiting the pumping function of the left ventricle of the heart and which may result in acute symptoms such as chest pain. The size of the compromised tissue depends on the severity of the blockage of the blood perfusion, the location of the blocked artery, and the time passed between MI and onset of therapy [175]. Initial treatments after MI is the reperfusion of occluded coronary arteries [164]. Secondary prevention commonly includes pharmaceutical agents such as aspirin, ACE inhibitors, or β -blockers, which are routinely administered following MI [154]. Tissue damage is partly permanent due to the limited regenerative capacity of the human myocardium [113], although the extent of cardiomyocyte replacement remains controversial [98]. New therapeutic approaches, such as stem cell therapy or tissue engineering, aim at remuscularizing the heart [112, 191]. Refractory heart failure can be treated by mechanical assist devices [18] or, as a last resort, heart transplantation [94].

Computer simulations of mechanical systems have been used in classical engineering disciplines, for example, car crash simulations, for decades. In this setting, computational models provide the opportunity to test designs virtually and lower the demand for expensive experiments. Virtual biophysical models of organs provide several opportunities to improve the current state of medicine. In a simulation of the organ's current state, clinical quantities of interest could be measured non-invasively. One example in this domain is obtaining pressure differences in coronary arteries through image-based modeling of blood flow instead of catheterization [174]. In surgical interventions, physicians only have one chance to choose the best procedure for a particular patient based on their individual experience. Here, computational simulations can support surgeons' decision making by exploring different variants of the surgical procedure without



(a) Healthy heart of a 24-year old.

(b) Heart of a 60-year old with myocardial infarction. The infarcted left-ventricular myocardium is visible due to a lack of blood perfusion (dotted area).

Figure 1.1: Two hearts at end-systole, taken from four-chamber cine magnetic resonance imaging. Images by C. Rischpler, Department of Nuclear Medicine, TUM.

harming the patient. For example, a catheter ablation strategy to treat atrial fibrillation can be chosen to maximize cardiac output after treatment [8, 92]. Another example is choosing the pacing site for cardiac resynchronization therapy (CRT) to optimize long-term cardiac output [161].

Computational models of cardiac mechanics with a timeframe of weeks or months could enable patient-specific therapies by *in silico* predicting the long-term response to therapies. An early identification of high-risk patients progressing to chronic heart failure is crucial for an appropriate treatment to reduce the likelihood of severe adverse cardiovascular events [172]. Clinical quantifiers of the progression of cardiac failure are left-ventricular end-systolic volume [183], infarct size [130], ejection fraction [58], and sphericity [189]. However, it is currently not possible to predict if and when an individual patient will progress to heart failure following MI [26]. As the underlying biological mechanisms following MI are still an open field of research, their computational modeling poses many challenges.

1.2 Background

Myocardial infarction (MI) triggers a series of compensatory events in myocardial tissue, many of which fall into the broad category of growth and remodeling (G&R), that is into growth, atrophy, and reorganization of the cardiac tissue. Cardiac G&R describes an adaptive process changing ventricular size, shape, constitution, and function as a response to tissue injury, driven by mechanical, neurohormonal, and genetic factors [149]. The structural changes primarily affect

the myocytes but also the coronary vasculature [40] and the extracellular matrix, i.e., interstitium, fibroblasts, and collagen.

Wound healing characterizes the initial response during the first days after MI [43]. The abrupt loss of contractile tissue, through necrosis and apoptosis of ischemic tissue, instantly decreases systolic ejection. An immediate consequence is infarct expansion [95]. That is, the myocardium starts to grow and remodel, which typically results in a regional dilation and thinning of the infarcted area [173], augmenting left ventricular end-diastolic volume [43]. The magnitude of dilation is positively correlated with infarct size [33], making timely reperfusion the primary therapeutic target [184]. The extracellular matrix forms a collagen scar around and inside the infarcted area, termed reparative fibrosis, after dead myocytes are removed by inflammatory cells [54]. This healing process is thought to be genetically controlled, whereas the orientation of newly deposited collagen fibers is related to the local mechanical conditions [43, 53].

Early ventricular G&R is adaptive and to some extent capable of stabilizing cardiac performance [39]. It primarily affects the spared, nonischemic myocardium and takes place during the weeks to months following MI. Eccentric hypertrophy, i.e., myocyte grow in length without an increase in wall thickness, in viable non-infarcted regions increases end-diastolic volume [173]. The heart can increase its stroke volume via the Frank-Starling mechanism [71], enhancing the contractility of non-infarcted myocardium and improving hemodynamic performance [130]. The stimuli for eccentric hypertrophy are however not identified yet [84].

Another early adaption is the remodeling, that is, reorganization, of the local myofiber architecture, commonly characterized by its fiber and sheet orientation [88]. The change in microstructure following MI has previously been assessed *ex vivo* in studies using diffusion-weighted magnetic resonance imaging and verified by histology [37, 131, 145, 190]. The findings of these studies are however conflicting, as they do not agree on how the microstructure changes following MI. In fact, in some studies, no significant fiber reorientation was found at all [180]. One possible reason for this inconclusiveness is measurement errors [23]. However, another probably even more critical problem is undoubtedly the cross-sectional design of the studies mentioned above where the cardiac tissue of different infarcted and non-infarcted animals was compared rather than the tissue of the same animals before and after infarction. There is a pressing need for new non-invasive longitudinal studies overcoming this deficiency and finally settling the question of fiber reorientation after MI satisfactorily.

In many patients, G&R advance beyond this compensatory stage, eventually progressing to chronic heart failure [78]. This process has been called adverse or pathological G&R. Laplace's law states that circumferential wall stress is proportional to both left ventricular pressure and radius and inversely proportional to wall thickness [69]. Following dilation and thinning of the infarct zone [176], systolic and diastolic circumferential wall stress in non-infarcted myocardium thus increase significantly [142]. Pressure overload and elevated wall stress trigger concentric hypertrophy, i.e., myocyte widening with an increase in wall thickness [105]. The systolic shape of the left ventricle changes from elliptical to spherical [40] while increasing its mass [69]. The adaption capabilities of the heart via the Frank-Starling mechanism are exhausted [104]. Hypertrophied infarcted tissue inhibits reactive fibrosis, increasing the concentration of very rigid collagen fibers [54]. The newly deposited collagen stiffens the myocardium and increases diastolic pressure. Furthermore, it transforms the cardiac tissue to a mechanically and electrically heterogeneous compound, promoting arrhythmogenesis [13]. During adverse remodeling, the heart does not converge to an adapted equilibrium state. Instead, it forms a vicious cycle of

progressing hypertrophy, increasing wall stress, and interstitial fibrosis [122]. These mechanisms send the heart into a downwards spiral of progressively increasing ventricular volume and mass and decreasing contractility, finally resulting in chronic heart failure [78].

Summarizing, MI can be considered a perturbation of the cardiac tissue's balanced, healthy state. MI is followed by scarring and fibrosis as immediate emergency repair mechanisms. Subsequently, a mixture of wall dilatation and eccentric and concentric hypertrophy is observed, increasing both the volume and wall thickness of the left ventricle. While in some instances this growth process can recover a new equilibrium, in others maladaptation is observed, i.e., a continued increase of volume and wall thickness. A comprehensive theory that explains under which conditions G&R after MI becomes unstable and how it could be stabilized remains pending to date. However, current models of cardiac mechanics lack several key properties to make research of cardiac G&R accessible.

1.3 Research objective

With post-infarction growth and remodeling (G&R) identified as a major research objective of computational cardiac models, several key model requirements need to be fulfilled. As outlined above, G&R crucially depends on the local mechanical stress state within the myocardium. A cardiac model thus needs to predict not only kinematics but also the internal stress state with sufficient accuracy. An important prerequisite for that are physiological boundary conditions. Furthermore, tools for fast approximated model evaluation need to be available during model development. Finally, an inverse analysis framework is required for personalization of patient-specific cardiac models. The tools proposed in the following lay the groundwork for future studies of cardiac G&R.

Parts of this section were submitted for publication in [147, 148].

1.3.1 Model accuracy

Cardiac mechanics simulations consist of solving a nonlinear elastodynamic boundary value problem [156]. Physiological boundary conditions are essential to achieve predictive results for any clinical purposes. The boundary conditions on the structure field of the myocardium are mainly governed by two physiological aspects: Blood flow within the chambers near the inside surface of the myocardium (*endocardium*) and the pericardial sac on the outside surface (*epicardium*). There are many applications for simulating heart blood flow [46]. However, for many relevant questions the exact fluid dynamics of blood within the heart or a resolved fluid-solid interaction simulation are not needed for simulating the myocardium. Instead, a realistic pressure-flow relationship stemming from the circulatory system is sufficient, which is commonly represented by lumped-parameter fluid models that provide the correct normal pressure to the endocardial wall [100].

However, there is no consensus on boundary conditions to represent the effects of the pericardial sac. The goal of this work is thus twofold: (a) provide a detailed literature review of pericardial biomechanics, hence justifying its modeling using a computationally inexpensive viscoelastic model, and (b) highlight the relevance of such boundary conditions through a de-

tailed quantitative analysis using a subject-specific cine MRI data set. For that purpose, a four-chamber cardiac geometry including parts of the great vessels is employed, as it provides several options to assess the physiological accuracy of the pericardial boundary condition, e.g. through the interplay between ventricles and atria during ventricular systole. Note that the pericardial boundary condition is independent of the geometry and is meant to be applied to any kind of cardiac mechanics simulation that includes the epicardial surface.

1.3.2 Computational efficiency

Predicting patient-specific G&R requires a fine spatial resolution of the cardiac model, as the cardiac tissue following myocardial infarction is very heterogeneous and G&R describes a local effect on the cell-scale. However, the needed huge number of degrees of freedom (DOFs) make the solution of cardiac models computationally expensive and limit the models' use in clinical practice. As an example, the high-fidelity four-chamber model proposed in this thesis was run on a single node of a Linux cluster with two Intel Xeon E5-2680 *Haswell* processors, equipped with 12 cores and 64 GB of RAM. A simulation of one heartbeat, which takes about one second in reality, took about one day to compute. The potential to reduce computation time motivates the use of reduced order models (ROMs). In this work, we solely consider model order reduction (MOR) of time-dependent parametric problems. In the following, different strategies in reduced order modeling are reviewed.

An important category of cardiac ROMs is made up by simplified modeling. For these models, the same system of differential equations as for the full order model (FOM) is solved, but on a simplified analytical geometry. The displacements are commonly parameterized by only one scalar degree of freedom (DOF). These models are thus referred to as 0D models. Examples in this category include monoventricular cylindrical [5], spherical [29], or prolate spheroid [136] or biventricular [123] geometries. These models allow extremely fast evaluation, with computation times well below one second. Their results are, however, only lumped quantities which usually need an extra correction step in order to predict the solution of a corresponding patient-specific 3D model.

Another approach of model order reduction (MOR) in biomechanics is the use of coarsely discretized geometries, see e.g. [17, 83]. Coarsely discretized models are easy to implement, since the computational framework is identical to the one of the FOM. The disadvantage of using coarsely discretized geometries is that there is no exact control over the approximation quality and important features of the FOM might not be preserved by the ROM.

A third category of cardiac ROMs makes a model computationally less expensive by reducing the dimension of the problem, starting from the FOM. These ROMs make a model computationally less expensive by reducing the dimension of the problem, starting from the FOM. For example in cardiac electrophysiology, approximated Lax pairs for propagating wave fronts were proposed in [63, 64]. A local reduced basis method for parameterized cardiac electrophysiology was recently introduced in [143]. Reduced basis methods were proposed for general large deformation, material nonlinear finite element simulations [108, 132]. A framework for linear coupled multiphysics problems was introduced in [159].

Using the group's code [181], for a large-scale cardiac finite element simulation, about 90 % of the time is spent iteratively solving linear systems of equations. This proportion motivates the use of MOR by projection, where the full linear system is projected onto a much smaller dimen-

sional subspace while preserving the model's most relevant features. The solution of the FOM is then approximated by a solution in the reduced space with a ROM. A popular method to generate such subspaces is proper orthogonal decomposition (POD), which is purely observation-based and independent of the underlying physics of the model. The snapshots are here transient observations of displacements. They can be obtained from a FOM simulation of one heartbeat.

There are only few examples where POD has been applied to cardiac problems. A quasi-static cardiac model was reduced using POD and combined with hyper-reduction techniques in [21]. However, analysis was only carried out using an idealized ellipsoidal left ventricular geometry with few DOFs. While this is very instructive, results for speedup and accuracy of the ROM are not conclusive for real-world cardiac problems. The reduction of a patient-specific biventricular cardiac model using POD is described in [31]. Here, a general approach is presented and analysed mathematically, before being applied to the example of a patient-specific beating heart model. Parameter estimation is performed based on medical images. A ROM of blood dynamics in coronary arteries is used in [12].

Cardiac models rely on a large set of patient-specific parameters, describing constitutive behavior, hemodynamics, boundary conditions, or local fiber orientation. In order not to rely on a FOM simulation for each new ROM simulation, which would render the ROM simulation useless, the reduced subspace must be able to adapt to a changing parameter set. This adaption requires parametric model order reduction (pMOR) of the time-dependent problem. Among many global and local pMOR techniques, various subspace interpolation methods have been proposed in the past [14]. Specifically, a popular method using a Grassmann manifold was proposed in [4] and illustrated with a large coupled aeroelastic model of a fighter jet. The method proposed in [31] uses a so-called "multi-POD" approach. A parameter-weighted variant of this approach is also used in this work and described in Section 4.2.2 as weighted concatenation of snapshots method. Furthermore, a global pMOR approach using a global basis over the whole parameter range is employed in [21].

The performance of POD in realistic coupled simulations of cardiac contraction is yet unknown. In this thesis, the performance of POD is demonstrated and applied to a patient-specific cardiac geometry with about 850'000 structural DOFs. POD for large nonlinear models has only been applied to single fields, e.g. structural mechanics or fluid dynamics, separately [51]. In this work, the case of a POD-reduced 3D structural model that is monolithically coupled to a 0D Windkessel model is considered. Only the structural dimension of the problem is reduced. Additionally, several subspace interpolation methods are reviewed for cardiac problems. In these parametric simulations, the contractility parameter controlling maximum active tension of the myofibers is varied in the cardiac model, as it has been shown to be the most influential parameter for cardiac function and commonly calibrated to experiments.

1.3.3 Model personalization

Many of the cardiac model parameters depend on a patient's physiology and are *a priori* unknown, as invasive experiments cannot be carried out on living human subjects. A predictive patient-specific cardiac model is thus subject to an iterative process termed *inverse analysis*. In this context, the simulation of one heartbeat with given parameters can be regarded as the forward problem. The reverted task of matching the parameters to given observations from the patient-specific heartbeat is then the inverse problem. Common clinical measurements of car-

diac kinematics are displacement data extracted from cine or tagged magnetic resonance imaging (MRI), representing an Eulerian and Lagrangian description of motion, respectively. Other measurements include blood pressure or electrocardiograms. As cardiac mechanics simulations pose an expensive forward problem, repeated evaluation during inverse analysis has incredible computational demands. Furthermore, algorithms for inverse analysis commonly scale linearly with the number of parameters. Using reduced order modeling during inverse analysis might thus lead to significant time savings.

During gradient-based optimization, the adjoint method offers computationally inexpensive gradient calculation when combining it with advanced methods such as automatic differentiation and checkpointing [74]. For example in [160], regional contractility was estimated from short axis cine MRI. Using the adjoint method, ischemic regions in cardiac electrophysiology were identified in [36]. Most recently in [52], passive material parameters and active fiber shortening was estimated for a biventricular geometry from ventricular volume and regional strain.

Gradient-free inverse analysis for cardiac problems was demonstrated in [30], where regional cardiac contractility was estimated from cine MRI using the unscented Kalman filter (UKF). The reduced order UKF was further applied in [15, 133] to estimate boundary condition parameters of the aorta for a fluid-structure-interaction problem. Other examples of gradient-free inverse analysis include [9], where left-ventricular active and passive material parameters were estimated from 3D tagged MRI using a parameter sweep.

A good overview of using pMOR for inverse analysis is given in [14] and [146]. One example is to optimize over the ROM within a regularly updated trust region around the FOM, see e.g. [193]. There are some examples where reduced order modeling has been combined with inverse analysis in biomechanics. For arterial hemodynamic fluid-structure-interaction problems, an inverse analysis with uncertainty quantification was performed in [115] using a reduced basis method. There are however few references for cardiac solid models. In [31], the reduced order UKF was applied to estimate cardiac contractility in a healthy and an infarcted region. The forward simulations were carried out using POD, thus converging to a different solution than using the FOM only. In [83] a multifidelity approach was proposed to calibrate hemodynamical and structural parameters of a cardiac model to ventricular pressure measurements. Here, a Levenberg-Marquardt-based optimization uses evaluations switching between a 3D FOM, a coarsely discretized version of the 3D FOM, and a 2D surrogate model. Another multifidelity approach was used in [135] between a 3D FOM and a 0D surrogate model. An evolutionary algorithm was used in [22] using a ROM with a pre-computed POD-basis from a single FOM to identify four parameters of an electrophysiological cardiac model from a synthetic electrocardiogram. As in [31], a reduced order UKF was used in [41] to estimate parameters of a one-way coupled electromechanical cardiac model from synthetic data. Here, as well, a POD basis was constructed *a priori* from, in this case, four pre-computed parameter sample sets.

Using coarsely discretized or surrogate models does however not guarantee that the most important features of the FOM are preserved. These surrogate models further lack the ability of pMOR to inherently *learn* from evaluations of the FOM to become more precise throughout the optimization. Instead, they require an additional mapping between FOM and surrogate model solutions. Most importantly, using 2D or 0D surrogate models during inverse analysis, the heart can only be tuned to scalar measurements. However, a calibration to spatial measurements from cine or tagged MRI might be desired in many applications, e.g. when detecting infarcted regions [30]. Furthermore, an *a priori* generation of the ROM might not be suitable for non-convex ap-

proximation problems with several parameters as it is computationally expensive and the parameter range might not be known *a priori*. In this thesis, a novel method of how an automatically updated ROM can be integrated into any optimization-based inverse analysis is proposed. This method leads to considerable savings in computation time and its performance is demonstrated in a real-world multivariate inverse analysis scenario.

1.4 Contributions of this work

With important requirements to study cardiac G&R outlined above, the contributions of this thesis are summarized in the following.

- **Physiological and efficient pericardial boundary conditions**

Physiological boundary conditions are essential for the predictive capabilities of any cardiac model. On the heart's inside, blood pressure is acting on the myocardium. The heart itself is contained within an enclosing sac, the pericardium. Except for the work of [56], there are no studies of pericardial-myocardial interaction. However, the pericardium in [56] was modeled by a contact-interaction problem, rendering the imposition of pericardial boundary conditions computationally expensive. This thesis demonstrates the good performance of a simplified pericardial model through a comprehensive quantitative comparison of simulation results from a patient-specific four-chamber cardiac model to cine magnetic resonance data.

- **Coupled nonlinear model order reduction**

Cardiac contraction is commonly simulated with parametric, highly dimensional, large deformation, nonlinear models. These models are computationally expensive, limiting their use in clinical practice and slowing model personalization. Several approaches for cardiac model order reduction have been proposed. However, past studies are either not applicable to real-world patient-specific models, do not feature a performance comparison of reduction methods, or consider purely structural models. This thesis proposes to reduce the structural model of a monolithically coupled structure-Windkessel cardiac model using projection-based model order reduction with proper orthogonal decomposition. The reduced order model is solved in a parallel high performance computing framework. This approach offers considerable computational speedup while maintaining approximation accuracy. Furthermore, several subspace interpolation methods are reviewed for parametric solutions of the cardiac model.

- **Speedup of gradient-based inverse analysis**

Inverse analysis is crucial for cardiac modeling to personalize model parameters to given experimental data. Gradient-based methods are commonly used to solve the arising optimization problem. Gradients are commonly calculated using finite differences. However, this strategy is computationally expensive, scaling with the number of parameters. In this thesis, a simple method is proposed to use parametric reduced order models to calculate gradients, based on knowledge of prior optimization iterations. It is shown that approximation quality is comparable to a standard gradient-based optimization while significantly reducing simulation time.

1.5 Outline

The tools for predictive patient-specific cardiac modeling are organized in the following, self-contained chapters, each demonstrated by individual numerical examples. The remainder of this thesis is structured as follows.

Chapter 2 describes all components of a computational cardiac solid mechanics model. The general set of governing partial differential equations is introduced, using a large-deformation nonlinear continuum mechanics framework. The solution using the finite element method is briefly outlined in the following. Specifically for cardiac problems, the geometries, materials, and circulatory system are explained, leading, finally, to the monolithically coupled structure-Windkessel model used throughout this thesis.

Diving into biological details of the heart's interaction with its surrounding organs, **Chapter 3** offers a thorough analysis of pericardial boundary conditions. Following analysis of the anatomical and physiological background, current pericardial boundary conditions are reviewed. Using a four-chamber patient-specific geometry, different models of pericardial-myocardial interaction are quantitatively compared to multi-view patient-specific cine MRI and their implication on the contractile motion of the heart is analyzed.

With computation time identified as a major inconvenience of high-fidelity cardiac simulations, a model order reduction strategy is proposed in **Chapter 4** for the monolithically coupled structure-Windkessel model, based on proper orthogonal decomposition. To enable parametric dependence in reduced order models, several subspace interpolation methods are reviewed. The performance of model order reduction is demonstrated in a real-world setting, for both constant and variable parameter sets.

The use of the reduced order model from Chapter 4 in an inverse-analysis scenario is briefly outlined in **Chapter 5**. Here, a simple but effective method is proposed how parametric reduced order modeling can be incorporated into gradient-based inverse analysis using finite differences. The performance of the method is demonstrated using synthetic data.

The conclusion in **Chapter 6** summarizes the methods proposed in this thesis for cardiac modeling. Furthermore, objectives for future research towards cardiac growth and remodeling are given.

2 Cardiac mechanics

This chapter is concerned with the derivation of a mathematical and computational cardiac model used throughout this thesis. Section 2.1 introduces the set of differential equations needed to describe the cardiac motion as an elastodynamic problem in a material nonlinear framework capable of large deformations. These equations are numerically solved by the finite element method briefly outlined in Section 2.2. Moving from a general framework to cardiac-specific models, two cardiac geometries are introduced in Section 2.3, along with cardiac material definitions in Section 2.4. Ventricular pressures within the heart caused by blood flow are approximated by a lumped-parameter model of the circulatory system described in Section 2.5. Finally, the coupled system is presented in Section 2.6.

2.1 Continuum mechanics

This section contains a summary of the governing equations of continuum mechanics relevant for this work. For more details, refer to [19, 87]. Let $\mathcal{B}_0 \in \mathbb{R}^3$ denote the material or reference configuration of a continuous body with particle positions \mathbf{X} at time $t = 0$. The deformation of the body is expressed by the mapping function φ in Lagrangean description. It maps the material position \mathbf{X} in reference configuration to the spatial position \mathbf{x} within the spatial or current configuration \mathcal{B}_t for all times $t \in \mathbb{R}_+$,

$$\varphi(\mathbf{X}, t) = \begin{cases} \mathcal{B}_0 \rightarrow \mathcal{B}_t, \\ \mathbf{X} \mapsto \mathbf{x}(\mathbf{X}, t). \end{cases} \quad (2.1)$$

The finite displacement field

$$\mathbf{u}(\mathbf{X}, t) = \mathbf{x}(\mathbf{X}, t) - \mathbf{X} \quad (2.2)$$

links both configurations. The first and second time derivatives of the displacement vector are the velocities $\dot{\mathbf{u}}(\mathbf{X}, t)$ and accelerations $\ddot{\mathbf{u}}(\mathbf{X}, t)$ defined as

$$\dot{\mathbf{u}}(\mathbf{X}, t) = \left. \frac{\partial \mathbf{u}(\mathbf{X}, t)}{\partial t} \right|_{\mathbf{X}} = \frac{d\mathbf{u}(\mathbf{X}, t)}{dt}, \quad (2.3)$$

$$\ddot{\mathbf{u}}(\mathbf{X}, t) = \left. \frac{\partial^2 \mathbf{u}(\mathbf{X}, t)}{\partial^2 t} \right|_{\mathbf{X}} = \frac{d\dot{\mathbf{u}}(\mathbf{X}, t)}{dt} = \frac{d^2 \mathbf{u}(\mathbf{X}, t)}{d^2 t}. \quad (2.4)$$

2.1.1 Nonlinear kinematics

The deformation gradient \mathbf{F} is the material gradient of the deformation mapping

$$\mathbf{F}(\mathbf{X}, t) = \nabla_{\mathbf{X}} \varphi(\mathbf{X}, t) = \frac{d\mathbf{x}(\mathbf{X}, t)}{d\mathbf{X}}. \quad (2.5)$$

For simplicity of notation, in the following, the dependence of kinematic quantities on time t is dropped. The deformation gradient allows to map between basis vectors in reference and current configuration. It is a mixed tensor as its first and second basis vector are from the tangential spaces of the current and reference configuration, respectively. An infinitesimal line segment $d\mathbf{X} \in \mathcal{B}_0$ in reference configuration is mapped to a line segment $d\mathbf{x} \in \mathcal{B}_t$ in material configuration using the deformation gradient

$$d\mathbf{x} = \mathbf{F} \cdot d\mathbf{X}, \quad (2.6)$$

termed *push-forward* operation. The inverse *pull-back* operation is

$$d\mathbf{X} = \mathbf{F}^{-1} \cdot d\mathbf{x}. \quad (2.7)$$

The determinant J of the deformation gradient,

$$J = \det \mathbf{F} > 0, \quad (2.8)$$

is always positive and is a measure for the change of infinitesimal volume elements

$$dv = J dV, \quad (2.9)$$

where dv and dV are the infinitesimal volume element in current and reference configuration, respectively. The deformation gradient can be multiplicatively decomposed in an isotropic, shape-preserving part \mathbf{F}_{vol} , and an isochoric, volume-preserving part $\bar{\mathbf{F}}$, as follows

$$\mathbf{F} = \mathbf{F}_{\text{vol}} \cdot \bar{\mathbf{F}}, \quad \text{with} \quad \mathbf{F}_{\text{vol}} = J^{\frac{1}{3}} \mathbf{I} \quad \text{and} \quad \bar{\mathbf{F}} = J^{-\frac{1}{3}} \mathbf{F}, \quad (2.10)$$

with identity matrix \mathbf{I} . The relationship between infinitesimal area elements $d\mathbf{a}$ and $d\mathbf{A}$ in current and reference configuration, respectively, is Nanson's formula

$$d\mathbf{a} = J\mathbf{F}^{-\text{T}} \cdot d\mathbf{A}. \quad (2.11)$$

Using the polar decomposition theorem, the deformation gradient can be uniquely right or left decomposed as

$$\mathbf{F} = \mathbf{R} \cdot \mathbf{U} = \mathbf{v} \cdot \mathbf{R}, \quad (2.12)$$

with rigid body rotation tensor \mathbf{R} and the symmetric and positive definite stretch tensors \mathbf{U} and \mathbf{v} in reference and current configuration, respectively. Due to the mixed-basis nature and the lack of rotational invariance of the deformation gradient, the right Cauchy-Green deformation tensor \mathbf{C} is widely used instead:

$$\mathbf{C} = \mathbf{F}^{\text{T}} \cdot \mathbf{F} = \mathbf{U}^{\text{T}} \cdot \mathbf{R}^{\text{T}} \cdot \mathbf{R} \cdot \mathbf{U} = \mathbf{U}^{\text{T}} \cdot \mathbf{U}, \quad (2.13)$$

where the orthogonality of the rotation tensor has been used. The right Cauchy-Green tensor is defined in reference configuration and invariant with respect to rigid body motion. A common strain measure defined in reference configuration is the Green-Lagrange strain tensor

$$\mathbf{E} = \frac{1}{2} (\mathbf{F}^{\text{T}} \cdot \mathbf{F} - \mathbf{I}) = \frac{1}{2} (\mathbf{C} - \mathbf{I}), \quad (2.14)$$

which, in contrast to the right Cauchy-Green tensor, is zero in the absence of deformation. The rate of the Green-Lagrange strain tensor is

$$\dot{\mathbf{E}} = \frac{1}{2} (\dot{\mathbf{F}}^{\text{T}} \cdot \mathbf{F} + \mathbf{F}^{\text{T}} \cdot \dot{\mathbf{F}}). \quad (2.15)$$

2.1.2 Stresses and constitutive behavior

The current surface traction \mathbf{t} is defined as the resulting force $\Delta \mathbf{f}$ on a vanishing surface area Δa in current configuration

$$\mathbf{t} = \lim_{\Delta a \rightarrow 0} \frac{\Delta \mathbf{f}}{\Delta a}. \quad (2.16)$$

Using the surface traction \mathbf{t} and the current outward unit normal \mathbf{n} , the Cauchy stress tensor $\boldsymbol{\sigma}$ can be derived, for which holds

$$\mathbf{t} = \boldsymbol{\sigma} \cdot \mathbf{n}. \quad (2.17)$$

The Cauchy stress tensor is defined with respect to the current basis vectors. The first Piola-Kirchhoff stress tensor \mathbf{P} is obtained from the Cauchy stress tensor by a pull-back operation of the second basis vector

$$\mathbf{P} = J \boldsymbol{\sigma} \cdot \mathbf{F}^{-\top}. \quad (2.18)$$

The second Piola-Kirchhoff stress tensor \mathbf{S} is obtained by an additional pull-back of the first basis vector

$$\mathbf{S} = \mathbf{F}^{-1} \cdot \mathbf{P} = J \mathbf{F}^{-1} \cdot \boldsymbol{\sigma} \cdot \mathbf{F}^{-\top}. \quad (2.19)$$

The surface traction \mathbf{T} in reference configuration is then calculated as

$$\mathbf{T} = \mathbf{S} \cdot \mathbf{N}, \quad (2.20)$$

with outward unit reference normal \mathbf{N} . Hyperelastic materials can be modeled with a strain energy density function ψ , also called hyperelastic potential. Material behavior depends only on the current deformation and not on deformation history. The strain energy density function is invariant to rigid body rotations \mathbf{R} of the deformation gradient and depends on the deformation gradient \mathbf{F} or any derived quantities, e.g. stretch tensor \mathbf{U} , right Cauchy-Green tensor \mathbf{C} , or Green-Lagrange strains \mathbf{E} . The second Piola-Kirchhoff stress can be directly calculated from the potential ψ as

$$\mathbf{S} = 2 \frac{\partial \psi}{\partial \mathbf{C}} = \frac{\partial \psi}{\partial \mathbf{E}}. \quad (2.21)$$

Analog to the hyperelastic potential ψ in (2.21), a viscous pseudo-potential ψ_{visco} is defined to calculate the viscous stress

$$\mathbf{S}_{\text{visco}} = \frac{\partial \psi_{\text{visco}}}{\partial \dot{\mathbf{E}}} \quad (2.22)$$

depending on the rate of the Green-Lagrange strain tensor $\dot{\mathbf{E}}$. Note that this is not a physical principle but rather a computational convenience, since no potential can be given for dissipation processes. Specific constitutive models for cardiac tissue are given in Section 2.4.

2.1.3 Balance equations

Conservation of mass In classical elastodynamics, i.e., without growth or remodeling, the mass of the body is conserved. This yields in reference configuration

$$\frac{dm}{dt} = \frac{d}{dt} \int_{\mathcal{B}_0} \rho_0 dV = \int_{\mathcal{B}_0} \dot{\rho}_0 dV = 0, \quad (2.23)$$

and thus in local form $\dot{\rho}_0 = 0$. Using Reynold's transport theorem, the conservation of mass can equivalently be formulated in current configuration, refer to [19, 87].

Balance of linear momentum The balance of linear momentum states that the change in linear momentum must equal all external forces acting on the body

$$\frac{d}{dt} \int_{\mathcal{B}_0} \rho_0 \dot{\mathbf{u}} dV = \int_{\mathcal{B}_0} \hat{\mathbf{b}}_0 dV + \int_{\partial\mathcal{B}_0} \hat{\mathbf{t}}_0 dA, \quad (2.24)$$

with external surface traction $\hat{\mathbf{t}}_0$ acting on the reference boundary $\partial\mathcal{B}_0$. This expression can be simplified to

$$\int_{\mathcal{B}_0} \rho_0 \ddot{\mathbf{u}} dV = \int_{\mathcal{B}_0} (\text{Div } \mathbf{P} + \hat{\mathbf{b}}_0) dV, \quad (2.25)$$

with volume forces $\hat{\mathbf{b}}_0$ per reference unit volume. The local form of the balance of linear momentum in reference configuration yields

$$\rho_0 \ddot{\mathbf{u}} = \text{Div } \mathbf{P} + \hat{\mathbf{b}}_0. \quad (2.26)$$

This expression is also known as Cauchy's first law of motion.

Balance of angular momentum The balance of angular momentum states that the change in angular momentum must equal all external moments acting on the body and yields in reference configuration

$$\frac{d}{dt} \int_{\mathcal{B}_0} (\rho_0 \mathbf{x} \times \dot{\mathbf{u}}) dV = \int_{\mathcal{B}_0} (\mathbf{x} \times \hat{\mathbf{b}}_0) dV + \int_{\partial\mathcal{B}_0} (\mathbf{x} \times \hat{\mathbf{t}}_0) dA. \quad (2.27)$$

Analog to the balance of linear momentum, these formulations can be simplified by applying the Gauss-Green divergence theorem to the boundary integrals. It can be shown that the balance of angular momentum in current and reference configuration lead to the requirement that the Cauchy stress $\boldsymbol{\sigma}$ and the second Piola-Kirchhoff stress \mathbf{S} must be symmetric:

$$\boldsymbol{\sigma}^T = \boldsymbol{\sigma}, \quad \mathbf{S}^T = \mathbf{S}. \quad (2.28)$$

This expression is also known as Cauchy's second law of motion.

2.1.4 Initial boundary value problem

The Dirichlet and Neumann boundaries in reference configuration Γ_u and Γ_σ , respectively, are disjunct sets and together form the boundary $\partial\Omega$ of the domain in reference configuration Ω :

$$\Omega = \mathcal{B}_0, \quad \partial\Omega = \Gamma_u \cup \Gamma_\sigma, \quad \Gamma_u \cap \Gamma_\sigma = \emptyset \quad (2.29)$$

Using the balance of linear momentum (2.26) together with prescribed displacements $\hat{\mathbf{u}}$ on the Dirichlet boundary Γ_u and prescribed tractions $\hat{\mathbf{t}}_0$ on the Neumann boundary Γ_σ yields

$$\text{Div } \mathbf{P} + \hat{\mathbf{b}}_0 = \rho_0 \ddot{\mathbf{u}} \quad \text{in } \Omega \times [0, T], \quad (2.30)$$

$$\mathbf{u} = \hat{\mathbf{u}} \quad \text{on } \Gamma_u \times [0, T], \quad (2.31)$$

$$\mathbf{P} \cdot \mathbf{N} = \hat{\mathbf{t}}_0 \quad \text{on } \Gamma_\sigma \times [0, T], \quad (2.32)$$

$$\mathbf{u}(\mathbf{X}, 0) = \hat{\mathbf{u}}_0(\mathbf{X}) \quad \text{in } \Omega, \quad (2.33)$$

$$\dot{\mathbf{u}}(\mathbf{X}, 0) = \hat{\mathbf{u}}_0(\mathbf{X}) \quad \text{in } \Omega, \quad (2.34)$$

which is the strong formulation of the initial boundary value problem (IBVP) since the equation holds for every material point \mathbf{X} in reference configuration. The IBVP is solved for all times t between the initial time 0 and the final time T . Initial conditions (2.33) and (2.34) are prescribed at $t = 0$ with initial displacements $\hat{\mathbf{u}}_0$ and initial velocities $\hat{\mathbf{u}}_0$.

2.2 Finite element method

The set of nonlinear partial differential equations forming the IBVP given in Section 2.1.4 is solved using the finite element method. All derivations in this section will be given with respect to the geometry in reference configuration Ω , as it corresponds to the implementation used in this work. However, all derivations could equally be carried out in current configuration. Again, this section only contains relevant equations used in this thesis. For a comprehensive discussion, see for example [19].

2.2.1 Weak formulation

The balance of momentum (2.30) and Neumann boundary conditions (2.32) of the strong formulation of the IBVP yield the weighted integral formulation by multiplying with a weighting or test function $\delta \mathbf{u}$ and integrating over the respective domains

$$\int_{\Omega} (\rho_0 \ddot{\mathbf{u}} - \text{Div } \mathbf{P} - \hat{\mathbf{b}}_0) \cdot \delta \mathbf{u} \, dV + \int_{\Gamma_\sigma} (\mathbf{P} \cdot \mathbf{N} - \hat{\mathbf{t}}_0) \cdot \delta \mathbf{u} \, dA = 0. \quad (2.35)$$

The weighting function $\delta \mathbf{u}$ can be interpreted as virtual displacements. In contrast to the point-wise enforcement of the governing equations in the strong formulation, the weighted integral formulation now is enforced in an integral sense. Applying the Gauss-Green divergence theorem yields the virtual work $\delta \mathcal{W}$ in reference configuration,

$$\delta \mathcal{W} := \underbrace{\int_{\Omega} \rho_0 \ddot{\mathbf{u}} \cdot \delta \mathbf{u} \, dV}_{-\delta \mathcal{W}_{\text{kin}}} + \underbrace{\int_{\Omega} \mathbf{S} : \delta \mathbf{E} \, dV}_{-\delta \mathcal{W}_{\text{int}}} - \underbrace{\int_{\Omega} \hat{\mathbf{b}}_0 \cdot \delta \mathbf{u} \, dV - \int_{\Gamma_\sigma} \hat{\mathbf{t}}_0 \cdot \delta \mathbf{u} \, dA}_{-\delta \mathcal{W}_{\text{ext}}} = 0. \quad (2.36)$$

Compared to the strong and weighted integral formulation, (2.36) now possesses weaker derivability requirements since one spatial derivative of the primary variable \mathbf{u} has been shifted to the test function $\delta\mathbf{u}$ within the variation $\delta\mathbf{E}$. The Dirichlet boundary conditions (2.31) are enforced by

$$\mathbf{u} = \hat{\mathbf{u}} \quad \text{on } \Gamma_u \quad \forall \mathbf{u} \in \mathcal{S}, \quad (2.37)$$

$$\delta\mathbf{u} = \mathbf{0} \quad \text{on } \Gamma_u \quad \forall \delta\mathbf{u} \in \mathcal{T}, \quad (2.38)$$

where the test function vanishes on the Dirichlet boundary and the solution and weighting function spaces \mathcal{S} and \mathcal{T} , respectively, are sufficiently smooth. The weak formulation of the IBVP then is

$$\text{find } \mathbf{u} \in \mathcal{S} \text{ such that } \delta\mathcal{W} = 0 \quad \forall \delta\mathbf{u} \in \mathcal{T}. \quad (2.39)$$

2.2.2 Discretization in space

The weak formulation (2.39) is solved discretely at nodes connected through n_{ele} disjunct finite elements

$$\Omega \approx \bigcup_{e=1}^{n_{\text{ele}}} \Omega^{(e)}, \quad (2.40)$$

where the superscript (e) denotes element quantities. The continuous quantities \mathbf{u} and $\delta\mathbf{u}$ in the weak formulation (2.39) are approximated in an element-wise manner on an element (e) by $\mathbf{u}_h^{(e)}$ and $\delta\mathbf{u}_h^{(e)}$, respectively,

$$\mathbf{u}^{(e)}(\mathbf{X}, t) \approx \mathbf{u}_h^{(e)}(\mathbf{X}, t), \quad (2.41)$$

$$\delta\mathbf{u}^{(e)}(\mathbf{X}) \approx \delta\mathbf{u}_h^{(e)}(\mathbf{X}), \quad (2.42)$$

where subscript h denotes spatially approximated quantities using basis functions N_k , often called shape functions. Typically, $\Omega^{(e)}$ is mapped to a parameter space $\boldsymbol{\xi}$. Displacements and their variation are then approximated using the basis functions

$$\mathbf{u}_h^{(e)}(\boldsymbol{\xi}, t) = \sum_{k=1}^{n_{\text{nod}}^{(e)}} N_k(\boldsymbol{\xi}) \mathbf{d}_k(t), \quad \text{in } \Omega^{(e)} \forall (e), \quad (2.43)$$

$$\delta\mathbf{u}_h^{(e)}(\boldsymbol{\xi}) = \sum_{k=1}^{n_{\text{nod}}^{(e)}} N_k(\boldsymbol{\xi}) \delta\mathbf{d}_k, \quad \text{in } \Omega^{(e)} \forall (e). \quad (2.44)$$

Here, the same shape functions N_k are used for displacements $\mathbf{u}_h^{(e)}$ and virtual displacements $\delta\mathbf{u}_h^{(e)}$. This approach is termed Bubnov Galerkin or just Galerkin method, whereas in a Petrov Galerkin method solution and weighting basis functions are chosen independently. The spaces \mathcal{S} and \mathcal{T} are restricted to the finite dimensional solution and weighting function subspaces $\mathcal{S}_h \subset \mathcal{S}$ and $\mathcal{T}_h \subset \mathcal{T}$, respectively. The former continuous displacement field is now characterized by

discrete nodal displacements \mathbf{d}_k , where $n_{\text{nod}}^{(e)}$ is the number of nodes of a given element. The geometry in reference and current configuration is then approximated in an element-wise manner as

$$\mathbf{x}_h^{(e)}(\boldsymbol{\xi}, t) = \sum_{k=1}^{n_{\text{nod}}^{(e)}} N_k(\boldsymbol{\xi}) \mathbf{x}_k(t), \quad \text{in } \Omega^{(e)} \forall (e), \quad (2.45)$$

$$\mathbf{X}_h^{(e)}(\boldsymbol{\xi}) = \sum_{k=1}^{n_{\text{nod}}^{(e)}} N_k(\boldsymbol{\xi}) \mathbf{X}_k, \quad \text{in } \Omega^{(e)} \forall (e), \quad (2.46)$$

with discrete nodal positions \mathbf{X}_k and \mathbf{x}_k in reference and current configuration, respectively. Using the isoparametric concept, the geometry in current configuration $\mathbf{x}_h^{(e)}$ and reference configuration $\mathbf{X}_h^{(e)}$ is approximated using the same shape functions N_k as for the displacements in an element-wise manner. In this thesis, exclusively ten-node tetrahedral elements with quadratic Lagrange polynomials as basis functions are used. The displacement error e_d of the Galerkin approximation

$$e_d = \mathbf{u} - \mathbf{u}_h \quad (2.47)$$

is orthogonal to the discrete weighting basis function space \mathcal{T}_h . This property can be interpreted that the space of weighting basis functions in \mathcal{T}_h cannot detect the deviation of \mathbf{u}_h from \mathbf{u} .

The weak form (2.39) is evaluated in an element-wise manner using Gaussian quadrature and sorted in global vectors using the assembly operator

$$\int_{\Omega} (\bullet) dV \approx \mathbf{A} \int_{\Omega_h^{(e)}} (\bullet) dV. \quad (2.48)$$

Inserting the discretized solution (2.43) into the principle of virtual work (2.36) yields the following spatially semi-discrete version in vector-matrix notation

$$\delta \mathbf{d}^T \left[\mathbf{M} \ddot{\mathbf{d}} + \mathbf{F}(\mathbf{d}, \dot{\mathbf{d}}) \right] = 0, \quad (2.49)$$

with global mass matrix \mathbf{M} and force vector \mathbf{F} , containing the sum of internal and external forces. The global vectors $\delta \mathbf{d}$, \mathbf{d} , $\dot{\mathbf{d}}$ and $\ddot{\mathbf{d}}$ contain virtual displacements and discrete displacements, velocities, and accelerations, respectively. These vectors are of dimension $3 \cdot n_{\text{nod}}$, corresponding to the total number of structural degrees of freedom (DOFs), i.e., the structural unknowns in the system. Since (2.49) must hold for any choice of virtual displacements $\delta \mathbf{d}$ it can be equivalently reformulated as

$$\mathbf{R}_{\text{semi}}^S := \mathbf{M} \ddot{\mathbf{d}} + \mathbf{F}(\mathbf{d}, \dot{\mathbf{d}}) = 0, \quad (2.50)$$

which is the spatially semi-discrete form of the IBVP with the semi-discrete residual $\mathbf{R}_{\text{semi}}^S$.

2.2.3 Discretization in time

The discrete displacements $\mathbf{a} = \ddot{\mathbf{d}}$ and velocities $\mathbf{v} = \dot{\mathbf{d}}$ in the IBVP are discretized in time with Newmark's method [139]

$$\mathbf{v}_{n+1} = \frac{\gamma}{\beta\Delta t} (\mathbf{d}_{n+1} - \mathbf{d}_n) - \frac{\gamma - \beta}{\beta} \mathbf{v}_n - \frac{\gamma - 2\beta}{2\beta} \Delta t \mathbf{a}_n, \quad (2.51)$$

$$\mathbf{a}_{n+1} = \frac{1}{\beta\Delta t^2} (\mathbf{d}_{n+1} - \mathbf{d}_n) - \frac{1}{\beta\Delta t} \mathbf{v}_n - \frac{1 - 2\beta}{2\beta} \mathbf{a}_n, \quad (2.52)$$

with parameters $\gamma \in [0, 1]$ and $\beta \in [0, 0.5]$, and time step size $\Delta t = t_{n+1} - t_n$. Additionally, the generalized- α method [38] is applied, yielding quantities at a generalized time step $n + 1 - \alpha_i$

$$(\bullet)_{n+1-\alpha_i} = (1 - \alpha_i)(\bullet)_{n+1} + \alpha_i(\bullet)_n, \quad \alpha_i \in [0, 1], \quad i \in \{f, m\} \quad (2.53)$$

depending on the weights α_f and α_m for force vector and mass matrix respectively. Finally, the time and space discrete structural residual is obtained as

$$\mathbf{R}_{n+1}^S := \mathbf{M} \mathbf{a}_{n+1-\alpha_m} + \mathbf{F}_{n+1-\alpha_f} = \mathbf{0}. \quad (2.54)$$

Note that this time integration scheme is not energy conserving, for which other methods available.

2.3 Geometrical models

Two geometrical models are used in this work. The high-fidelity patient-specific four-chamber geometry in Section 2.3.1 is obtained from magnetic resonance imaging (MRI), which is useful for model validation but is computationally expensive. The simplified ellipsoid model in Section 2.3.2 on the other hand is fast to evaluate and can be used in proof-of-concept simulations.

2.3.1 Patient-specific four-chamber geometry

A comprehensive *in vivo* MRI data set was obtained from a 33 year old healthy female volunteer. The imaging data was acquired at King's College London, UK using a Philips Achieva 1.5T MRI scanner. As several minutes might have passed between different imaging sequences, the subject may have moved, leading to a spatial misalignment. Thus, all images used in this work are rigidly registered onto another. In a first step, short axis cine MRI is registered to 3D MRI. In a second step, two-chamber, three-chamber, and four-chamber cine MRI is registered to short-axis cine MRI.

A four chamber geometry was obtained from a dual-phase whole-heart 3D b-SSFP sequence [179], acquisition matrix $212 \times 209 \times 200$, acquired voxel size $2 \times 2 \times 2$ mm, repetition time 4.5 ms, echo time 2.2 ms, echo train length 26 and flip angle 90° . The diastolic rest period (diastasis) was used to generate the computational mesh. The geometry was meshed using Gmsh [66] with a resolution of 2 mm, yielding 282 288 nodes and 167 232 quadratic tetrahedral elements, totaling a 846 864 structural degrees of freedom. Additionally, the geometry contains triangular surface elements with no additional degrees of freedom to track the movement of the planes

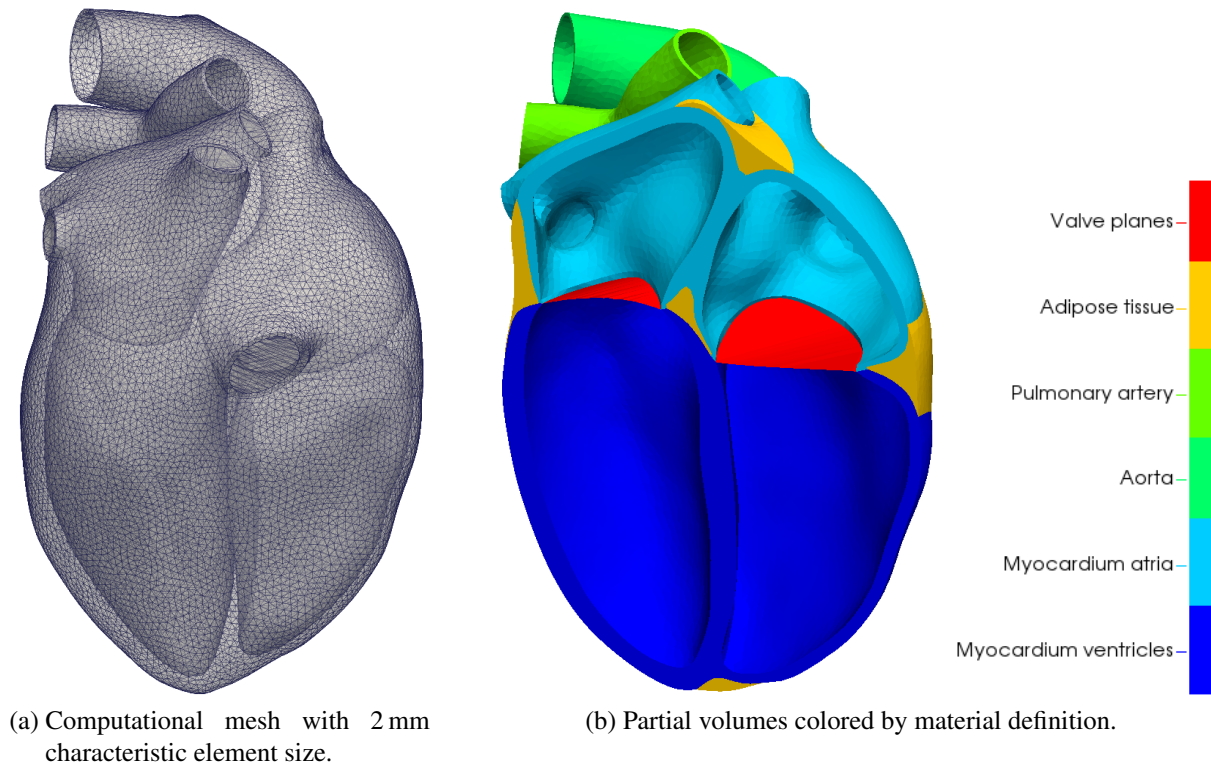


Figure 2.1: Four chamber patient-specific cardiac geometry.

of cardiac valves, allowing to monitor the volumes of all four cardiac cavities. The meshed geometry is shown in Figure 2.1a. All four cardiac cavities are closed with surface elements with no additional degrees of freedom at the valve planes depicted in red in Figure 2.1b at the left and right atrioventricular plane, respectively. The atria are additionally closed at their respective connections to the vasculature. The volumes of all four cardiac cavities can thus be monitored and the movement of cardiac valve planes tracked. The different materials are depicted in Figure 2.1b.

Remark Whole-heart 3D-imaging differs from cine MRI data, since both imaging techniques provide slightly different grey-values for the same tissues. More importantly, the patient might have moved between both image sequences, leading to a spatial misalignment even after registration. However, in many applications the simulation results are compared to cine MRI data, for example during model validation or inverse analysis. It has thus to be accepted that even in reference configuration, the heart does not perfectly align with cine MRI data. The alternative of using short-axis cine MRI during diastasis to obtain the reference configuration, however, is even less desirable. The present MRI data set's cine MRI has a slice thickness of 8 mm, leading to strong artifacts in the segmented geometry.

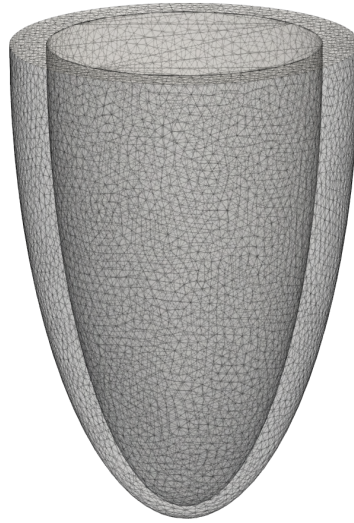


Figure 2.2: Simplified prolate spheroid geometry for the left ventricle of the four-chamber geometry in Section 2.3.1.

2.3.2 Generic prolate spheroid geometry

A common tool in computational cardiac modeling are simplified geometries, which reduce computational demand and geometrical complexity while resembling one part of the heart. A common example of such a model is the prolate spheroid geometry, mimicking the shape of the left ventricle [20, 48, 65]. The geometry shown in Figure 2.2 is shaped so that volume and dimensions resemble closely the ones of the left ventricle of the four-chamber geometry introduced in the previous section. It is discretized with ten-node quadratic tetrahedral elements and has 44'475 structural degrees of freedom.

2.4 Modeling cardiac tissue

This section introduces several material models used in computational cardiac modeling. Material can be classified in a passive and active behavior. There is an ongoing debate on whether to use an active stress or an active strain approach to model cardiac contraction, see e.g. [3]. In the present work, an active stress model is used, as the cardiac muscle can exert an active stress without deformation. The total stress is thus additively decomposed in an active part \mathbf{S}_{act} and a passive part \mathbf{S}_{pass} ,

$$\mathbf{S} = \mathbf{S}_{\text{pass}} + \mathbf{S}_{\text{act}}. \quad (2.55)$$

The material components of different tissues are specifically defined in Chapters 3 and 4. Passive behavior, detailed in Section 2.4.2, describes the tissues resistance with respect to deformation, as in any classical mechanical engineering problem. Active behavior, detailed in Section 2.4.3, describes the capability of the heart's muscle cells, the myocytes, to contract and impose a stress component on the tissue. Both passive and active component may depend on a complex three-dimensional architecture of the myofibers, which is described in Section 2.4.1. In patient-specific biomechanical problems, the reference configuration of the simulation obtained from medical

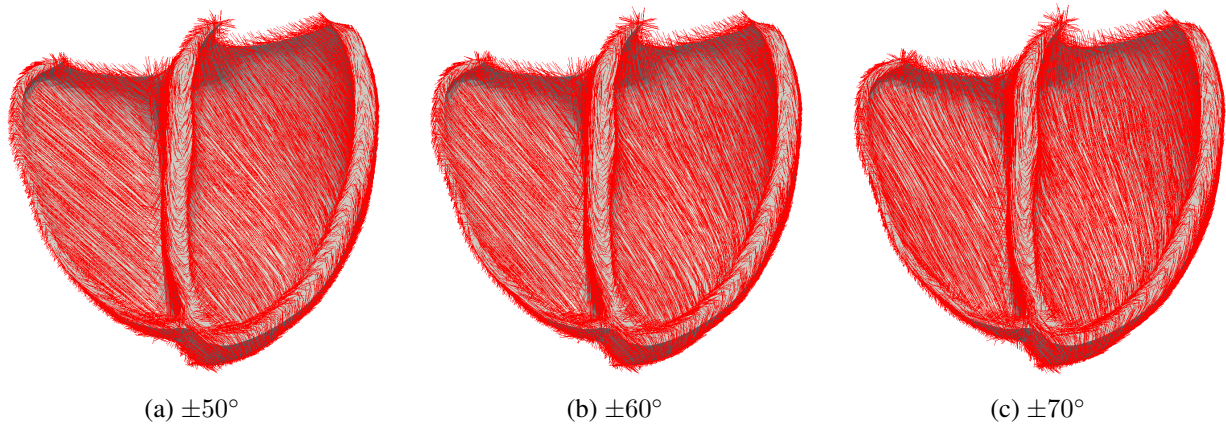


Figure 2.3: Different ventricular fiber orientations.

imaging is usually not stress-free. The prestress method in Section 2.4.4 yields a reference configuration which is in balance with external loads present during imaging.

2.4.1 Local anisotropy

It is widely accepted that passive cardiac tissue behavior is non-linear, anisotropic (orthotropic), viscoelastic and history-dependent [27, 166]. This is mainly due to the extracellular collagen network structure [99]. The strain-stress relationship of myocardial tissue is classically represented using anisotropic hyperelastic potentials [88], which require the local fiber and sheet orientation as well as the stiffness in each of these directions. Furthermore, active stress is applied according to local cardiac muscle orientation.

The knowledge of patient-specific and regionally varying constitutive properties of myocardial tissue is crucial for an accurate representation of the cardiac contraction in a numerical simulation [88]. The ventricular myocardium has a complex three-dimensional architecture [68]. In particular, the myocardium is a composite of layers (or sheets) of parallel myocytes, which are the predominant fiber types, occupying 70% of the volume. The remaining 30% consists of various interstitial components, of which only 2–5% are occupied by collagen arranged in a spatial network that forms lateral connections between adjacent fibers. The muscle fiber direction and the sheet orientations change through the thickness of the myocardium [55].

It is well known that the fiber orientation has a strong impact on active cardiac mechanics [9, 49, 67, 140, 178, 188]. Patient-specific fibers can be obtained from diffusion tensor MRI [138]. Three commonly used fiber architectures for ventricular myocardium, namely $\pm 50^\circ$, $\pm 60^\circ$, and $\pm 70^\circ$, are shown in Figure 2.3. Here, the angles represent the constant fiber angle at epi- and endocardium, respectively. The transverse angle is zero throughout the myocardium. The sheet normal vector \mathbf{n}_0 is perpendicular to the epi- and endocardial surfaces. The sheet vector \mathbf{s}_0 is then obtained from $\mathbf{s}_0 = \mathbf{n}_0 \times \mathbf{f}_0$.

In this work, the local angles of cardiac myofibers are prescribed at epi- and endocardium of the ventricles. Using harmonic lifting, the fiber vectors \mathbf{f}_0 are interpolated to the interior of the domain by solving a Laplace problem [137]. The solution of the Laplace problem yields ap-

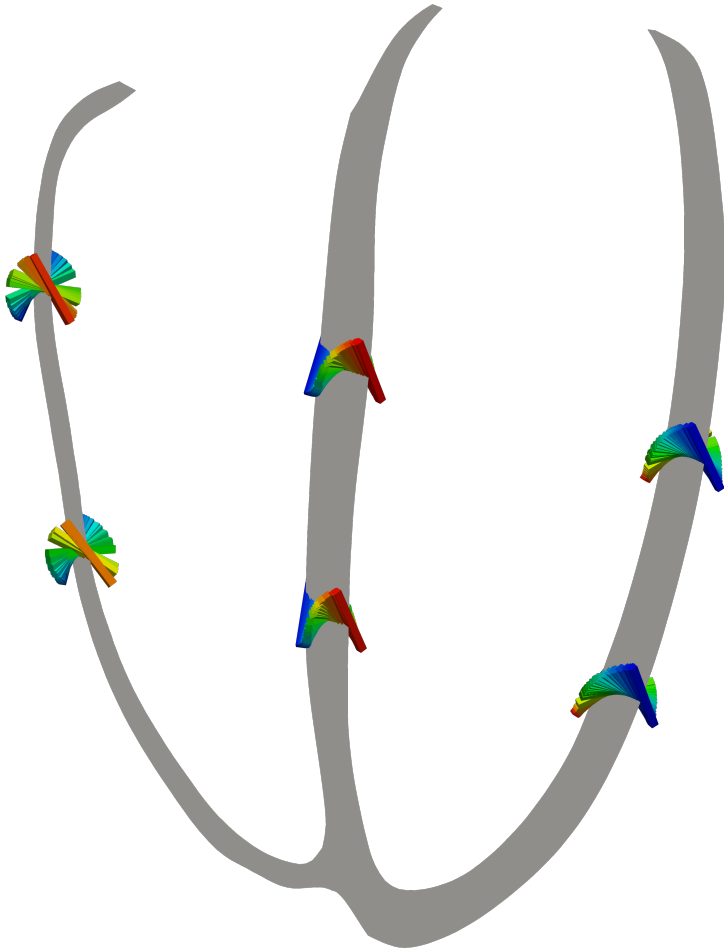


Figure 2.4: Transmural fiber angles for a $\pm 60^\circ$ fiber orientation.

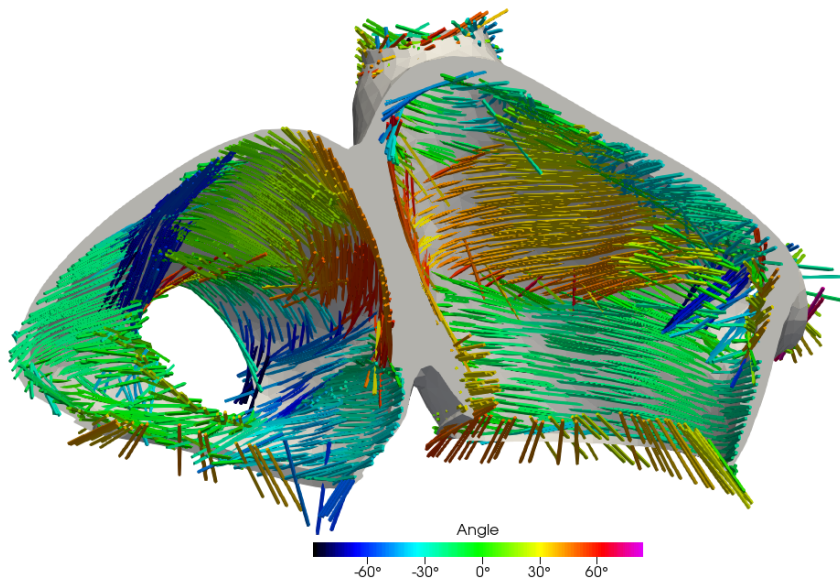


Figure 2.5: Atrial fiber orientation. Fiber angles are with respect to the ventricular long axis.

proximately a linear interpolation of the fiber vector components throughout the thickness of the myocardial wall. This transmural fiber-interpolation is visualized in Figure 2.4 for a cut through the ventricular myocardium, based on a $\pm 60^\circ$ fiber orientation. As the atrial fiber architecture is more complex, it is obtained using a semi-automatic registration method based on the fiber definition in atlas atria [90, 92] and visualized in Figure 2.5.

Remark Different methods exist to incorporate local anisotropy in the form of local coordinate system $(\mathbf{f}_0, \mathbf{s}_0, \mathbf{n}_0)$ into computational models. In the most simple case, the local coordinate system is constant per element. However, as the myocardium exhibits a strong transmural variation in local orientations, see Figure 2.4, a constant per element coordinate system in combination with a coarse discretization can lead to a deterioration in spatial convergence. Alternatively, the local coordinate system can be defined on a nodal basis and its vector components interpolated to the integration points using the elements' shape functions.

To illustrate the effects of different definitions of local coordinate systems, four simulations are compared in Figure 2.6. It shows an end-systolic configuration of a cardiac contraction simulation, using the four chamber geometry from Section 2.3.1. Compared are two coordinate system interpolations, constant per element and interpolated on integration points, and two characteristic element sizes, 2 mm and 1 mm. The configuration with constant per element coordinate systems and 2 mm discretization size (black) visibly differs from the other three configurations, especially at the interventricular septum. On the other hand, the configurations using a local coordinate system interpolated to the integration points coincide well for the 2 mm (red) and 1 mm (orange) discretization size. These configurations also coincide well with constant per element coordinate systems and 1 mm discretization size (blue). These results suggest that using coordinate systems interpolated at the integration points improve spatial convergence and should be used in all cardiac simulations.

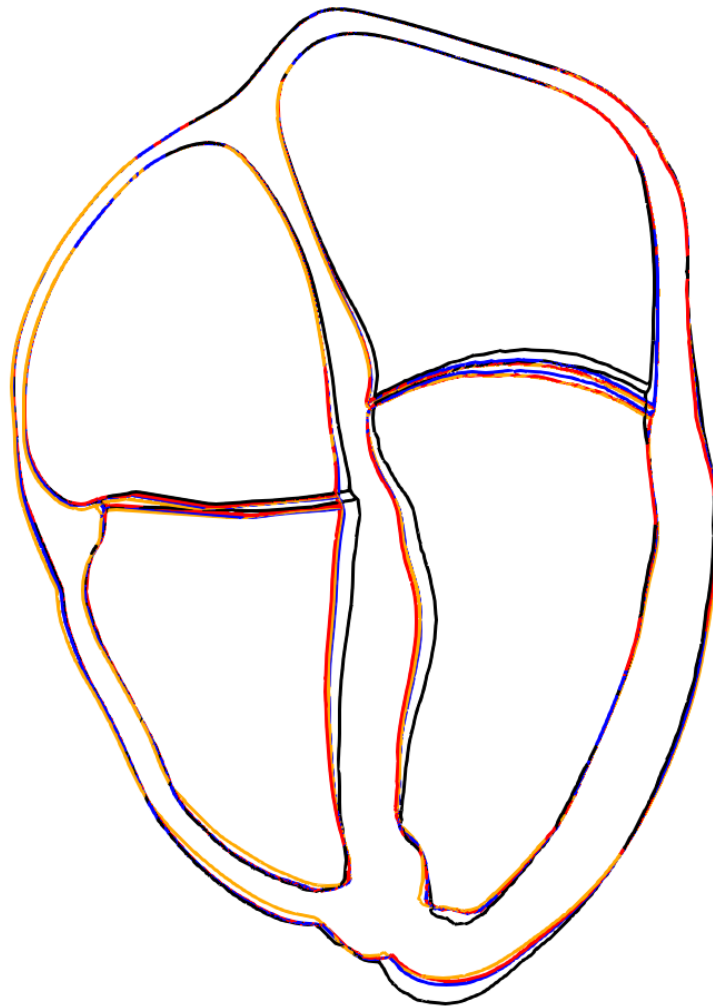


Figure 2.6: End-systolic configuration of cardiac contraction simulation using the four-chamber geometry from Section 2.3.1. The geometry is cut in four-chamber view for different coordinate system interpolations and characteristic discretization sizes: constant per element 2 mm (black) and 1 mm (blue), interpolated on integration points 2 mm (red) and 1 mm (orange).

2.4.2 Passive behavior

The passive stress contribution \mathbf{S}_{pass} is in the most general case additively composed of different elastic materials i with strain energy density function ψ_i and a viscous material with pseudo-potential ψ_{visco} ,

$$\mathbf{S}_{\text{pass}} = \sum_i \frac{\partial \psi_i}{\partial \mathbf{E}} + \frac{\partial \psi_{\text{visco}}}{\partial \dot{\mathbf{E}}}. \quad (2.56)$$

Based in the volumetric-isochoric split of the deformation gradient in (2.10), the isochoric right Cauchy-Green tensor becomes

$$\bar{\mathbf{C}} = \bar{\mathbf{F}}^T \cdot \bar{\mathbf{F}} = J^{-2/3} \mathbf{C}. \quad (2.57)$$

Depending on the isochoric deformation, the following modified invariants \bar{I}_i are defined:

$$\bar{I}_1 = \text{tr}(\bar{\mathbf{C}}), \quad \bar{I}_2 = \frac{1}{2} [\text{tr}^2(\bar{\mathbf{C}}) - \text{tr}(\bar{\mathbf{C}}^2)]. \quad (2.58)$$

For the treatment of anisotropic tissues, pseudo-invariants are defined

$$I_{4,f} = \mathbf{f}_0 \cdot \mathbf{C} \mathbf{f}_0, \quad I_{4,s} = \mathbf{s}_0 \cdot \mathbf{C} \mathbf{s}_0, \quad I_{8,fs} = \mathbf{f}_0 \cdot \mathbf{C} \mathbf{s}_0, \quad (2.59)$$

based on fiber orientation \mathbf{f}_0 and sheet orientation \mathbf{s}_0 . Together with the sheet normal orientation \mathbf{n}_0 , the orthonormal local coordinate system $\mathbf{s}_0 = \mathbf{n}_0 \times \mathbf{f}_0$ is formed. Throughout this work, different hyperelastic potentials are utilized for different biological tissues within the heart.

Neo-Hooke The isotropic Neo-Hooke material is

$$\psi_{\text{NH}} = \frac{\mu}{2} (\bar{I}_1 - 3), \quad (2.60)$$

with stiffness parameter μ . It is used in this thesis for biological materials where no specific material definition is available, e.g. for adipose tissue.

Anisotropic exponential The mechanical properties of healthy myocardial tissue have been determined in biaxial extension testing with asymmetric loading [44, 192] and triaxial shear testing [45]. However, information from both extension and shear testing is necessary to fully characterize the orthotropic behavior of myocardial tissue [88]. Combined extension and shear testing of human specimens was recently carried out in [166] for the first time, further investigating the viscoelastic and history-dependent material behavior. From this comprehensive data set, constitutive parameters were fitted in [75]. In biaxial extension testing, a thin (1-2 mm) sheet ($40 \times 40 \text{ mm}^2$ [192], $25 \times 25 \text{ mm}^2$ [166]) of myocardium was sliced tangentially from the left ventricular free wall. The slices were cut assuming a uniform fiber direction aligned to the sheet edges, as judged by eye. In triaxial shear testing, a small cube ($3 \times 3 \times 3 \text{ mm}^3$ [45], $4 \times 4 \times 4 \text{ mm}^3$ [166]) is cut from the myocardium, again assuming a uniform fiber distribution aligning with the edges of the specimen.

Based in these experimental observations, an exponential orthotropic solid ψ_{exp} material model was formulated [88]. It describes the interplay between extracellular matrix, myofibers, and laminar sheets as

$$\psi_{\text{exp}} = \frac{a}{2b} \left(e^{b(\bar{I}_1 - 3)} - 1 \right) + \frac{a_{fs}}{2b_{fs}} \left(e^{b_{fs} I_{8,fs}^2} - 1 \right) + \sum_{i \in \{f,s\}} \frac{a_i}{2b_i} \left(e^{b_i(I_{4,i} - 3)} - 1 \right), \quad (2.61)$$

with material parameters a_i and b_i with indices f, s, fs , denoting fiber orientation, sheet orientation, and their interaction, respectively. The orientation of the local coordinate system is detailed in Section 2.4.1. This material is widely used in cardiac biomechanics, see e.g. [10, 11, 106], and parameters were fitted for this model in [88] and [75] to extension tests and shear test. Note, however, that different parameter sets were obtained for each of the tests. There exists no unique data set that matches the experimental observations of both extension tests and shear tests at the same time. It should also be noted that the choice of reference configuration, in which the tissue's behavior is exactly orthotropic, is open to debate.

Mooney-Rivlin Due to its simplified definition with only two material parameters, the isotropic Mooney-Rivlin material is also used to describe the passive behavior of myocardial tissue [30, 156]. Its strain-energy density function is

$$\psi_{\text{MR}} = C_1(\bar{I}_1 - 3) + C_2(\bar{I}_2 - 3), \quad (2.62)$$

with stiffness parameters C_1 , and C_2 .

Volumetric penalty Furthermore, two different formulations of a volumetric penalty function [185] are used in this work,

$$\psi_{\text{vol,a}} = \kappa \left(J + \frac{1}{J} - 2 \right), \quad (2.63)$$

$$\psi_{\text{vol,b}} = \frac{\kappa}{2} (1 - J)^2, \quad (2.64)$$

with penalty parameter κ . Both penalize $J \neq 1$ to enforce quasi-incompressibility, i.e., $J \rightarrow 1$ for $\kappa \rightarrow \infty$. In practice, κ is chosen so that the change in volume throughout the simulation is sufficiently small.

Viscous A viscous material component is modeled with a viscous pseudo-potential ψ_{visco}

$$\psi_{\text{visco}} = \frac{\eta}{2} \text{tr} \left(\dot{\mathbf{E}}^2 \right), \quad (2.65)$$

with viscosity η . This material is frequently used to model myocardial viscosity in a simplified manner [30, 32]. Note that there is an ongoing research for more advanced cardiac viscous models [75, 166].

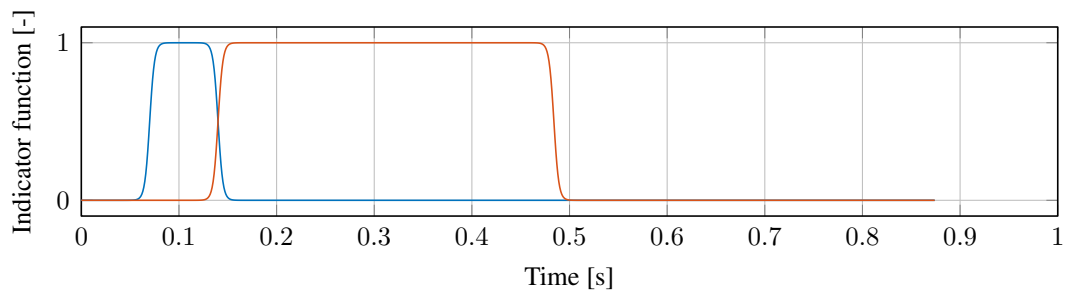
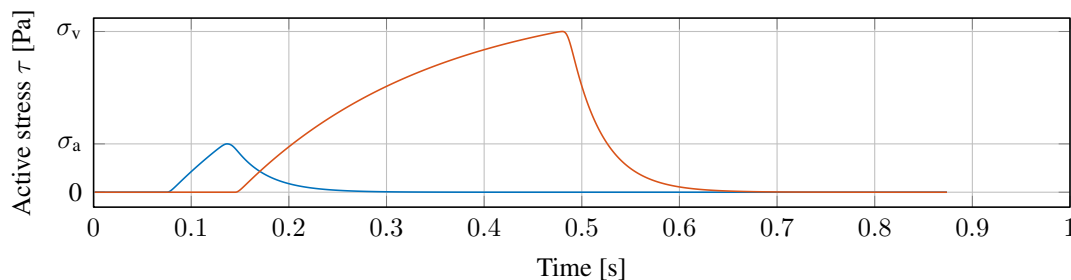
(a) Prescribed indicator functions $f(t)$ for atria (blue) and ventricles (red).(b) Active stress $\tau(t)$ for atria (blue) and ventricles (red) with maximum values σ_a and σ_v , respectively.

Figure 2.7: Active stress.

2.4.3 Active behavior

As the focus of this thesis is the mechanical function of the heart, the propagation of the electrical signal within the myocardial tissue is not accounted for. Instead, all myocardial tissue contracts simultaneously in all simulations presented in this thesis. This approach ignores regional deviations in the onset of systole and diastole. Assuming a simultaneous activation and deactivation of the whole heart might thus predict unrealistic timing between atrial and ventricular contraction. Due to the large size of the ventricles, simultaneous activation might also lead to slightly different contractile behavior than regionally resolved activation times. However, it is not expected that the findings of this thesis are strongly influenced by cardiac electrophysiology. For detailed information on simulating the electrical conduction system of the heart, the reader is referred to [89–92].

As a result of the electrochemical processes inside the myocytes, in particular due to calcium dynamics, an active force is generated inside the myocyte sarcomeres mainly along the fiber direction. A first model of myocyte contraction was introduced in [16]. A more sophisticated model for cardiac contraction on the myocyte level exists [32], including the Frank-Starling mechanism. This model depends on various cell-level parameters which were calibrated for example in [29]. In this thesis, a much simplified model is used with only three parameters. Hence, the active stress tensor

$$\mathbf{S}_{\text{act}} = \tau(t) \mathbf{f}_0 \otimes \mathbf{f}_0 \quad (2.66)$$

results from prescribing the unidirectional active stress τ in fiber direction \mathbf{f}_0 . The orientation of the local fiber direction \mathbf{f}_0 is detailed in Section 2.4.1. The active stress is obtained from an

evolution equation

$$\dot{\tau}(t) = -|u(t)| \tau(t) + \sigma_0 |u(t)|_+, \quad \tau(0) = 0, \quad (2.67)$$

with active stress $\tau \in [0, \sigma_0[$ and the function $|u(t)|_+ = \max(u(t); 0)$. The contractility σ_0 controls the upper limit of the active stress component. The prescribed activation function $u(t)$ is

$$u(t) = \alpha_{\max} \cdot f(t) + \alpha_{\min} \cdot [1 - f(t)], \quad (2.68)$$

with actin-myosin binding and unbinding rates α_{\max} and α_{\min} , respectively. The smooth indicator function $f \in]0, 1[$ indicates ventricular systole

$$f(t) = S^+(t - t_{\text{sys}}) \cdot S^-(t - t_{\text{dias}}), \quad (2.69)$$

depending on the descending and ascending sigmoid functions S^+ and S^- , respectively. The sigmoid functions are modeled using the hyperbolic tangent function

$$S^\pm(\Delta t) = \frac{1}{2} \left[1 \pm \tanh \left(\frac{\Delta t}{\gamma} \right) \right], \quad (2.70)$$

with steepness γ . An exemplary indicator function is visualized in Figure 2.7a for atrial and ventricular myocardium. The resulting active stress curve is displayed in Figure 2.7b. Note that the actual maximum value $\max(\tau)$ depends on the activation function u and may be significantly lower than the asymptotic active stress σ_0 . Thus, for clarity, the maximum values σ_v and σ_a , denoting maximum ventricular and atrial active stress, respectively, are stated instead of σ_0 , refer to Figure 2.7b. The times t_{sys} and t_{dias} model the onset of systole and diastole, respectively.

2.4.4 Prestress

For the reference configuration a patient-specific geometry is used, segmented from static 3D MRI at diastolic rest period (diastasis), see Section 2.3. Diastasis is very suitable for the reference configuration, since both ventricular and atrial myofibers are relaxed, the heart is not accelerated, and blood pressures are minimal and constant. This simplifies the task of obtaining the stress state of the reference configuration, which in this case is determined by the static blood pressures within the cardiac cavities. The geometry is always prestressed, if non-zero, with the initial ventricular and atrial pressures. In this work, the Modified Updated Lagrangian Formulation is used as proposed in [59, 60]. This method incrementally calculates a deformation gradient with respect to an unknown stress-free reference configuration. From this deformation gradient, a stress field is calculated so that the segmented geometry of the heart is in balance with the prestressed pressure state. Additionally, any springs present in boundary conditions are prestressed as well. Note that while this technique allows to model prestress, the residual stresses inherent in myocardial tissue [97] are not accounted for. Although the resulting configuration is in balance with all prescribed external loads, it does not take into account the preferred homeostatic state of cardiac tissue.

Remark 1 Prestress has a major influence on passive material behavior and thus on cardiac mechanics. Furthermore, prestress is also important for models accounting for the Frank-Starling mechanism as prestress determines here the initial stretching of the sarcomeres. This influence is visualized by a small numerical experiment with the patient-specific four-chamber geometry introduced in Section 2.3.1 using the isotropic Mooney-Rivlin material from (2.62) for ventricular and atrial myocardium. The model is purely structural and contains the pericardial boundary condition later examined in Chapter 3. In this prestress study, four simulations of cardiac contraction are compared. Each simulation features a different combination of left and right ventricular pressure, whereas atrial pressures are assumed to be zero throughout the simulation. The geometry is first prestressed to the given ventricular pressures using MULF. During cardiac contraction, ventricular pressures are kept constant to their prestressed value.

The results are compared at end-systole in four-chamber view in Figure 2.8 for four combinations of ventricular pressures (left/right [mmHg]): 0/0 (red), 10/10 (orange), 10/0 (green), and 0/10 (black). Please note that the *left* ventricle is on the *right* side of the image. The influence of ventricular prestress becomes evident by observing the displacements at the interventricular septum. There are only minor differences between the symmetrically prestressed configurations 0/0 (red) and 10/10 (orange). However, the strong influence of ventricular prestress pressures becomes evident when comparing the asymmetrically prestressed configurations 10/0 (green) and 0/10 (black). The interventricular septum buckles to the side of the higher prestress pressure.

Remark 2 Prestressing requires solving the cardiac model as a static problem, i.e., (2.50) with $\dot{\mathbf{d}} = \ddot{\mathbf{d}} = \mathbf{0}$. The quasi-incompressibility, enforced by a penalty potential (2.63) or (2.64), leads to an ill-conditioned system, posing challenges for the solver of the linearized system. Instead of a standard Newton algorithm to solve the nonlinear system (2.50), the method of pseudo-transient continuation (PTC) [61] is used in this work for prestressing. PTC adds an identity matrix to the tangential stiffness matrix, improving its conditioning. The identity matrix is scaled by a constant, the inverse of a pseudo-time step, which decreases to zero as the problem converges towards the solution.

2.5 Modeling the circulatory system

Hemodynamics describe the flow of blood within the circulatory system. There exist different approaches to incorporate blood flow into the computational model. Three-dimensional fluid-structure-interaction is resolved for example in [111, 141]. As the exact fluid dynamics are not needed for the structural cardiac model, they are represented in this thesis with lumped-parameter Windkessel models. A comprehensive review of different Windkessel models is given in [163]. In this work, a four element Windkessel model is used based on the ideas in [182] and [100]. The schematic of the Windkessel model is given in Figure 2.9a using resistances R , compliances C , and an inertance L_p . Pressures at different parts of the model are denoted by p . It is distinguished here between a proximal (index p) and a distal part (index d) of the outlets, i.e., lung and aorta for the right and left ventricle, respectively. The atrial pressure p_{at} is prescribed to simulate atrial systole, see Figure 2.9b. The reference pressure p_{ref} is kept constant.

For the four-chamber geometry from Section 2.3.1, the same Windkessel model is used for each ventricle with different parameters. For simplicity of notation, in this section all Windkessel



Figure 2.8: End-systolic configuration of cardiac contraction simulation using the four-chamber geometry from Section 2.3.1. The geometry is cut in four-chamber view for different ventricular prestress pressures (left/right [mmHg]): 0/0 (red), 10/10 (orange), 10/0 (green), and 0/10 (black). Note that the *left* ventricle is on the *right* of the image.

parameters and variables are valid for both left and right ventricle. Note that this cardiovascular model does not represent a closed-loop system, as introduced e.g. in [83], since the total blood volume is not conserved, i.e., blood exiting the right ventricle into the lungs does not enter the left atrium. However, using a Windkessel model for each ventricle provides us with a reasonable approximation of ventricular pressures.

The atrioventricular and semilunar valves are modeled with a smooth diode-like behavior by non-linear resistances $R_{av} := R(p_v - p_{at})$ and $R_{sl} := R(p_p - p_v)$, respectively,

$$R(\Delta p) = R_{\min} + (R_{\max} - R_{\min}) \cdot S^+(\Delta p) \quad (2.71)$$

depending on the sigmoid function S^+ from (2.70) with steepness k_p and the minimal and maximal valve resistance $R_{\min} \rightarrow 0$ and $R_{\max} \rightarrow \infty$, respectively. This yields the set of differential equations

$$\begin{aligned} \frac{p_v - p_{at}}{R_{av}} + \frac{p_v - p_p}{R_{sl}} + \dot{V}(\mathbf{u}) &= 0, \\ q_p - \frac{p_v - p_p}{R_{sl}} + C_p \dot{p}_p &= 0, \\ q_p + \frac{p_d - p_p}{R_p} + \frac{L_p}{R_p} \dot{q}_p &= 0, \\ \frac{p_d - p_{ref}}{R_d} - q_p + C_d \dot{p}_d &= 0. \end{aligned} \quad (2.72)$$

The vector of primary variables for a single Windkessel yields $\mathbf{p} = [p_v, p_p, p_d, q_p]^T$, including the flux q_p through the inertance L_p . The set of Windkessel equations (2.72) is discretized in time with the one-step- θ scheme

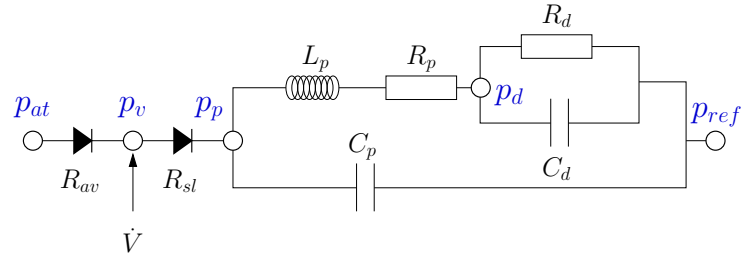
$$\begin{aligned} (\dot{\bullet})_{n+1} &= \frac{(\bullet)_{n+1} - (\bullet)_n}{\Delta t}, \\ (\bullet)_{n+\theta} &= \theta(\bullet)_{n+1} + (1 - \theta)(\bullet)_n, \quad \theta \in [0, 1]. \end{aligned} \quad (2.73)$$

This yields the discrete Windkessel residual \mathbf{R}^W evaluated at time step $n + \theta$. The parameters of the cardiovascular model are constant throughout this thesis and summarized in table A.2. Windkessel parameters are motivated by values from literature and adapted to yield physiological pressures as well as approximately a periodic state of the Windkessel systems.

The 0D Windkessel model is strongly coupled to the 3D structural model. The 0D model depends on the structural displacements of the 3D model via the change in ventricular volume \dot{V} . On the other hand, the 3D model depends on left (and right) ventricular pressure from the 0D model. The coupling between both models is described in the following section.

2.6 Coupled structure-Windkessel system

The discretized structural model introduced in Section 2.2 is coupled to a zero-dimensional model of the circulatory system, further specified in Section 2.5. This reduced order model of hemodynamics is commonly termed Windkessel model. For the coupled problem, time and space



(a) Schematic of the Windkessel model using symbols borrowed from electrical schematics.

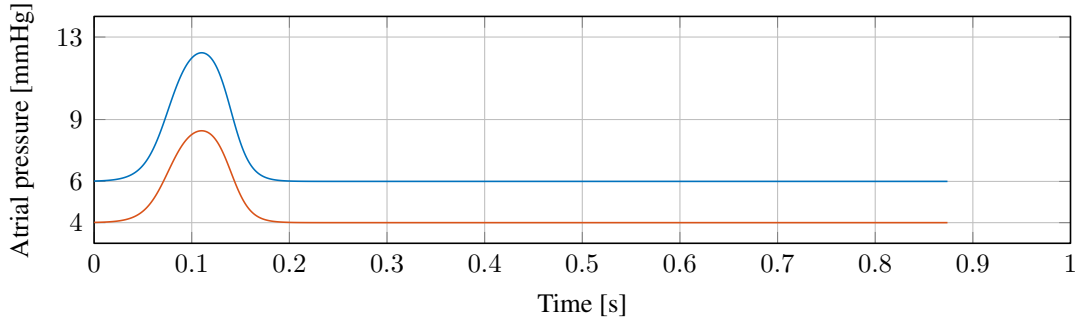

 (b) Prescribed left (blue) and right (red) atrial pressure $p_{at}(t)$.

Figure 2.9: Details of the Windkessel model used in this thesis.

discrete structural residual \mathbf{R}^S and Windkessel residual \mathbf{R}^W generally depend on the discrete displacements \mathbf{d} and discrete Windkessel DOFs \mathbf{p} , thus

$$\mathbf{R}_{n+1}^S := \mathbf{R}^S(\mathbf{d}_{n+1}, \mathbf{p}_{n+1}), \quad \mathbf{R}_{n+1}^W := \mathbf{R}^W(\mathbf{d}_{n+1}, \mathbf{p}_{n+1}). \quad (2.74)$$

The monolithically coupled structural-Windkessel is solved at time step $n + 1$ with the Newton-Raphson method

$$\begin{bmatrix} \mathbf{K}^S & \mathbf{K}^{SW} \\ \mathbf{K}^{WS} & \mathbf{K}^W \end{bmatrix}_{n+1}^i \cdot \begin{bmatrix} \Delta \mathbf{d} \\ \Delta \mathbf{p} \end{bmatrix}_{n+1}^{i+1} = - \begin{bmatrix} \mathbf{R}^S \\ \mathbf{R}^W \end{bmatrix}_{n+1}^i \quad (2.75)$$

for increments in displacements and Windkessel variables $\Delta \mathbf{d}_{n+1}$ and $\Delta \mathbf{p}_{n+1}$, respectively, at iteration $i + 1$ until convergence. The linearizations are

$$\mathbf{K}^S = \frac{\partial \mathbf{R}^S}{\partial \mathbf{d}}, \quad \mathbf{K}^{SW} = \frac{\partial \mathbf{R}^S}{\partial \mathbf{p}}, \quad \mathbf{K}^{WS} = \frac{\partial \mathbf{R}^W}{\partial \mathbf{d}}, \quad \mathbf{K}^W = \frac{\partial \mathbf{R}^W}{\partial \mathbf{p}}. \quad (2.76)$$

The solution is converged if

$$\|\mathbf{R}^S\|_{\infty} < tol_{res}^S \quad \text{and} \quad (2.77)$$

$$\|\Delta \mathbf{d}\|_{\infty} < tol_{inc}^S \quad \text{and} \quad (2.78)$$

$$\|\mathbf{R}^W\|_2 < tol_{res}^{OD} \quad \text{and} \quad (2.79)$$

$$\|\Delta \mathbf{p}\|_2 < tol_{inc}^{OD}, \quad (2.80)$$

with the structural and Windkessel residual and increment tolerances tol_{res}^S , tol_{res}^S , tol_{inc}^{0D} , and tol_{inc}^{0D} , respectively. For details on monolithically coupled structure-Windkessel cardiac problems, see [56, 83, 156].

3 Pericardial boundary conditions

This chapter studies in detail the interaction between the heart and its enclosing, the pericardium. Section 3.1 gives an overview of the anatomy and physiology of the pericardium and reviews pericardial boundary conditions currently used in cardiac mechanics simulations. In Section 3.2, a simplified model is derived to represent the influence of the pericardium by parallel springs and dashpots acting in normal direction to the epicardium. Different boundary condition cases are defined in Section 3.3, based on boundary conditions currently used in cardiac mechanics. To justify the simplifications made in Section 3.2, numerical experiments are carried out in Section 3.4. The influence of the pericardial boundary condition is demonstrated in Section 3.5 through a detailed quantitative comparison of simulation results to cine MRI. Ventricular volume, atrioventricular-plane-displacement, and atrioventricular interaction are evaluated and a quantitative error measurement is introduced by calculating a distance error at endo- and epicardial surfaces between simulation results and cine MRI. This chapter is closed with a discussion of the results, the limitations of the study, future perspectives, and some conclusions in Section 3.6.

Parts of this chapter were published in [148].

3.1 The pericardium

In the following, the anatomy of the pericardium and its physiology are reviewed, where the focus is on the mechanical interaction between the pericardium and the heart. Based on this review, variants of pericardial boundary conditions are evaluated and a model for pericardial-myocardial interaction is proposed.

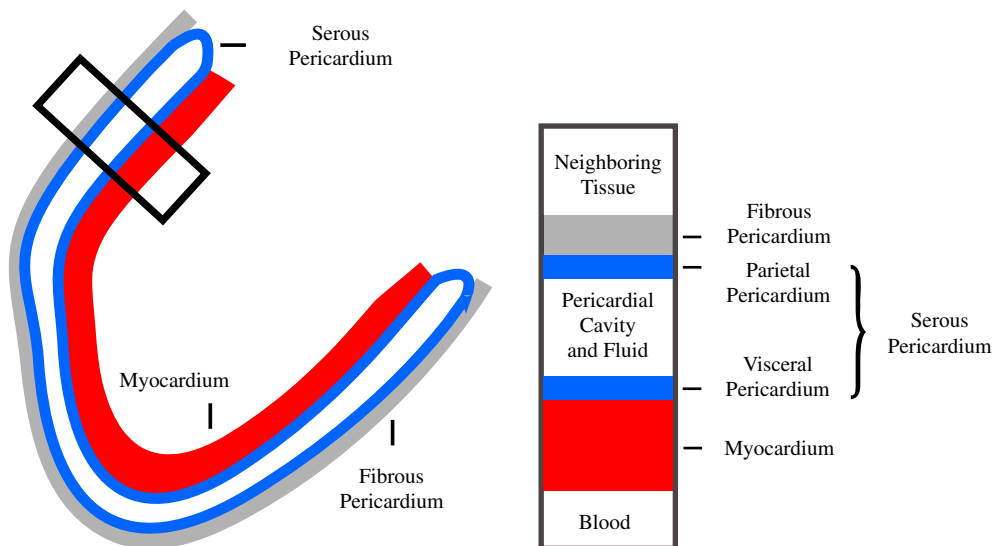
3.1.1 Anatomy

As visualized in Figure 3.1a, the pericardium is a sac-like structure with a combined thickness of 1-2 mm, containing the heart and parts of the great vessels [86]. Figures 3.1b and 3.1c show a cross-sectional view of the myocardium and the layers of the pericardium, which are detailed in the following.

The *fibrous pericardium* consists of a fibrous layer that forms a flask-like sac with a wavy collagenous structure of three interwoven main layers that are oriented 120° to each other [169]. It has a higher tensile stiffness than the myocardium and is dominated by the viscoelastic behavior of extracellular collagen matrix and elastin fibers [116]. The fibrous pericardium is fixed in space by a *three point cardiac seat belt* via the pericardial ligaments to the sternum. Furthermore, it is thoroughly attached to the central tendon of the thoracic diaphragm and additionally supported



(a) Dissected mediastinum with cut pericardium and heart surface. Image by G. M. Gruber, Medical University of Vienna, Austria.



(b) Location of the heart with respect to serous and fibrous pericardium. Inspired by [96].

(c) Cross-sectional view of transmurals layers of heart and pericardium. Inspired by [96].

Figure 3.1: Heart and pericardium.

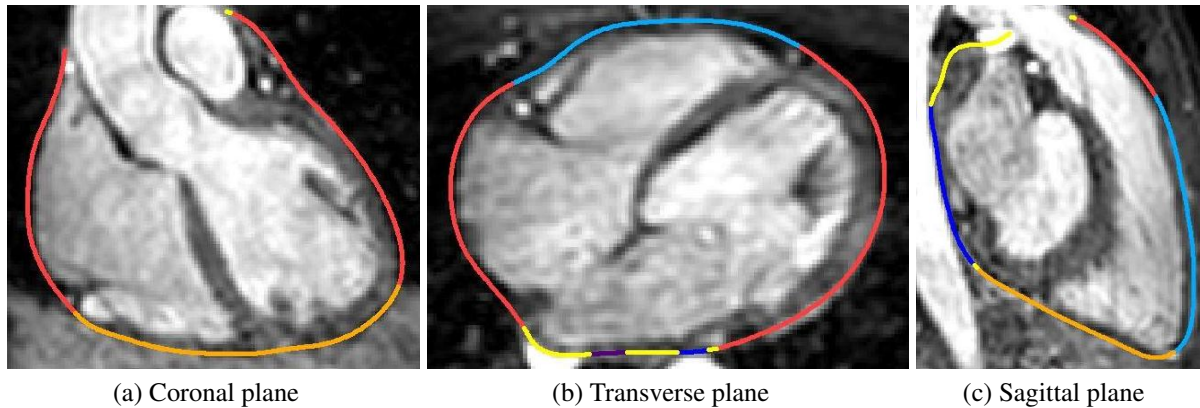


Figure 3.2: Position of the pericardium indicated in 3D MRI taken during diastasis. The neighboring tissue is color-coded: lungs (red), diaphragm (orange), sternum and ribs (light blue), aorta (dark blue), esophagus (purple), other (yellow). MRI courtesy of R. Chabiniok, J. Harmer, E. Sammut, King's College London, UK.

by the coats of the great vessels [168]. The various tissues, the fibrous pericardium is in contact with, can be seen in Figure 3.2.

The fibrous pericardium contains a serous membrane, the *serous pericardium*, forming a closed sac. The serous pericardium is connected to the myocardium (*visceral pericardium*) and the fibrous pericardium (*parietal pericardium*). The composite of fibrous and parietal pericardium is commonly referred to as pericardium, whereas the visceral pericardium in contact with the myocardium is referred to as epicardium [168]. The space between the visceral and parietal pericardium is the pericardial cavity, which is filled by a thin film of fluid with an average volume of 20-25 ml [86]. Between the visceral pericardium and the myocardium the heart is covered by a layer of adipose tissue, accumulated especially in the interventricular and atrioventricular grooves and around the coronary vessels, constituting about 20% of the heart weight [151]. A common analogy for the layers of the pericardium in contact with the heart in Figure 3.1b is that of a fist pushed into an inflated balloon [128]. The fist represents the heart and the two layers of the balloon represent the visceral and parietal pericardium.

3.1.2 Mechanical physiology

The pericardium serves multiple purposes [167] that can be grouped in: (a) membranous, where it serves as a barrier against the spread of infection [169] and (b) mechanical, where it secures cardiac stability via its attachments within the thorax [162], as will be explained in the following. The mechanical properties of the pericardium itself can be found in [155].

There is clear empirical evidence that the pericardium has a direct mechanical impact on the acute and chronic biomechanics of the heart. For example, in [70] it was discovered that the correlation of left and right ventricular pressure is higher with intact pericardium than after its complete removal. Maximal cardiac output during exercise can be increased acutely by the complete removal of the pericardium (*pericardiectomy*) through utilizing the Frank-Starling mechanism [79]. However, removing the pericardial restraint chronically promotes eccentric hypertrophy,

i.e., an increase in dimension and mass of the heart and a change in shape from elliptical to spherical. The pericardium thus acts as a diastolic constraint for the heart by exercising a radial compression stress. This was confirmed in [97] where it was observed that the opening angle of the myocardium with intact visceral pericardium is much higher than after its removal. The visceral pericardium is thus important for residual stress and passive stiffness.

It is widely accepted that the mechanism of the myocardium-pericardium interaction is through the pericardial fluid. In [85] it was found that while increasing the volume of fluid within the pericardial cavity, the pericardial liquid pressure remains constant until it suddenly rises sharply. The observation led to the conclusion that most of the fluid is contained in pericardial sinuses and grooves. This mostly empty space forms the so-called pericardial reserve volume, acting as a buffer against increasing pericardial liquid pressure. Only a small portion of the pericardial fluid remains as a thin film on the interface between parietal and visceral pericardium. In [157], a dye was injected into the pericardial cavity near the apex. Fifteen minutes after injection the dye was almost exclusively found in the interventricular and atrioventricular grooves. This suggests that there is no significant fluid movement on the large surface areas of the ventricular free walls, leaving just a very thin film of fluid with an estimated thickness of less than 0.5 mm.

The mechanical constraint of the pericardium on diastolic cardiac function can be quantified by pericardial pressure. Here it is important to distinguish between liquid pressure and contact pressure [165, 177]. Liquid pressure describes the hydrostatic pressure inside the pericardial fluid and is measured by an open-ended catheter. However, liquid pressure does not describe the constraining effect of the pericardium on the myocardium. The constraint is assessed by contact pressure, which can be measured by a thin, flat, air-filled balloon catheter. In [165] it was found that liquid pressure is substantially below contact pressure unless the pericardium contains a significant amount of pericardial fluid, which happens e.g. due to pericardial effusion. Furthermore, contact stress and thus ventricular restraint was maintained even though pericardial fluid was completely removed and liquid pressure at the epicardial surface was zero. Pericardial fluid therefore acts as lubrication rather than a load balancing mechanism, providing low-friction sliding between pericardium and epicardium [82].

There is less information available on the influence of the pericardium during systole. A pericardial restraining effect during systole would require a tension force to be transmitted by the myocardial-pericardial interface. The restraining effect of the pericardium during systole can be well observed in fish, where the parietal pericardium is almost rigid [86]. It was observed in [170] that pericardial liquid pressure in smooth dogfish is always negative and decreases further during cardiac contraction. In man, [171] found that pericardial liquid pressure also drops during ventricular systole but remains positive throughout the cardiac cycle. However, to the best of the authors' knowledge there is no study on the change of contact pressure during systole. It can be observed from mammal cine MRI that surrounding tissue moves toward the heart during systole, indicating attachment of pericardium and epicardium. It is hypothesized that during systole, through the effect of adhesion, the pericardium remains in contact with the epicardium. This is analogous to the simple experiment of "gluing" two glass plates together with a drop of water. The glass plates can hardly be separated in normal direction but can be easily moved relatively to each other in tangential direction.

3.1.3 Current pericardial boundary conditions

For biventricular geometries, the constraining effect of the pericardium in diastole is accounted for in [30, 125, 126], where a no penetration condition is enforced on the epicardium by a uni-directional penalty contact with a rigid pericardial reference surface. However, this neglects any constraining effect in systole by not allowing the pericardial-myocardial interface to transmit any tension forces. Recently, [158] proposed to completely prohibit movement normal to the epicardial surface, neglecting any elastic effects. The bi-directional elastic constraining effect of the pericardium is accounted for in spring-type boundary conditions, where a spring-dashpot boundary condition is enforced either on the base [156] or on apex and valve annuli [161] with homogeneous-zero Neumann conditions applied to the rest of the epicardium. These boundary conditions are analogous to the external tissue support of the aorta in [133, 134]. However, they do not cover the whole epicardial surface thus representing pericardial-myocardial interaction only partially.

Fewer references exist for four chamber geometries. A common combination of boundary conditions for four chamber geometries are homogeneous-zero Dirichlet conditions on vessel cut-offs and a soft material connected to the apex [10, 30], or springs on the outside of great vessels [114]. In those cases, however, homogeneous-zero Neumann conditions are applied on the remaining epicardial surface, neglecting any influence of the pericardium as in the biventricular case. In [11] *omni-directional* springs acting in all directions are applied to the epicardium, artificially constraining any sliding movement along the pericardial-epicardial interface. To the authors' best knowledge, the most detailed and physiologically correct representation of the pericardium so far is implemented in [56]. The pericardial-myocardial interaction is here modeled by a frictionless sliding, bi-directional penalty contact interaction in normal direction between the epicardium and a solid pericardial reference body. However, this condition is computationally very expensive as it requires solving an adhesial contact interaction problem. It also requires an additional solid body to be created, representing the surrounding tissue. Furthermore, no boundary conditions can be enforced at the great vessels since they are not included in the geometry. Thus, a fixation of the apex was necessary. All models based on four chamber geometries reviewed here lack a quantitative validation through comparison of simulation results to measurements, e.g. medical images like magnetic resonance imaging (MRI).

3.2 Modeling the pericardium

The aim in this work is to propose and justify a pericardial boundary condition that is both realistic and computationally inexpensive. The pericardial model proposed is based on [152] and is sketched in Figure 3.3. Using BACI [181], it was also already applied to a two-chamber geometry in [83]. It consists of a spring and a dashpot in parallel, acting in normal direction to the epicardial surface. Within the tangential, plane frictionless sliding is allowed to account for the lubricating effect of the pericardial fluid. A spring stiffness k and dashpot viscosity c contain the combined effects of serous pericardium, fibrous pericardium, and neighboring tissue. Generalizing the effect on the ventricles, spring compression models the pericardium's constraining effect during passive ventricular filling, whereas spring expansion models the pericardium's support during ventricular systole.

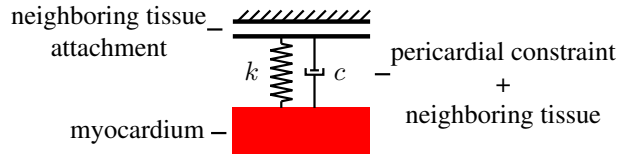


Figure 3.3: Serous pericardium, fibrous pericardium, and neighbouring tissue modeled by a spring (stiffness k) and a dashpot (viscosity c) in parallel. Spring and dashpot act in normal direction on the epicardial surface.

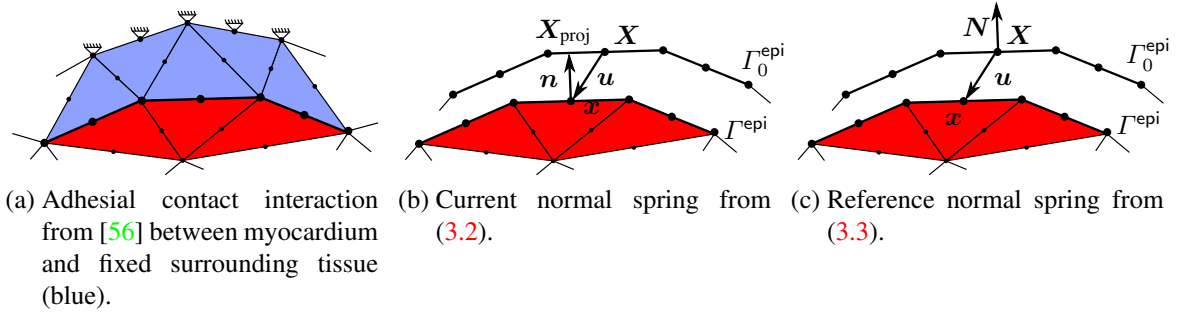


Figure 3.4: Different formulations of interaction between myocardium (red) and pericardium.

Note that only in the limit case of $k \rightarrow \infty$, would yield a boundary condition that penalizes and therefore prohibits any movement in normal direction to the epicardium, as it was recently proposed in [158]. However, the pericardial boundary condition is meant to be used with finite values for k and c , more realistically representing the visco-elastic support of the pericardium and its surrounding tissue and permitting movement normal to the epicardial surface.

In the following, a simple mathematical formulation for the pericardial boundary condition depicted in Figure 3.3 is derived. This derivation is carried out in two steps, where different assumptions are introduced in each step. Only the spring component is considered during the derivation. However, all conclusions hold equivalently for the dashpot component.

The goal is to preserve the features of the detailed pericardial boundary condition in [56] but arrive at a much simpler and cheaper formulation. As reviewed in Section 3.1.3, pericardial-myocardial interaction is modeled in [56] by adhesial contact between the epicardium and an elastic reference body that is fixed in space and representing the surrounding tissue, see Figure 3.4a.

Projection-based spring-dashpot In the first step, the elastic body representing the surrounding tissue in [56] is replaced with springs acting in normal direction to the epicardium. Here, it is assumed that the elasticity of the surrounding tissue is linear with respect to the small movements of the epicardium in its normal direction. Note that the boundary conditions is enforced on the epicardial side of the myocardial-pericardial interface, as this does not require a representation of the actual pericardial surface. Therefore, the pericardium itself is not modeled but the forces acting on the myocardium because of its presence. The elastic potential of a linear spring distributed on the epicardial surface Γ_0^{epi} in current configuration surface is

$$W = \frac{1}{2} \int_{\Gamma_0^{\text{epi}}} k g^2 da \quad (3.1)$$

with spring stiffness k , gap g , and surface integral in current configuration da . The calculation of the gap is illustrated in Figure 3.4b. A point $\mathbf{x} \in \Gamma^{\text{epi}}$ on the current epicardial surface is projected onto the point $\mathbf{X}_{\text{proj}} \in \Gamma_0^{\text{epi}}$ on the reference epicardial surface. The distance between both points projected in the direction of the current outward normal vector \mathbf{n} yields the gap function

$$g = (\mathbf{x} - \mathbf{X}_{\text{proj}}) \cdot \mathbf{n}. \quad (3.2)$$

Though reducing algorithmic and computational demands compared to contact interaction, this boundary condition still requires updates of the normal vector and its linearization with respect to the displacements as well as a projection of each evaluation point onto Γ_0^{epi} in each Newton iteration at each time step.

Reference normal spring-dashpot In a second step, two further simplifications are introduced. Instead of calculating the spring deformation from a projection, the spatial displacements \mathbf{u} are used directly. Furthermore, the epicardial normal vector in reference configuration (i.e. \mathbf{N} instead of \mathbf{n}) is used, neglecting any change in normal direction throughout the simulation. The formulation of the gap in (3.2) is then simplified to

$$g = \mathbf{u} \cdot \mathbf{N} \quad (3.3)$$

The calculation of the gap is illustrated in Figure 3.4c. The simplifications leading to (3.3) are valid for small rotations of the epicardium, an assumption that is not valid for all parts of the epicardium. However, the performance of both formulations (3.2) and (3.3) is reviewed in Section 3.4.

The final expression for the pericardial boundary traction \mathbf{t}_{epi} acting on the epicardial surface then is

$$\mathbf{t}_{\text{epi}} = \mathbf{N} (k_p \mathbf{u} \cdot \mathbf{N} + c_p \dot{\mathbf{u}} \cdot \mathbf{N}). \quad (3.4)$$

For the sake of simplicity, constant boundary condition parameters k_p and c_p are used here on the whole epicardial surface. As it will be shown in the numerical examples, this simple approach already leads to greatly improved results. But of course, a regional distribution based on neighboring organs as visualized in Figure 3.2 is also possible.

3.3 Boundary condition cases

This section contains an overview of the pericardial boundary conditions studied in this work. They are characterized by the potential they add to the cardiac model's total energy $\delta\Pi$, yielding a different weak form for the initial boundary value problems (IBVPs) in each case. For a detailed description of the relevant elastodynamic equations and their discretization, see Sections 2.1 and 2.2, respectively.

Case free The complete absence of boundary conditions on the epicardial surface is modeled by case *free*, where the boundary-value problem is given in its most simple form

$$0 = \delta\Pi, \quad (3.5)$$

adding no additional energy to the IBVP. This boundary condition is frequently used on mono- and biventricular geometries.

Case apex Case *apex* yields the boundary-value problem

$$0 = \delta\Pi + \int_{\Gamma^{\text{apex}}} [k_a \mathbf{u} + c_a \dot{\mathbf{u}}] \cdot \delta \mathbf{u} \, dA \quad (3.6)$$

adding the energy for omni-directional spring dashpots to the energy, where Γ^{apex} is the apical surface. The apical surface is defined as the epicardial surface within 10 mm of the apex. It resembles homogeneous-zero Neumann boundary conditions on $\Gamma_0^{\text{epi}} \setminus \Gamma_0^{\text{apex}}$, i.e., the absence of any pericardial boundary conditions as frequently found in literature [10, 30, 161].

Case pseudo-contact Case *pseudo-contact* uses the projection-based evaluation of the gap function from (3.2), acting on the whole epicardial reference surface Γ_0^{epi} . Due to the projection of epicardial integration points onto the epicardial reference surface, no potential can be given for the boundary condition. The projection algorithm itself is not outlined in this work. For further details, see the work of [150] and [50].

Case pericardium Case *pericardium* uses the simplified evaluation of the gap function from (3.3), acting on the whole epicardial reference surface Γ_0^{epi} . This yields the IBVP

$$0 = \delta\Pi + \int_{\Gamma_0^{\text{epi}}} \mathbf{N} [k_p \mathbf{u} \cdot \mathbf{N} + c_p \dot{\mathbf{u}} \cdot \mathbf{N}] \cdot \delta \mathbf{u} \, dA. \quad (3.7)$$

3.4 Numerical results with a prolate spheroid geometry

In Section 3.2 it was shown how the pericardial boundary condition in case *pericardium* can be derived from adhesive sliding contact by introducing several simplifications. To justify the simplifications made by the pericardial boundary condition, the very simple geometry introduced in Section 2.3.2 of a half prolate spheroid, which roughly represents the shape of the left ventricle, is used with $\pm 60^\circ$ fibers. The reference configuration is shown in Figure 3.5a. The prolate spheroid is able to show the consequences of each boundary condition while being simple enough to isolate the effects of the boundary condition.

3.4.1 Model definition

The total energy of the IBVP is

$$\begin{aligned} \delta\Pi = & \int_{\Omega_0} \rho_0 \ddot{\mathbf{u}} \cdot \delta \mathbf{u} \, dV + \int_{\Omega_0} \mathbf{S} : \delta \mathbf{E} \, dV \\ & + \int_{\Gamma_0^{\text{endo}}} p_v \mathbf{F}^{-\text{T}} \cdot \mathbf{N} \cdot \delta \mathbf{u} \, dA + \int_{\Gamma_0^{\text{base}}} [k_b \mathbf{u} + c_b \dot{\mathbf{u}}] \cdot \delta \mathbf{u} \, dA, \end{aligned} \quad (3.8)$$

with left ventricular pressure p_v and inside surface Γ_0^{endo} . The surface Γ_0^{base} describes where the cardiac base would be for a real cardiac geometry, i.e., the cut-off surface of the prolate spheroid. The stiffness k_b and viscosity c_b of springs and dashpots connected to the base, respectively, represent the attachment to the atria. The model is solely composed of myocardial tissue, using

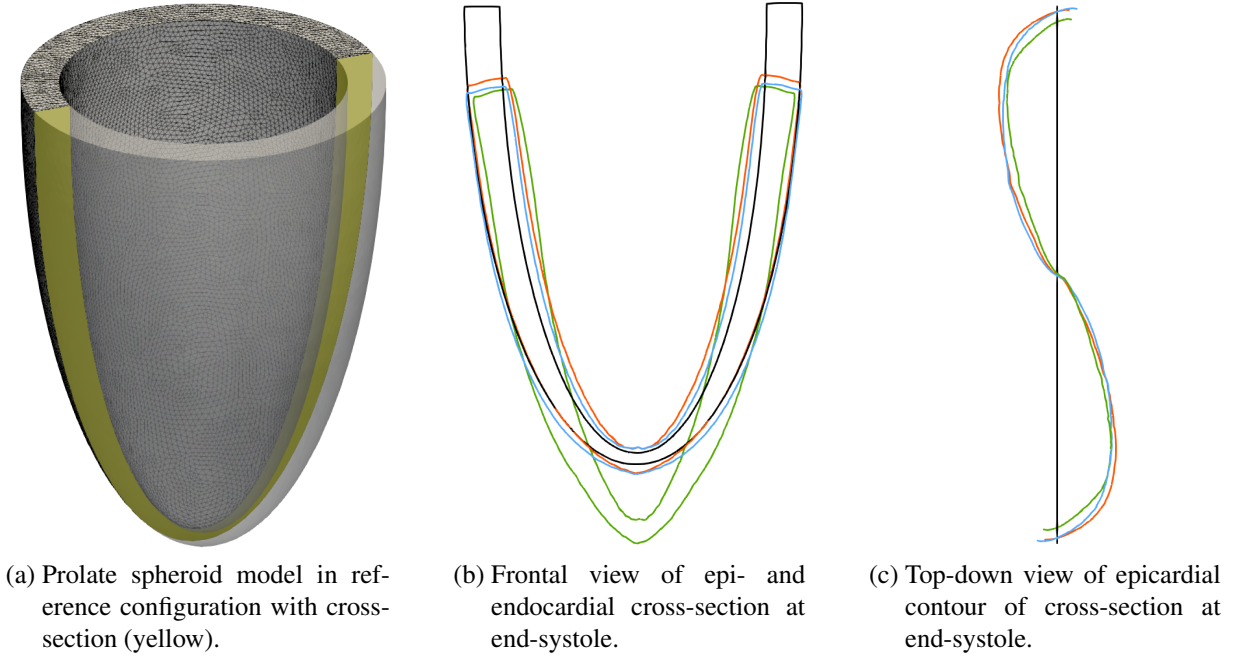


Figure 3.5: Prolate spheroid model in reference configuration (black) with cases *free* (green), *pericardium* (blue), and *pseudo-contact* (orange).

Mooney-Rivlin material ψ_{MR} from (2.62), volumetric penalty $\psi_{\text{vol,a}}$ from (2.63), viscous material ψ_{visco} from (2.65), and active stress \mathbf{S}_{act} from (2.66),

$$\mathbf{S} = \frac{\partial}{\partial \mathbf{E}} (\psi_{\text{MR}} + \psi_{\text{vol,a}}) + \frac{\partial}{\partial \mathbf{E}} \psi_{\text{visco}} + \mathbf{S}_{\text{act}}. \quad (3.9)$$

The parameters of the prolate spheroid model are given in Table A.1. All three boundary condition cases use the same contractility parameter.

3.4.2 End-systolic results

The results of the contraction simulation are shown in Figures 3.5b and 3.5c at end-systole. Displayed is the reference configuration and all three boundary condition cases for a cross-section of the ellipsoid. Figure 3.5b shows in a frontal view the shortening of the ellipsoid with visible epi- and endocardial contours. While the cases *pericardium* and *pseudo-contact* appear very similar with little differences only in radial direction, case *free* exhibits much less longitudinal shortening. Instead, there is a translational movement of the whole geometry instead.

Figure 3.5b shows the epicardial contour of the ellipsoid in a top-down view to observe the twisting motion of the ellipsoid. All three boundary condition cases are very similar. This confirms that the normal springs in cases *pericardium* and *pseudo-contact* in fact allow tangential sliding and do not prohibit any rotational movement, as they are very similar to case *free*. Furthermore, the similarity of cases *pericardium* and *pseudo-contact* shows that the simplified spring formulation (3.3) in case *pericardium* is sufficient to represent the effects of the

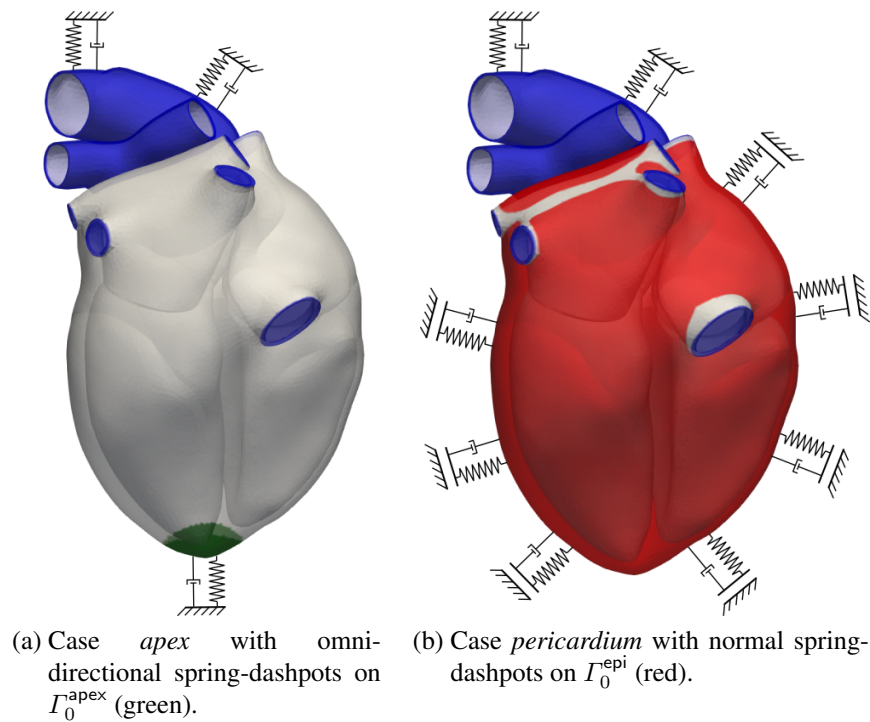


Figure 3.6: Surface definitions for boundary conditions with omni-directional spring-dashpots on Γ_0^{vess} (blue) and homogeneous-zero Neumann boundary conditions (white).

pericardium compared to the more detailed formulation (3.2) in case *pseudo-contact*. The case *pseudo-contact* is thus not considered in all further evaluations in this chapter.

Remark As mentioned in Section 3.2, the projection-based evaluation of the gap function in case *pseudo-contact* is computationally more expensive as the projection and its linearization has to be evaluated in every step of the nonlinear solver. Additionally, it is numerically less robust since the projection can fail or be non-unique for geometries more complex than the prolate spheroid.

3.5 Numerical results with a patient-specific four-chamber geometry

To illustrate the effects of pericardial boundary conditions, the four chamber geometry introduced in Section 2.3.1 obtained *in vivo* from a 33 year old healthy female volunteer is employed here. This section is structured as follows. After proposing the cardiac model in Section 3.5.1, an overview of all methods used in this chapter to quantify the difference between simulation and MRI is given in Section 3.5.2. Next, the model parameters are calibrated for both cases in Section 3.5.3. In the following sections, various outputs of both simulation cases *apex* and *pericardium* are validated with measurements from cine MRI in Section 3.5.5.

3.5.1 Model definition

The total energy of the IBVP is

$$\begin{aligned} \delta\Pi = & \int_{\Omega_0} \rho_0 \ddot{\mathbf{u}} \cdot \delta\mathbf{u} \, dV + \int_{\Omega_0} \mathbf{S} : \delta\mathbf{E} \, dV \\ & + \sum_{\nu \in \{l,r\}} \int_{\Gamma_0^{\text{endo},\nu}} p_V^\nu \mathbf{F}^{-\top} \cdot \mathbf{N} \cdot \delta\mathbf{u} \, dA + \int_{\Gamma_0^{\text{vess}}} [k_v \mathbf{u} + c_v \dot{\mathbf{u}}] \cdot \delta\mathbf{u} \, dA, \end{aligned} \quad (3.10)$$

with left and right ventricular pressures p_V^l and p_V^r , respectively, vessel attachment stiffness k_v and viscosity c_v . The surface Γ_0^{vess} is shown in Figure 3.6. The surfaces $\Gamma_0^{\text{endo},l}$ and $\Gamma_0^{\text{endo},r}$ denote left and right ventricular endocardium, respectively. Different materials from Section 2.4 with volumes as in Figure 2.1 are defined for adipose tissue from (3.11), aorta and pulmonary artery from (3.12), as well as ventricular and atrial myocardium from (3.13):

$$\mathbf{S} = \frac{\partial}{\partial \mathbf{E}} (\psi_{\text{NH}} + \psi_{\text{vol,b}}) + \frac{\partial}{\partial \dot{\mathbf{E}}} \psi_{\text{visco}}, \quad (3.11)$$

$$\mathbf{S} = \frac{\partial}{\partial \mathbf{E}} (\psi_{\text{MR}} + \psi_{\text{vol,b}}) + \frac{\partial}{\partial \dot{\mathbf{E}}} \psi_{\text{visco}}, \quad (3.12)$$

$$\mathbf{S} = \frac{\partial}{\partial \mathbf{E}} (\psi_{\text{exp}} + \psi_{\text{vol,b}}) + \frac{\partial}{\partial \dot{\mathbf{E}}} \psi_{\text{visco}} + \mathbf{S}_{\text{act}}, \quad (3.13)$$

with isotropic Neo-Hooke material ψ_{NH} from (2.60), isotropic Mooney-Rivlin material ψ_{MR} from (2.62), anisotropic exponential material ψ_{exp} from (2.61), volumetric penalty from $\psi_{\text{vol,b}}$ (2.64), viscous material from ψ_{visco} (2.65), and active stress \mathbf{S}_{act} from (2.66). Each material is composed of a hyperelastic and a viscous contribution. Only the myocardial tissue in (3.13) has an additional active stress component \mathbf{S}_{act} . The material parameters and initial conditions of the patient-specific four-chamber model are given in Tables A.5 and A.6, respectively.

The local angles of cardiac myofibers are prescribed at epi- and endocardium of the ventricles. Using harmonic lifting, the fiber vectors \mathbf{f}_0 are interpolated to the interior of the domain by solving a Laplace problem [137]. It is well known that the fiber orientation has a strong impact on passive and active cardiac mechanics [9, 49, 67, 140, 178, 188]. In order to make a more clear statement about the pericardial boundary conditions independently of the fiber orientation and to show the interplay between boundary conditions and fiber orientations, three different fiber distributions are compared in this work: $\pm 50^\circ$, $\pm 60^\circ$, and $\pm 70^\circ$. The first and second angle describe the fiber helix angle at the endo- and epicardial surface, respectively, with respect to the local circumferential axis.

3.5.2 Assessment of cardiac function

In this section, the various methods used throughout this chapter to quantify cardiac function of different simulations are briefly described.

Cine MRI Cine MRI is used with a temporal resolution of ~ 30 ms in four- (Figure 3.7a), three-, and two-chamber views and short axis planes with a slice distance of 8 mm (Figures 3.7b,

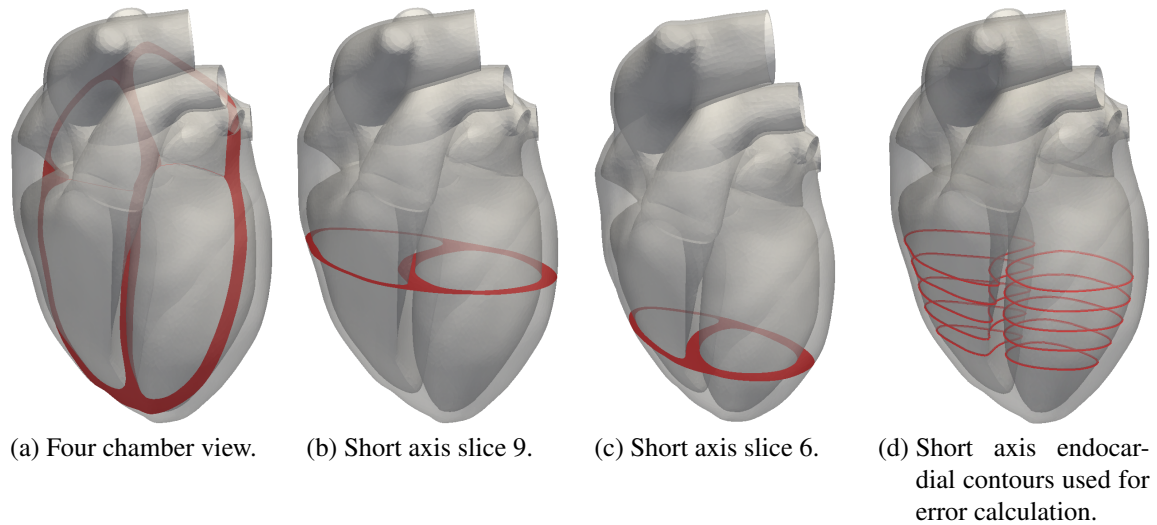


Figure 3.7: Post processing planes for simulations and cine MRI.

3.7c, 3.7d). All cine MRI data used in this work is rigidly registered to the static 3D image taken during diastasis and used for geometry creation to account for any movement of the subject during image acquisition.

It is important to note that the reference configuration of the simulation is obtained from static 3D imaging with a fine isotropic resolution and acquired in free-breathing, as explained in Section 2.3. For the comparison of simulation results to cine MRI however, one has to rely on sparsely distributed images acquired in expiration breath-hold. The used image types rely on different MRI acquisition parameters and pulse sequences. Therefore, it is impossible for the simulation to match the cine MRI data perfectly, even in reference configuration. This error however is usually smaller than the approximation error of the cardiac model.

Left ventricular volume A reference for left ventricular volume is obtained by manually segmenting the left endocardial surface obtained from the short axis cine MRI stack at all time steps. The sum of areas is added in each short axis slice multiplied by the slice thickness. The volume is cut at the top and bottom according to the limits of the left ventricle at each time step, as observed in two chamber and four chamber views.

In order to be fair and not to introduce a bias towards the more realistic pericardial model, for each simulation, the contractility σ_0 is calibrated. It is a key parameter describing cardiac elastodynamics, resembling the asymptotic active fiber stress introduced in Section 2.4.3. It controls maximum deformation during systole. In order to make simulations comparable, σ_0 is adapted for each combination of boundary condition and fiber orientation to match the left ventricular volume at end-systole as segmented from cine MRI of $V_{\min} = 57$ ml. The heart thus yields a stroke volume of 75 ml and an ejection fraction (EF) of 57%.

Atrioventricular plane displacement (AVPD) The movement of the left or right plane of the valve separating atrium and ventricle in long axis direction during the cardiac cycle is described by AVPD. For left and right ventricle those valves are termed mitral and tricuspidal

valve, respectively. As a scalar parameter, AVPD at end-systole is an important clinical parameter to describe and predict cardiac vitality [28, 186].

AVPD is evaluated in this work as it gives a quantitative measurement of the displacements in long axis direction. The displacements of the left and right atrioventricular plane are extracted semi-automatically from two, three, and four chamber cine MRI using the freely available software Segment version 2.0 R5585 [80]. In the simulations, the displacements are averaged over all nodes on the valve plane (see the red planes in Figure 2.1b) and project them onto the long axis direction. A positive sign indicates a movement of the base towards the apex.

Spatial error Displacements are validated in long axis direction using AVPD as measurement. To validate radial displacement, the movements of cardiac surfaces in simulations are compared to the ones from short axis cine MRI. For comparison, the left and right endocardium are selected, as it shows how pericardial boundary conditions, prescribed on the epicardium, act on the interior of the domain.

For each MRI time step (temporal resolution ~ 30 ms) the closest simulation time step is selected (temporal resolution 1 ms). Spatially, the simulations' displacement results are extracted at the same positions where the cine MRI slices were acquired. This is possible since the MRI scanner's global coordinate system is used for all images and the simulation. This method can be thought of as taking a virtual cine MRI of the simulation. This yields an Eulerian description of motion, as the observer is fixed in space. The difference of simulated displacements to cine MRI data was used previously, e.g. in [30] to estimate local tissue contractility. Note that this technique does not allow to track rotations of the left ventricle due to its rotational symmetry.

The contours of left and right endocardium are manually segmented from short axis cine MRI for slices 5 to 9 at all MRI time steps, see Figure 3.7d. These slices are selected because the myocardium is recognizable for all MRI time steps and not disturbed by either apex or AVP. The function A converts both MRI and simulated endocardial contours $\mathbf{d}_{\text{MRI}}^s$ and \mathbf{d}^s , respectively, to binary images with a resolution of $1 \times 1 \text{ mm}^2$ for every slice s . The Dice metric is used to compare both binary images via

$$\epsilon = 1 - \frac{1}{5} \sum_{s=5}^9 \frac{2 |A(\mathbf{d}_{\text{MRI}}^s) \cap A(\mathbf{d}^s)|}{|A(\mathbf{d}_{\text{MRI}}^s)| + |A(\mathbf{d}^s)|} \in [0, 1] \quad (3.14)$$

where $|\bullet|$ denotes the area of the binary image. As mentioned above, due to the geometry and displacements being from two different MRI sequences, they don't match in reference configuration. The error $\epsilon(t = 0) \approx 0.08$ at thus contains a combined error of image acquisition and image segmentation.

Ventricular-atrial interaction Utilizing a four chamber geometry allows us to investigate the interaction between ventricles and atria. Specifically, the influence of ventricular contraction on atrial filling should be studied. Therefore, atrial volumes are analyzed over time. Furthermore, left and right atrial volumes were segmented at ventricular diastasis and end-systole from isotropic 3D MRI.

Pericardial contact stress The stresses transmitted between the epicardial boundary conditions and the myocardium are evaluated for both cases *apex* and *pericardium*. Different averaged

stresses are used for both cases to quantify the constraining effect of each boundary condition. In case *apex* the stresses are concentrated on the small apical area and acting in any direction. Thus, the stress vectors of the apical boundary condition are integrated over the apical surface and normalized by the apical area to obtain the mean apical stress vector

$$\bar{\mathbf{t}}_{\text{apex}}(t) = \frac{\int_{\Gamma_0^{\text{apex}}} \mathbf{t}_{\text{apex}} \, dA}{\int_{\Gamma_0^{\text{apex}}} 1 \, dA}, \quad \mathbf{t}_{\text{apex}} = k_a \mathbf{u} + c_a \dot{\mathbf{u}}. \quad (3.15)$$

In case *pericardium* the boundary stresses are distributed over the whole epicardial surface and acting only in normal direction. Therefore, the (signed) normal component t_{epi} is extracted and integrated over the epicardial surface to obtain the mean scalar pericardial stress

$$\bar{t}_{\text{epi}}(t) = \frac{\int_{\Gamma_0^{\text{epi}}} t_{\text{epi}} \, dA}{\int_{\Gamma_0^{\text{epi}}} 1 \, dA}, \quad t_{\text{epi}} = k_p \mathbf{u} \cdot \mathbf{N} + c_p \dot{\mathbf{u}} \cdot \mathbf{N}, \quad (3.16)$$

normalized by the epicardial area.

3.5.3 Selection of pericardial parameters

Since in case *apex* the purpose of the apical boundary condition is fixing the apex throughout cardiac contraction, a high spring stiffness is chosen, permitting only little motion. For case *pericardium*, the parameters k_p and c_p describing pericardial stiffness and viscosity, respectively, need to be calibrated. The chosen value for pericardial viscosity has on its own, i.e., without parallel spring, only little influence on cardiac dynamics. However, in combination with the spring, it prevents unphysiological oscillations of the heart. Pericardial stiffness controls the amount of displacement perpendicular to the epicardial surface and thus the radial motion of the myocardium.

In the following, the influence of the parameter k_p on the contraction of the heart is investigated. For this study, only the $\pm 60^\circ$ fiber distribution is chosen, as it is commonly used in cardiac simulations, see e.g. [30, 83, 119]. The following parameter values are tested:

$$k_p \in \{0.1, 0.2, \dots, 1.0, 1.5, \dots, 5.0\} \left[\frac{\text{kPa}}{\text{mm}} \right] \quad (3.17)$$

For each choice of k_p , active stress is calibrated to yield the same end-systolic volume as measured from MRI. All parameters except k_p are kept constant throughout this study. Specifically, the timing of ventricular systole is not adjusted to match the volume curve from MRI. However, since all simulations reach the end-systolic state, it is used in this section for quantitative comparisons.

The results of the calibration are shown in Figure 3.8, where maximum active stress is plotted against pericardial stiffness. For comparison, the result for case *apex* with $\pm 60^\circ$ fibers is included. Active stress, required to yield identical end-systolic volume, rises strongly with increasing pericardial stiffness. The temporal maximum of pericardial contact stress averaged over the epicardium also increases strongly with k_p , as shown in Figure 3.9. For high k_p , contact stress has the same order of magnitude as active stress and exceeds maximum left ventricular pressure.

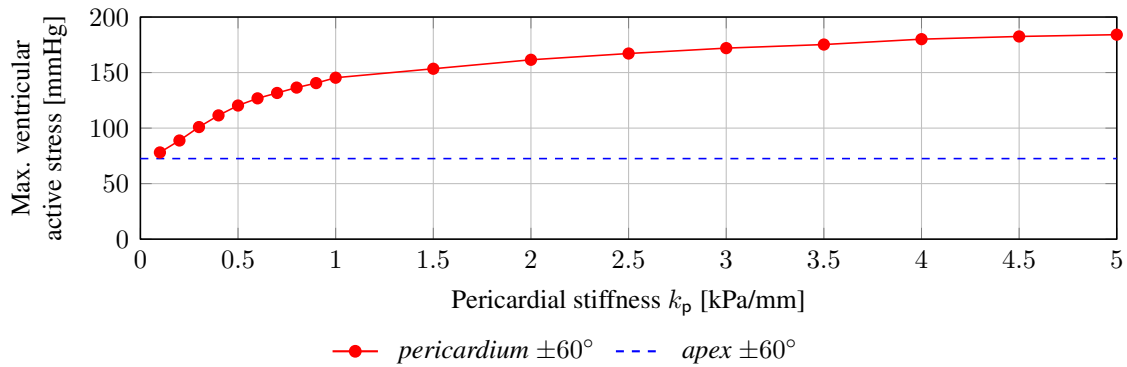


Figure 3.8: Maximum ventricular active stress σ_v calibrated to yield identical end-systolic volume. Shown for case *pericardium* with varying pericardial stiffness compared to case *apex*, both with $\pm 60^\circ$ fiber distributions.

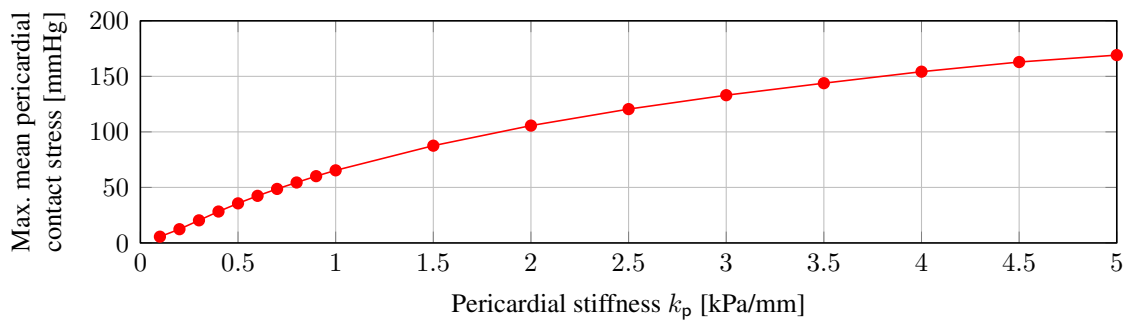


Figure 3.9: Maximum of mean pericardial contact stress \bar{t}_{epi} for case *pericardium* with varying pericardial stiffness and $\pm 60^\circ$ fiber distributions.

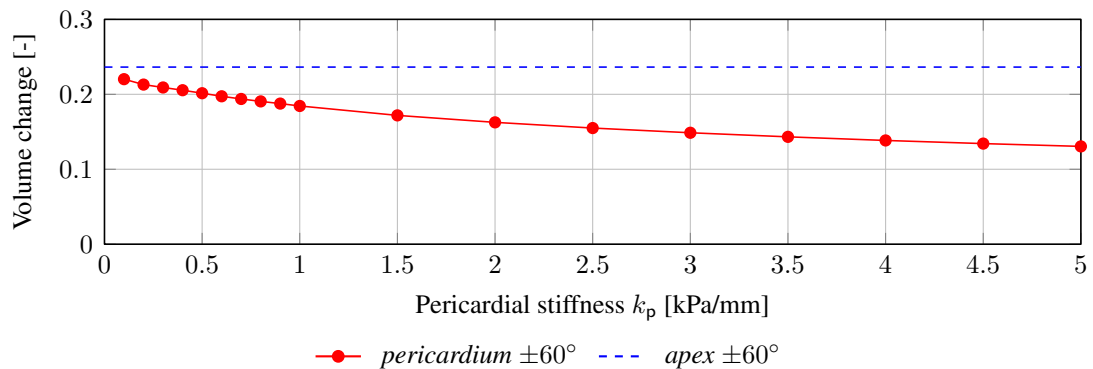


Figure 3.10: Volume change for case *pericardium* with varying pericardial stiffness compared to case *apex*, both with $\pm 60^\circ$ fiber distributions.

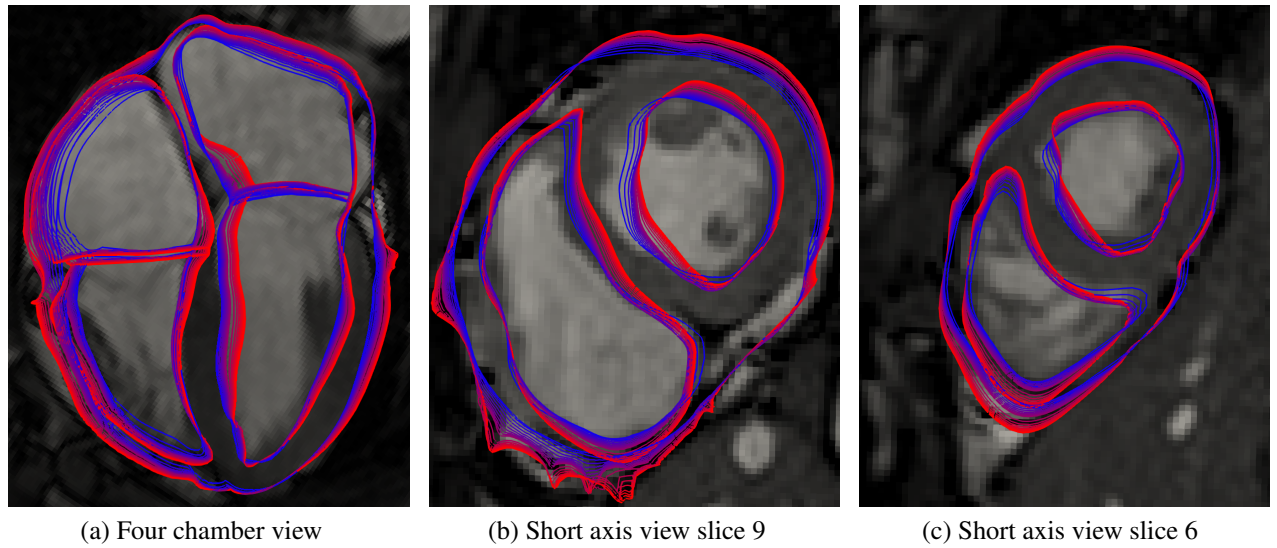


Figure 3.11: Cine MRI at end-systole for case *pericardium* with $\pm 60^\circ$ fiber distribution from $k_p = 0.1$ (blue) to $k_p = 5.0$ (red). Views as defined in Figure 3.7. MRI courtesy of R. Chabiniok, J. Harmer, E. Sammut, King's College London, UK.

For small k_p , it has the same order of magnitude as atrial pressure, which experimentally shown to be a good predictor for pericardial contact stress [177].

Figure 3.10 shows the volume within the pericardial cavity, calculated as the combined volume of all tissue inside the pericardium and the volume within the four cardiac cavities. Case *pericardium* yields a lower volume change than case *apex* and decreases further with increasing k_p .

The end-systolic state of the simulations is shown in Figure 3.11 compared to MRI. The images contain all simulated variants for k_p , where the color changes continuously from $k = 0.1$ kPa/mm (blue) to $k = 5.0$ kPa/mm (red). All MRI views in Figure 3.11 show clearly that pericardial stiffness controls radial displacement of the epicardium. High stiffness values result in less radial inward motion during ventricular systole than visible in cine MRI and vice versa. This is also well observable in Figure 3.11a for the atria in four-chamber view. The short axis views in Figures 3.11b and 3.11c additionally show that the interventricular septum is stretched and rotated as compared to MRI for high k_p .

The spatial error at left and right ventricular endocardium is shown in Figures 3.12a and 3.12b, respectively. The increasing mismatch between simulations and MRI for increasing k_p as visible in Figures 3.11b and 3.11c is quantified as increasing spatial error.

Left and right AVPD is displayed in Figures 3.12c and 3.12d, respectively. In the left ventricle, i.e., at the mitral valve, AVPD is not very sensitive to the choice of k_p . However, it is higher than in case *apex* but much lower than in MRI. For the right ventricle, i.e., at the tricuspid valve, AVPD is greatly enhanced by increasing k_p towards the value measured in MRI. An identical trend is observable for left and right atrial volume in Figures 3.12e and 3.12f, respectively.

To conclude the parametric study for pericardial stiffness, the value $k_p = 0.2$ kPa/mm is chosen for all following simulations. It offers a low spatial error at the ventricles but has higher atrial volume and AVPD than the simulation with $k = 0.1$ kPa/mm.

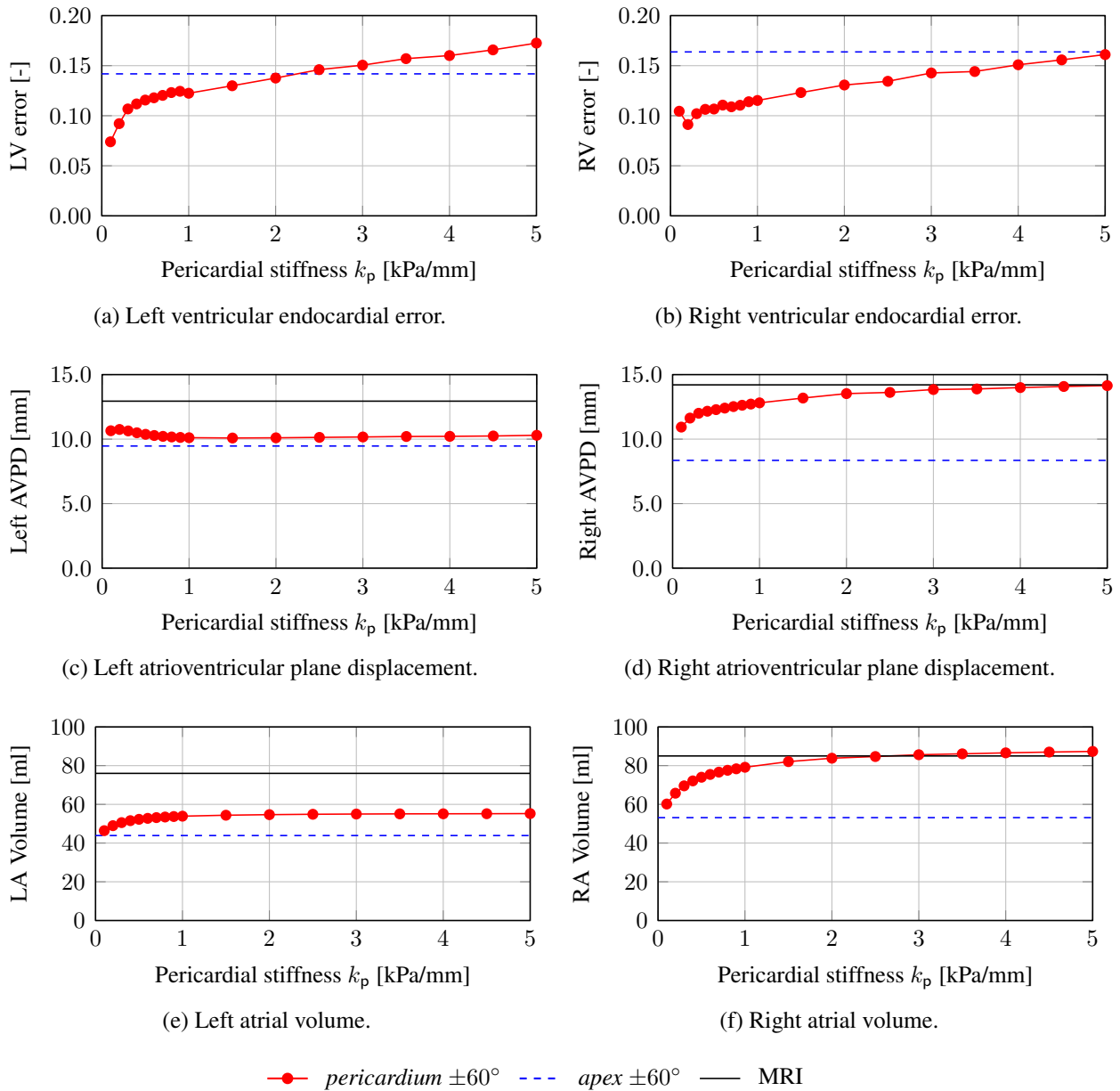


Figure 3.12: Kinematic scalar cardiac quantities at end-systole for case *pericardium* with varying pericardial stiffness $k_p \in [0.1, 5.0]$ compared to case *apex*, both with $\pm 60^\circ$ fiber distributions and MRI.

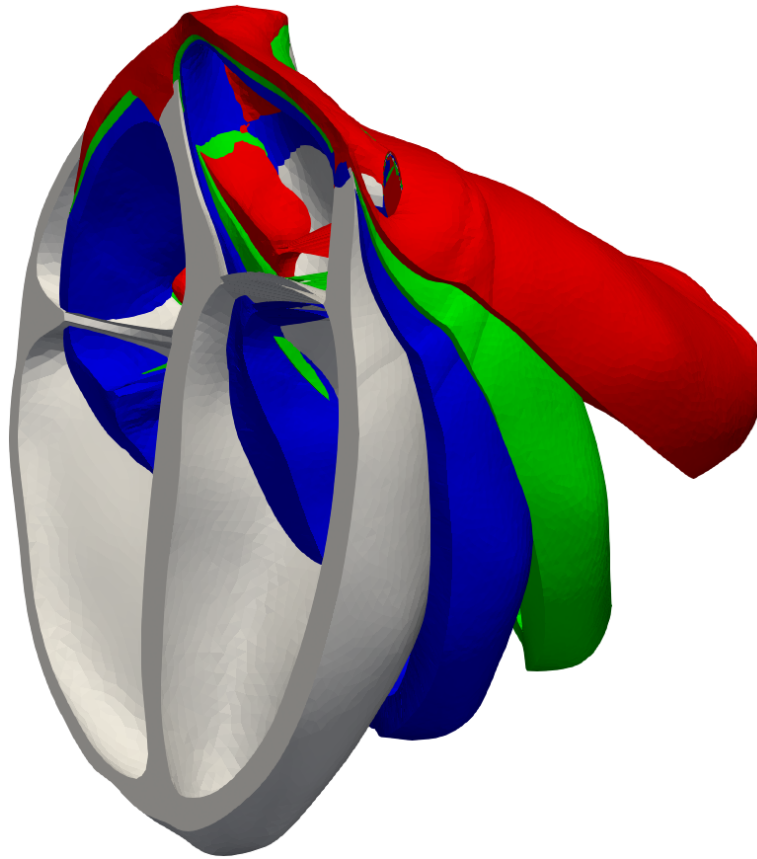


Figure 3.13: End-systolic results for case *free* with different fiber orientations, cut in four chamber-view: Reference configuration (white), $\pm 50^\circ$ (red), $\pm 60^\circ$ (green), and $\pm 70^\circ$ (blue).

Remark The results for a cardiac contraction using boundary condition case *free* is shown in Figure 3.13 for three fiber directions together with the reference configuration. There is a large, unrealistic bending deformation associated with contraction. Case *free* is thus excluded from further evaluation and not recommended as a boundary condition for cardiac simulations.

3.5.4 Model personalization

In order to investigate the influence of pericardial boundary conditions, simulations with different pericardial boundary condition on the epicardial surface Γ_0^{epi} are compared. The simulations will be denoted by *apex* and *pericardium* in the following, visualized in Figure 3.6a and Figure 3.6b, respectively. See Table 3.1a for an overview of the used parameters.

All simulations are carried out using three different fiber distributions, i.e., $\pm 50^\circ$, $\pm 60^\circ$, and $\pm 70^\circ$. The results for the calibration of σ_0 are shown in Table 3.1b. Note that here the maximum value σ_v of active stress is shown instead of σ_0 .

It can be observed that σ_v is larger in case *pericardium* than in case *apex*. Furthermore, σ_v increases from $\pm 50^\circ$ to $\pm 70^\circ$ fibers for more vertical fiber distributions.

	Γ_0^{apex}		Γ_0^{epi}	
	k_a [kPa/mm]	c_a [kPa·s/mm]	k_p [kPa/mm]	c_p [kPa·s/mm]
<i>apex</i>	$1.0 \cdot 10^3$	$1.0 \cdot 10^{-2}$	0	0
<i>pericardium</i>	0	0	0.2	$5.0 \cdot 10^{-3}$

(a) Spring stiffness and dashpot viscosity on apical and epicardial surface.

	σ_v [kPa]			t_{sys} [ms]		
	$\pm 50^\circ$	$\pm 60^\circ$	$\pm 70^\circ$	$\pm 50^\circ$	$\pm 60^\circ$	$\pm 70^\circ$
<i>apex</i>	63.5	72.4	91.0	143	155	172
<i>pericardium</i>	79.4	90.7	129	161	170	193

(b) Maximal myocardial active stress σ_v and ventricular activation time t_{sys} .

Table 3.1: Calibrated parameters for simulation cases *apex* and *pericardium* and different fiber orientations.

The parameters t_{sys} , t_{dias} , α_{max} , α_{in} defining cardiac contraction via the active stress component from Section 2.4.3 are personalized. The onset of systole and diastole, t_{sys} and t_{dias} , as well as the myofiber activation and deactivation rates, α_{max} and α_{in} , are adapted to the left ventricular volume curve for ventricles and atria. Here, parameters for the atria are fitted from the interval $t \in [0, 0.2 \text{ s}]$ and $t \in [0.2 \text{ s}, 0.9 \text{ s}]$ for the ventricles. The material parameter η controlling the viscosity of the tissue within the pseudo-potential ψ_{visco} from (2.65) is fitted during ventricular diastole, i.e., $t \in [0.5 \text{ s}, 0.9 \text{ s}]$. Since active stress is zero during this interval, viscosity controls the relaxation speed of the model. A summary of all calibrated model-specific material parameters is given in Table 3.1. For parameters identical in all models see Table A.5.

3.5.5 Validation with cine MRI

Results for both boundary cases *apex* and *pericardium* are extensively compared to cine MRI in this section. Firstly, scalar Windkessel outputs are evaluated and simulated volume curves are compared to MRI in Section 3.5.5.1. A qualitative evaluation of displacement results is given in Section 3.5.5.2 by comparing end-systolic simulation results to cine MRI frames at multiple views. The differences in pumping motion for simulation cases *apex* and *pericardium* is quantified by comparing the displacements of the left and right atrioventricular plane to MRI in Section 3.5.5.3. The interplay between ventricles and atria with and without the presence of pericardial boundary conditions is investigated in Section 3.5.5.4. In Section 3.5.5.5 a spatial error is calculated for the left and right endocardium to quantify the overall approximation quality. Finally, the contact stress of the pericardial boundary condition of case *pericardium* is evaluated in Section 3.5.5.6.

3.5.5.1 Scalar Windkessel results

Firstly, in Figure 3.14 the scalar outputs volume (left) and pressure (right) of the left ventricle of the Windkessel model are compared. As explained in Section 3.5.3, the contractility σ_0 was cal-

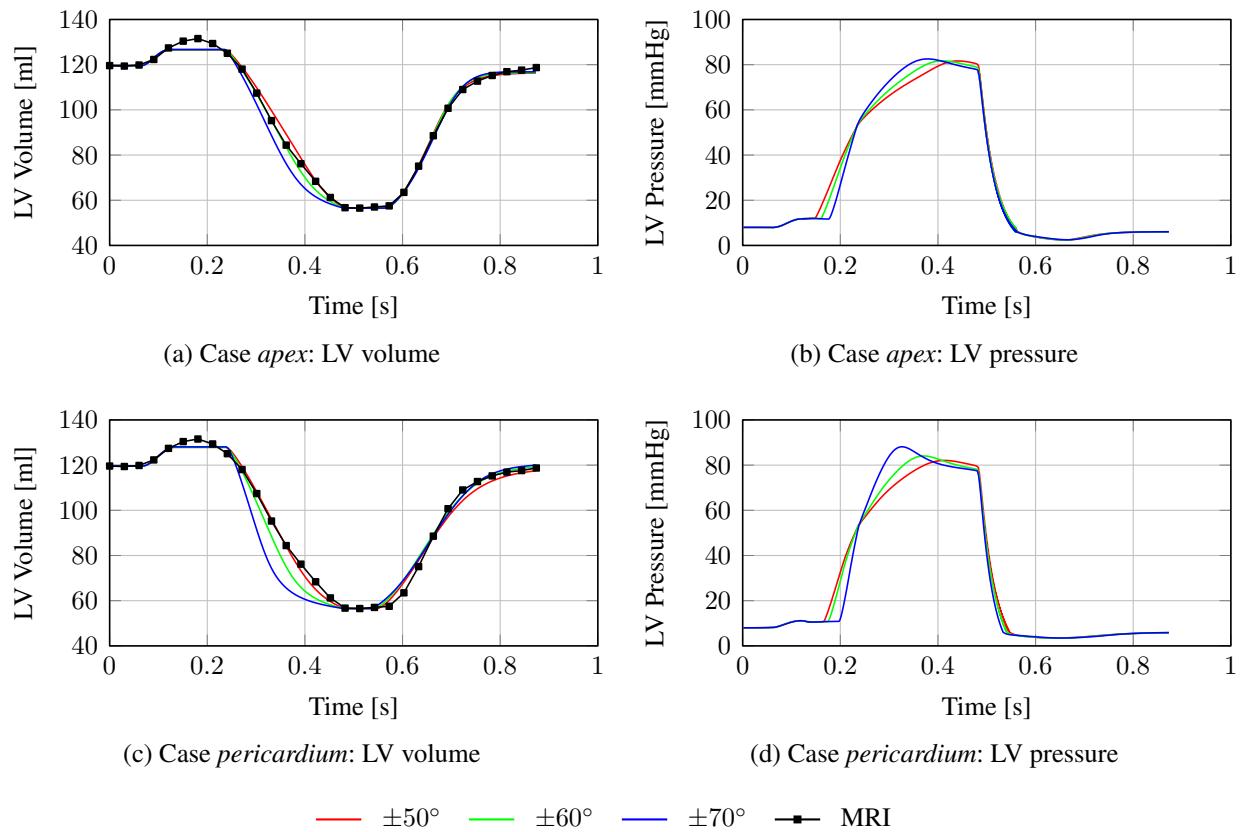


Figure 3.14: Simulation results for volume (left) and pressure (right) of the left ventricle (LV) for boundary condition cases *apex* (top) and *pericardium* (bottom). Volume results are compared to cine MRI.

ibrated in all simulations to match end-systolic volume as segmented from cine MRI. Therefore, in Figures 3.14a and 3.14c the volumes of MRI and all simulations match at $t = 0.51$ s. Furthermore, although they result from simulations with very different boundary conditions and fiber orientations the volume curves are very similar. The maximum volume due to atrial contraction and the prescribed atrial pressure in Figure 2.9b is similar in both cases but lower than in MRI. As for the volume curves, the pressure curves in Figures 3.14b and 3.14d are remarkably similar despite the different simulation settings. Because case *pericardium* exhibits a faster decay in volume during systole than in case *apex*, the pressure peak during systole is more pronounced.

3.5.5.2 Displacements at end-systole

As demonstrated in Section 3.5.5.1, the results of the scalar output parameters left ventricular volume and pressure are mostly invariant to changes in boundary conditions or fiber orientation. Validating the elastodynamical model of cardiac contraction thus requires a comparison of displacement results to spatially distributed MRI observations, see Figure 3.15. The reference configuration (diastasis) of the simulation is shown in Figures 3.15a, 3.15b, 3.15c. The MRI frames at end-systole are compared to the simulation results using the four chamber view, see

Figures 3.15d and 3.15g, and two different short axis views, see Figures 3.15e, 3.15h, 3.15f, 3.15i. The location of the view planes is visualized in Figures 3.7a, 3.7b, 3.7c.

For case *apex*, there is a radial inward movement of the myocardial wall. In Figure 3.15d, this is especially visible at the right atrial free wall and at the left and right epicardial free wall. There is a large mismatch between simulation and MRI at the interatrial septum. Due to the radial contraction motion, atrioventricular plane displacement (AVPD) is lower than in MRI. The fixation of the apex in case *apex* causes a mismatch between simulations and MRI at the apex, as the apex slightly moves during cardiac contraction. The interventricular septum's matches well with MRI in Figures 3.15e and 3.15f. However, the mismatch of epicardial contours is clearly visible and sensitive to fiber orientation.

Comparing Figures 3.15d and 3.15g, the influence of the pericardial boundary condition becomes clearly visible. For case *pericardium* in Figure 3.15g, it can be observed that the epicardial contour matches the MRI much closer than case *apex* in Figure 3.15d for any fiber orientation. The movements of the left and right atrioventricular plane also match well with MRI, for both orientation and displacement in normal direction. The displacements at the apical region are also predicted more accurately than in case *apex*. Comparing the shape of the right ventricle in Figures 3.15d and 3.15g, one can observe that the pumping motion of the right ventricle in case *apex* is the result of radial inward movement, whereas in case *pericardium* it is the result of a downward movement of the atrioventricular plane. The same observation holds for a less visible degree for the left ventricle. Through the constraining effect of the pericardium, the atria are visibly more stretched than in case *apex*. There is also an influence of the fiber orientation in case *pericardium*, although it is more bound to the endocardial surfaces. The more vertical the fiber orientation, i.e., from $\pm 50^\circ$ (red) to $\pm 70^\circ$ (blue), the larger the displacements of the atrioventricular planes and the smaller the displacement of the apex in anterior direction. There are some mismatches between simulation and MRI at the interatrial and interventricular septum but less pronounced than in case *apex*. The deviation at the interventricular septum can be observed for short axis slice 9 in Figure 3.15h. For short axis slice 6 in Figure 3.15i there is a good agreement with simulation and MRI at all regions of the left and right myocardium.

3.5.5.3 Atrioventricular plane displacement

The AVPDs in simulations and MRI are compared in Figure 3.16. The left and right AVPD from MRI (black) is zero at the beginning and at the end of the cardiac cycle. During atrial systole, the left and right atrioventricular planes (AVP) move away from the apex and reach both their minimal value at atrial end-systole at $t = 0.17s$. Followed by ventricular systole, the AVPs move towards the apex and both reach their maximal value at ventricular end-systole at $t = 0.51s$.

During atrial systole for $t \in [0, 0.25s]$, negative AVPD, i.e., movement of the AVP towards the atria, is less pronounced and delayed in both cases as compared to MRI. However, extremal AVPD at atrial end-systole is slightly higher in case *pericardium* than in case *apex*.

Comparing the AVPDs for cases *apex* and *pericardium* in Figures 3.16a, 3.16c, 3.16b, 3.16d, one can observe that in both cases the maximum AVPD depends on fiber orientation: The maximum AVPD increases from horizontal $\pm 50^\circ$ fibers (red) to vertical $\pm 70^\circ$ fibers (blue). The dependence on fiber orientation is more pronounced in case *apex* than in case *pericardium*. In general, AVPD is slightly higher in case *pericardium* than in case *apex* but still underestimates measurements from MRI.

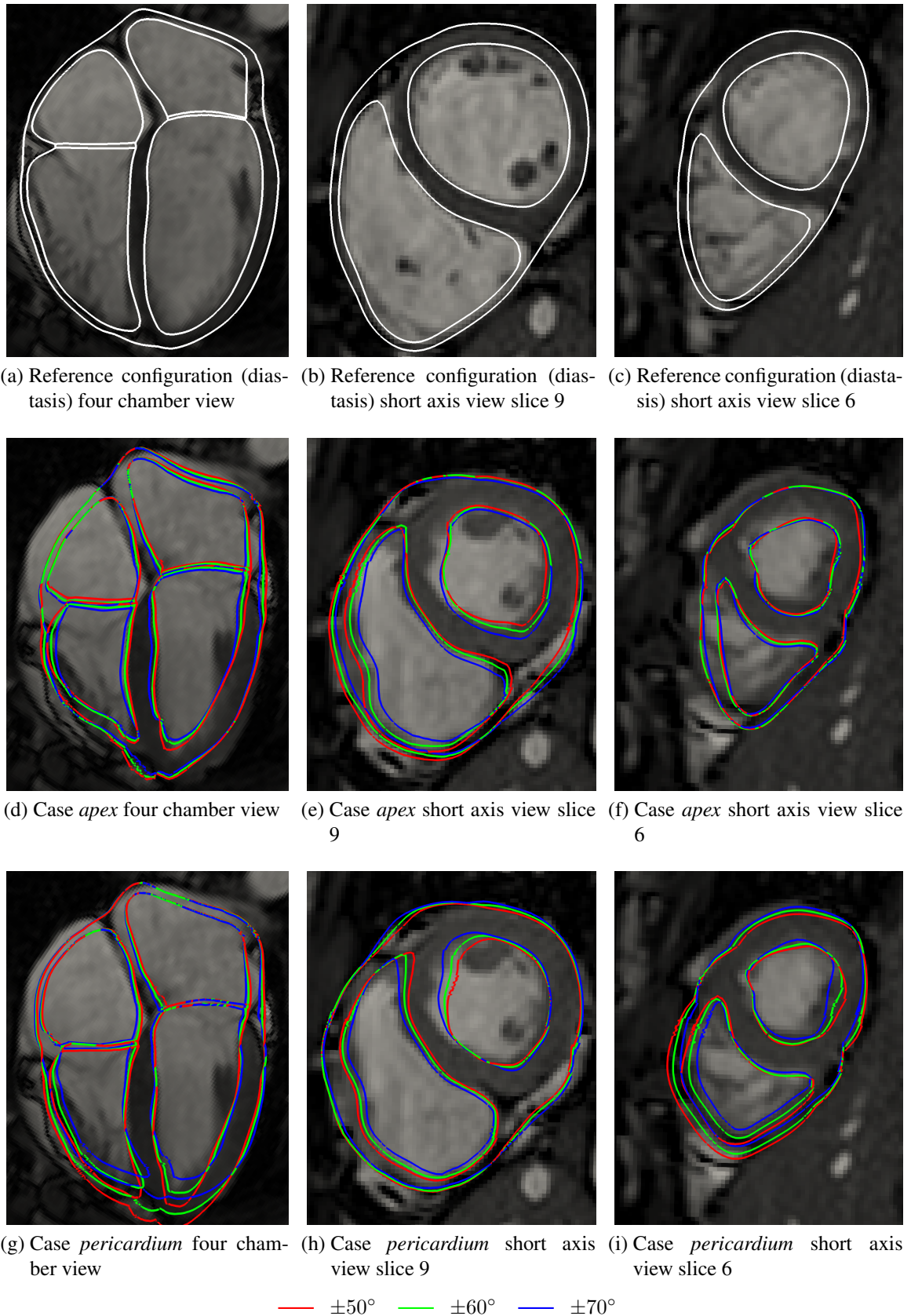


Figure 3.15: Reference configuration (diastasis) as well as simulation results and cine MRI at end-systole in four chamber view and short axis views as defined in Figure 3.7. MRI courtesy of R. Chabiniok, J. Harmer, E. Sammut, King's College London, UK

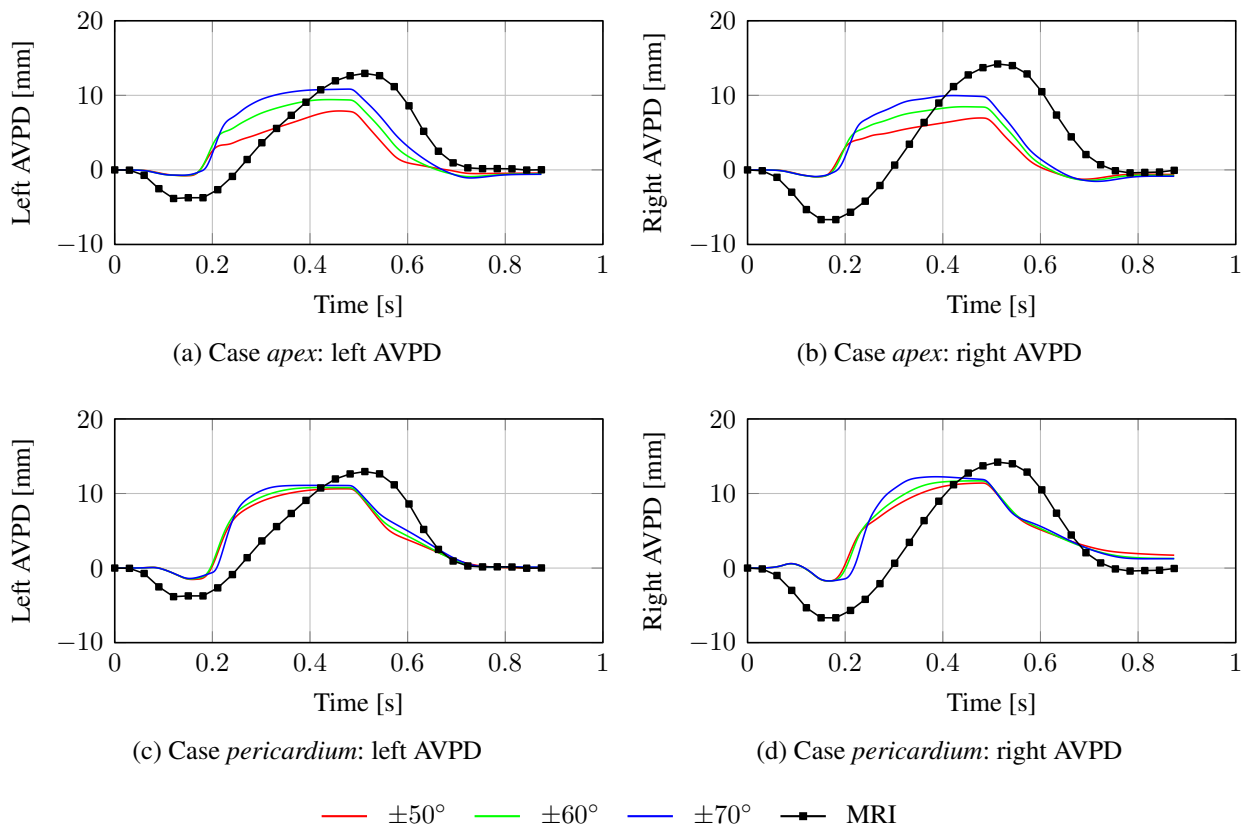


Figure 3.16: Simulated atrioventricular plane displacement for left and right ventricle compared to cine MRI.

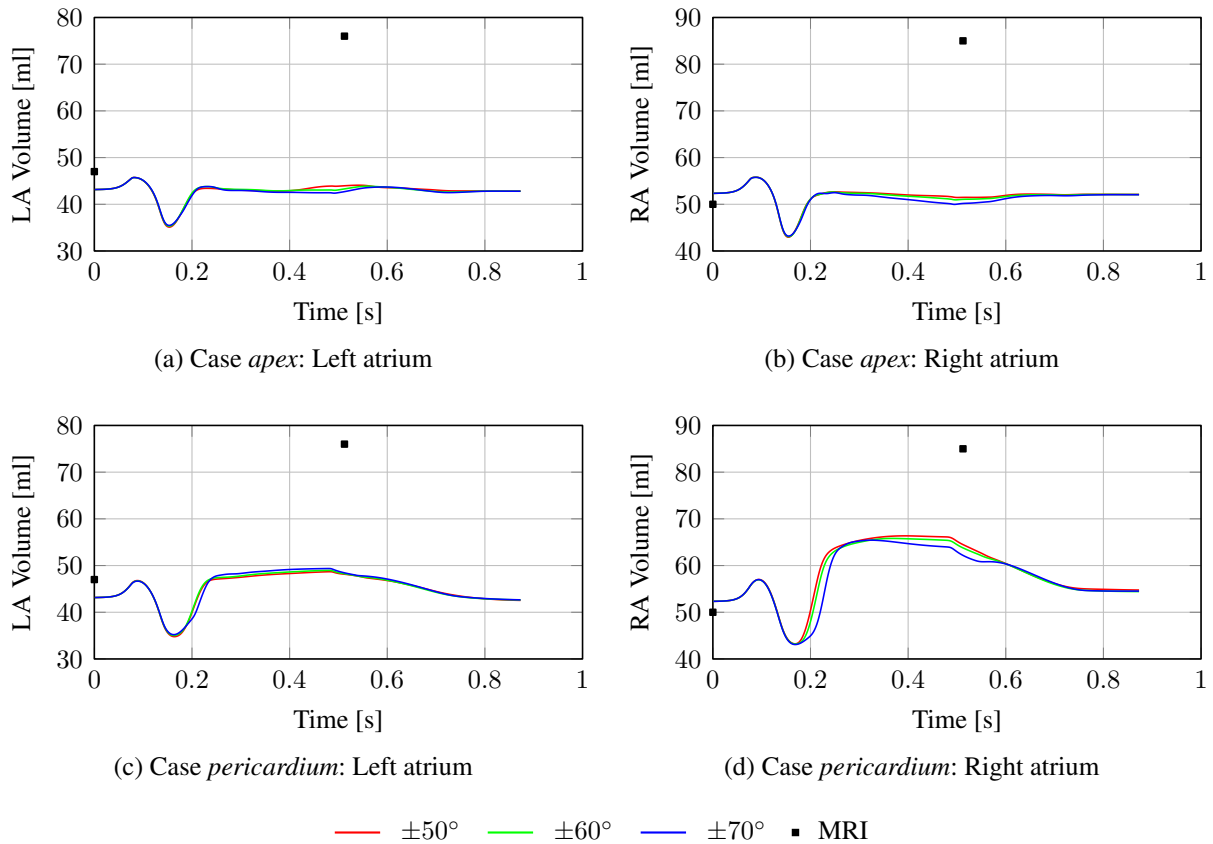


Figure 3.17: Simulated volume curves for left and right atrium compared to 3D MRI at ventricular diastasis and end-diastole.

3.5.5.4 Ventricular-atrial interaction

Atrial systole is visible by the drop in atrial volume in both cases. Passive atrial filling is non-existent in case *apex*, as the volumes in Figures 3.17a and 3.17b stay constant during ventricular systole. This is also visible at the end-systolic four-chamber view in Figure 3.15d. For $\pm 70^\circ$ fibers, the right atrium is even slightly emptied during ventricular systole, as observed in Figure 3.17b. Atrial filling can be observed for case *pericardium* in Figures 3.17c and 3.17d. Both atria are visibly filled during ventricular systole, although the maximum atrial volume remains smaller than in MRI.

3.5.5.5 Spatial error

For case *apex* in Figures 3.18a and 3.18b the error decreases in both ventricular endocardia during contraction towards end-systole at $t = 0.51$ and rises during ventricular contraction and relaxation. This observation suggests that the end-systolic state is approximated well, but mismatches between contraction and relaxation velocity cause an error increase. Errors at the end of the simulation higher than the ones at $t = 0$ suggest that the state at the end of the simulation

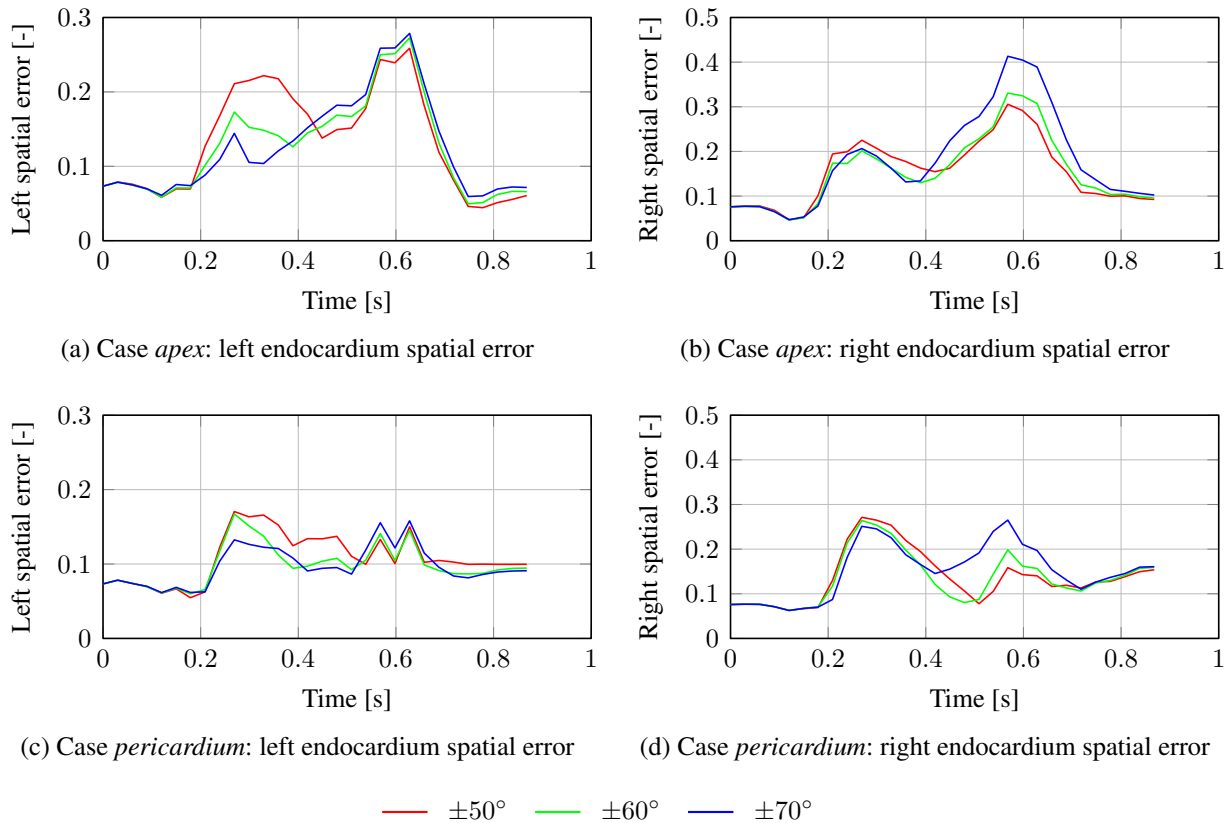


Figure 3.18: Relative spatial error of simulation results and cine MRI at left and right endocardium.

differs from the reference configuration. The overall error is much lower in case *pericardium* than in case *apex*.

3.5.5.6 Boundary stresses

Both scalar boundary stresses $\bar{t}_{\text{apex}} = \|\bar{\mathbf{t}}_{\text{apex}}\|_2$ and \bar{t}_{epi} are visualized in Figure 3.19 over time for all fiber orientations. It can be observed that apical stress in case *apex* is orders of magnitude higher than pericardial stress in case *pericardium* and more dependent on fiber orientation. In case *pericardium*, positive values of \bar{t}_{epi} indicate predominant tensile stresses between epicardium and pericardium. It can be seen that the mean pericardial stress in Figure 3.19b is a compressive stress for most of the cardiac cycle, except at the end of systole and onset of diastole.

Boundary stresses are visualized in Figure 3.20. For case *apex*, the mean stress vectors $\bar{\mathbf{t}}_{\text{apex}}$ for all three fiber distributions are shown in Figure 3.20a at $t = 0.45$ and scaled according to their magnitude. Fiber orientation has not only a strong influence on the magnitude but also on the direction of the mean apical stress.

The local distribution of pericardial contact stress with $\pm 60^\circ$ fibers at end-systole is shown in Figure 3.20b in reference configuration. At end-systole, compressive as well as tensile stresses

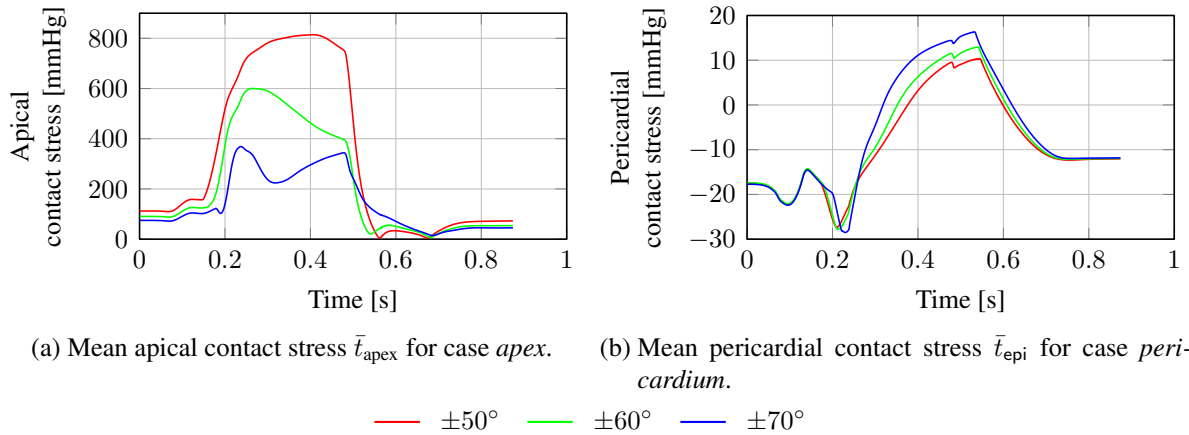


Figure 3.19: Stresses on the epicardial surface caused by boundary conditions.

occur. Stresses are centered around a tensile stress of 20 mmHg. Areas of high compressive stresses are at the left atrium, the anterior and posterior right ventricle, the posterior left ventricle, and the anterior left ventricular apex. Areas of high tensile stresses are the right ventricle close to the anterior part of the right ventricular outflow tract and the left and right ventricular free wall. Overall, pericardial contact stress is evenly distributed around the epicardial surface.

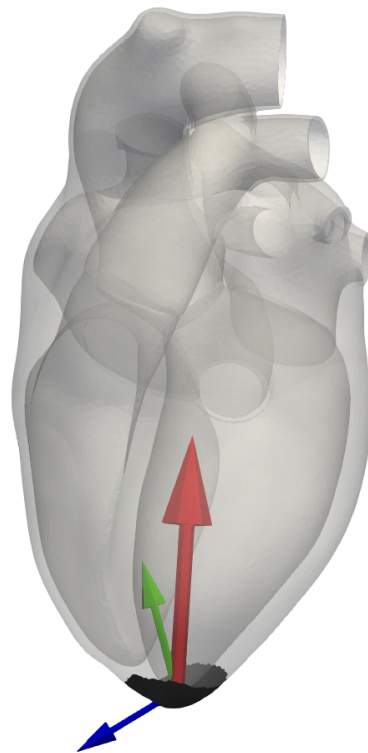
3.6 Discussion

Based on the physiology of the pericardium, the objective in this chapter is to analyze the effects of the pericardial boundary condition proposed in Section 3.2, by comparing the simulation cases *pericardium* and *apex*. First, a parametric study was performed to explore the influence of pericardial stiffness. Each simulation case was personalized and evaluated for the fiber orientations $\pm 50^\circ$, $\pm 60^\circ$, and $\pm 70^\circ$. The scalar left ventricular pressure and volume were then compared. The displacements at end-systole were qualitatively compared to multi-view cine MRI. Additionally, the differences of both simulation cases are compared to MRI by atrioventricular plane displacement (AVPD), passive atrial filling, and spatial approximation error at the left and right ventricular endocardium.

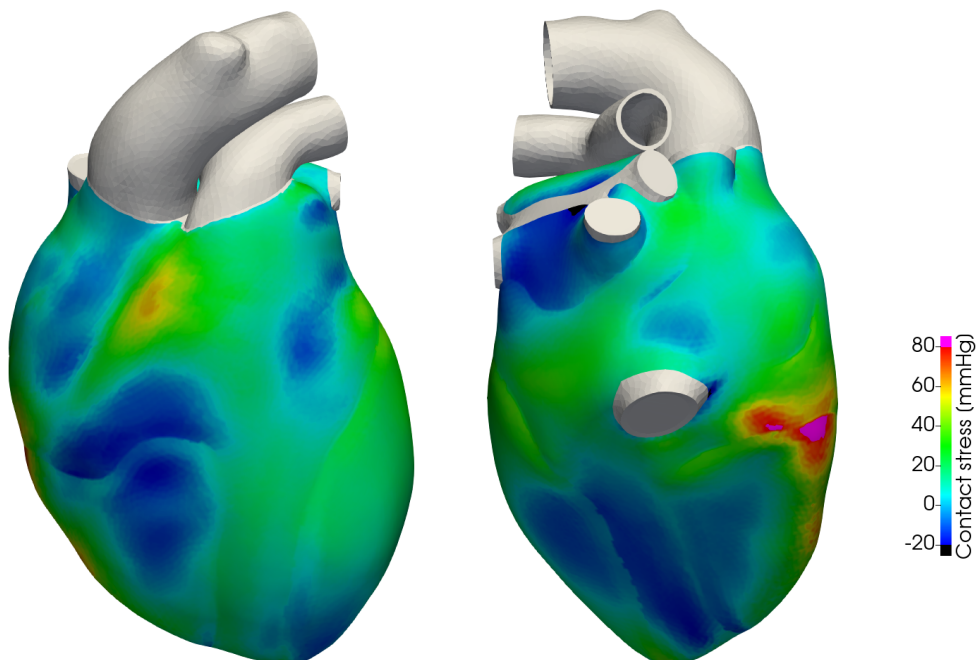
Pericardial stiffness

The parametric study for pericardial stiffness in case *pericardium* in Section 3.5.3 revealed that the ventricles are well approximated by the lowest tested stiffness values, e.g. $k_p = 0.1$ kPa/mm. Here, the error at left and right ventricular endocardium was minimized and much lower than in case *apex*.

In contrast, right AVPD and right atrial passive filling matched well with measurements from MRI for high stiffness values, e.g. $k_p = 3.0$ kPa/mm. Choosing this value globally for pericardial stiffness lead however to some undesirable consequences, namely unphysiologically high myocardial contractility and pericardial stress as well as bad approximation of the interventricular septum.



(a) Case *apex* mean apical stress vectors \bar{t}_{apex} (scaled by magnitude) for $\pm 50^\circ$ (red), $\pm 60^\circ$ (green), and $\pm 70^\circ$ (blue) fiber orientations at $t = 0.45$.



(b) Case *pericardium* pericardial contact stress t_{epi} on epicardial surface with $\pm 60^\circ$ fibers at end-systole $t = 0.51$.

Figure 3.20: Visualization of boundary stresses.

In future studies, it might thus be reasonable to select spatially varying pericardial parameters. This hypothesis is supported by the fact that the pericardial tissue is in contact with various organs of different material properties as outlined in Section 3.1.2. A starting point could be the estimation of regional pericardial parameters based on the surface definitions in Figure 3.2 with the objective to match MRI measurements in Section 3.5.3.

In case of a biventricular geometry, no atria are present. Thus AVPD is not controlled by the interaction of atria and pericardium. Furthermore, atrial filling is not taken into account. It is thus expected that a global value of $k_p = 0.1$ kPa/mm for pericardial stiffness yields good results for a biventricular geometry with $\pm 60^\circ$ fibers. This value was also used in [83], although it was not really analyzed there, e.g. with respect to MRI.

Pumping mechanism

Cardiac contractility was calibrated in all simulations in Section 3.5.3 to yield the same end-systolic volume. It was shown that in case *pericardium*, higher contractilities are required than in case *apex*. Therefore, for a given contractility, a heart constrained with the pericardial boundary condition yields less output. This result is in agreement with the experimental observation that cardiac output is greatly increased after the removal of the pericardium [79]. The result further agrees with the numerical experiments performed in [56]. For identical active stress, left ventricular ejection fraction decreased from 71 % to 63 % when including the pericardium.

The main pumping mechanism of the heart is shortening in long axis direction, which is quantified by AVPD [6, 7]. In [124], the pumping function of the heart was compared to a piston unit with the AVP as a piston. This mechanism could be observed in Section 3.5.5.3 for case *pericardium*, where left and right AVPD is higher than in case *apex* but still lower than in MRI.

The upper part of the left atrium is fixed by pulmonary veins. Ventricular contraction forces the mitral ring towards the apex and promotes the filling of the left atrium from the pulmonary veins [57]. In Section 3.5.5.4, atrial filling was compared during ventricular systole with and without pericardium. It was observed that the simulations of case *pericardium* which promoted higher AVPD in Section 3.5.5.3 contribute more to atrial filling during ventricular systole. Case *pericardium* predicts maximal atrial volume at ventricular end-systole as segmented from isotropic 3D MRI better than case *apex*. The simulated values are, however, still lower than in MRI for the chosen pericardial parameters.

It was shown that the pumping mechanism of the heart is very different for cases *apex* and *pericardium*, although their pressure and volume curves were similar in Section 3.5.5.1. A comparison of four-chamber and short axis slices of the left and right ventricle from simulation results to cine MRI in Section 3.5.5.2 revealed an unphysiological radial pumping motion without pericardial boundary conditions in case *apex*. In [47], it was revealed that the outer diameter of the left ventricle shortens only about 2 mm during systole. Furthermore, the total volume enclosed by the pericardium changes only by about 5-8 % during the cardiac cycle [7, 24]. It was found that for the $\pm 60^\circ$ fiber orientation the total change in pericardial volume is 24 % and 21 % for cases *pericardium* and *apex*, respectively. This mismatch is mainly due to the unphysiological change in atrial volume during ventricular contraction.

As demonstrated in the parametric study in Section 3.5.3, AVPD and atrial filling could be increased to the values measured in MRI by increasing the global pericardial stiffness. However, this was shown to lead to a worse approximation of the interventricular septum. This, again,

motivates the use of a regionally distributed pericardial stiffness. Another reason for underestimating AVPD and atrial filling might be a too stiff atrial material model, which is in this case identical to the ventricular one.

Fiber orientation

In this work, three fiber orientations were compared within the myocardium, namely $\pm 50^\circ$, $\pm 60^\circ$, and $\pm 70^\circ$. The influence of fiber direction for both boundary condition cases *apex* and *pericardium* was studied. It was shown that fiber orientation has a strong influence on the displacements. In Section 3.5.5.3 $\pm 70^\circ$ fiber orientations exhibited larger AVPD for both boundary condition cases. This can be attributed to the fact that the fiber orientation is more vertical, i.e., more aligned with the long axis, than $\pm 60^\circ$ and $\pm 50^\circ$ fiber orientations. Since myofiber contraction is prescribed in fiber direction, more vertical fiber orientations inherently apply a greater force pushing apex and AVP together, thus yielding higher AVPD. Since the AVP is attached to the atria, AVPD is also linked to atrial filling. In Section 3.5.5.4 it was shown that the more vertical $\pm 70^\circ$ fiber orientation also yielded the highest atrial filling during ventricular systole. Comparing results to short axis cine MRI slices, it was shown that a more horizontal $\pm 50^\circ$ fiber orientation leads to a more radial contraction of the heart. The maximum pericardial stress at end-systole was highest for $\pm 50^\circ$ fibers. This can be explained by the observation in Figure 3.15h where $\pm 50^\circ$ fibers (red) exhibited the most radial inward movement during systole. Since the myocardial-pericardial interface can only transmit forces in normal direction, a more radial contraction exerts a higher pericardial tensile stress. The overall spatial approximation error was also shown to be dependent on fiber direction. However, the dependence was more pronounced in case *apex* than in case *pericardium*.

Pericardial contact stress

In [165], end-diastolic pericardial contact pressure was measured with a flat balloon catheter at the left ventricular anterolateral epicardial surface with around 15 mmHg. In vivo experiments on humans in [177] showed pericardial pressures on the left lateral surface of the heart between 0 and 15 mmHg. The prestressing procedure in the model does not only include the myocardium but also the pericardial boundary condition in case *pericardium*. Here, a contact pressure of 20 mmHg was measured at diastasis on the left ventricular epicardial surface, agreeing well with experimental observations.

The stresses exerted by the boundary conditions on the epicardial surface of the heart were found to be more than one order of magnitude higher in case *apex* than in case *pericardium*. The exact stress values in case *apex* depend on the choice of apical spring stiffness, which was not calibrated in this study. It is nevertheless evident, that unphysiologically high stresses are concentrated in a very small area of the heart. In case *pericardium*, all boundary stresses are evenly distributed on the epicardial surface.

The similar maximum values of mean pericardial contact stress for all fiber directions in case *pericardium* suggest that pericardial constraint is displacement-controlled. Pericardial constraint is determined by the deviation of the heart throughout the cardiac cycle from its end-diastolic state. However, as outlined in Section 3.1.2, to the best of the authors' knowledge there are no measurements of pericardial contact pressure during the cardiac cycle to validate the stresses

experienced in the computational study. Pericardial contact stress is thus an output of the computational model which is not yet available in clinical practice. Given that the model was solely calibrated to kinematic data, the pericardial contact stresses predicted by the model should be considered as qualitative results.

Numerical performance

All simulations were run on two nodes of a Linux cluster. One node features 64 GB of RAM and two Intel Xeon E5-2680 "Haswell" processors, each equipped with 12 cores operating at a frequency of 2.5 GHz. The computation times of cases *apex* and *pericardium* were almost identical, which was about 18 hours for each of the simulations performed in this work, including prestressing. The pericardial boundary condition requires little effort to evaluate, since the pericardial boundary condition only requires the displacement field, which is computed anyway, and the reference surface normals, which are computed once at the initialization of the simulation. Some differences in numerical performance arise since the calculated displacement fields of both cases are different. Taking the $\pm 60^\circ$ fiber distribution, case *apex* had an average of 7.8 Newton iterations per time step and 28 linear solver iterations per Newton iteration. For case *pericardium*, these values were 8.3 and 25, respectively.

Limitations and future perspectives

As mentioned earlier, in this work, the propagation of the electrical signal sent from the sinus node was not accounted for. Rather, all myocardial tissues in the simulations were activated simultaneously. Recently, the ability to couple the structural model to an electrophysiological model was demonstrated in [89], which can be included in further studies. However, since the data came from a healthy volunteer, it is not expected to yield relevant variations.

Ex-vivo experiments on myocardial tissue in [45, 166, 192] showed anisotropic tissue characteristics, depending on myocardial fiber and sheet orientation. In the model, the anisotropic material model proposed in [88] was used for myocardial tissue. Due to the lack of sufficient experimental data, identical material properties were used for left and right myocardium, as well as the atria. However, no studies have been carried out how material parameters obtained from experiments on ex vivo tissue correlate to in vivo material behavior. Furthermore, it should be noted that vastly different material parameters have been estimated in [88] and [75] when being fitted to measurements from either biaxial tensile tests or shear tests.

The structural model was coupled to a lumped-parameter Windkessel model of hemodynamics of the systemic and pulmonary circulation with prescribed atrial pressures as in Figure 2.9b. The interaction between atria and ventricles should be investigated in further studies using a volume-preserving closed-loop model, including both pulmonary and systemic circulation. Furthermore, none of the cardiac simulations behave perfectly periodic, i.e., the values at the end of the cardiac cycle are not equal to the initial conditions. In future studies, achieving a periodic state should be incorporated into parameter estimation.

In this work the local helix fiber directions were interpolated at the integration points from three different prescribed constant-per-surface fiber orientations. Results showed that fiber orientation has a large influence on AVPD. However, there is no knowledge of patient-specific fiber orientation and equal distributions in left and right ventricle is assumed. Patient-specific cardiac

fiber orientations can be estimated from diffusion tensor MRI [138] (DTMRI). However, while applicable to in vivo DTMRI (as shown in [138]), to the best of the author's knowledge, fiber estimation has not been tested and validated with in vivo DTMRI yet. Further quantitative studies of cardiac dynamics require a fine resolution of patient-specific fibers.

Furthermore, constant stiffness and viscosity parameters of the pericardial boundary condition over the epicardial surface were assumed. Given reliable material parameters for the myocardium, constant pericardial stiffness and viscosity could be estimated from measured AVPD. The choice of constant parameters might however be oversimplified, as the pericardium is in contact with various tissues of different mechanical behaviors, as illustrated in Figure 3.2. For example, the movement of the apex in anterior direction in case *pericardium* as observed in Figure 3.15g suggests a higher pericardial stiffness to model the influence of the sternum and the diaphragm. This will however introduce more parameters to the model, which will need to be calibrated to measurements from e.g. cine or 3D tagged MRI. For this study the number of parameters was kept small in order to make the general effect of the pericardial boundary condition even by using a simplified modeling approach evident.

From a machine learning perspective, the limited available data from cine MRI was split into a training set and a test set. The training set data is used during model personalization. The rest of the data can then be used in the test set to check how well the model actually predicts data that was not used during personalization. In the present case, left ventricular volume and ventricular epicardial contours were used as training set to tune timing, (de-) activation rates, and contractility for atria and ventricles and global material viscosity and pericardial stiffness. AVPD, atrial volume, and ventricular endocardial contours, each left and right, were then used as test set to quantify the simulations' approximation error. Many more parameters of the cardiac model could be personalized for this patient-specific study. However, using the metrics in the test set for model calibration would disqualify using them to test model accuracy and limit the abilities to test the model.

Simulation results were solely validated with cine MRI data. Cine MRI can be interpreted as an Eulerian description of cardiac movement, as the imaging planes stay fixed in space throughout the cardiac cycle. This observation, however, cannot detect any rotational movement with respect to the long axis, as the left ventricle is almost rotationally symmetric. To properly validate any rotational movement of the myocardium, a comparison to data from 3D tagged MRI is necessary, which can be interpreted as a Lagrangian observation of cardiac motion. Furthermore, pressure measurements from within ventricles and atria are required. Pressure values at end-diastole are the initial values for the stress state of the myocardium, which cannot be assessed from imaging alone. Pressure curves over the cardiac cycle would yield a ground truth to validate the outputs of the Windkessel model. Figure 3.17 demonstrates that the model, while using the pericardial constraint, does accurately predict the atrial volume at ventricular end-systole. However, no data was obtainable at atrial end-systole. In future studies, if detailed cine data of atria are available (e.g. cine stack in transverse orientation with respect to the body, and using thin slices of 5mm), a more detailed analysis of atrial contraction will be considered.

3.7 Conclusion

In this chapter, an overview of the anatomy and mechanical function of the pericardium was given, and it was motivated to model its influence on the myocardium as springs and dashpots acting parallel on the epicardial surface. After a review of pericardial boundary conditions currently used in mechanical simulations of the heart, it was proposed to compare two simulation cases, one with and one without pericardial boundary conditions. Following calibration to stroke volume as measured from short axis cine MRI, several physiological key outputs of the model were compared and validated using multi-view cine MRI. Although exhibiting similar volume and pressure curves, the displacement results of both simulation cases were radically different. The simulations with pericardial boundary conditions matched MRI measurements much closer than without, especially with respect to atrioventricular plane displacement and atrial filling during ventricular systole, both quantities which were not included in the calibration of the model. By establishing an overall spatial approximation error at the left and right endocardium, it was shown that the introduction of only two global parameters for the pericardial boundary condition already yields a big gain in model accuracy. The ultimate goal is to obtain more comprehensive data sets, adding 3D tagged MRI and pressure measurements, to further validate the model of pericardial-myocardial interaction. Measurements of pericardial contact stress at different locations on the epicardium throughout the cardiac cycle would help to test the qualitative predictions of pericardial contact stresses by the present model and will probably lead to further model improvements.

4 Model order reduction

The interaction between myocardium and pericardium was studied in Chapter 3 using a patient-specific four-chamber geometry. As this is a high-fidelity model, it results in high computational demands. This chapter thus focuses on model order reduction techniques for monolithically coupled cardiac structure-Windkessel models. The remainder of this chapter is structured as follows. A reduced formulation is derived in Section 4.1 for the monolithically coupled system introduced in Section 2.6. Furthermore, several subspace interpolation methods are reviewed in Section 4.2. In numerical experiments in Section 4.3, the accuracy and speedup of the reduced order model (ROM) are demonstrated, and its response to parametric variations is shown. This chapter is closed with a conclusion and future perspectives in section 4.4.

Parts of this chapter were submitted for publication in [147].

4.1 Nonlinear parametric model order reduction by projection

The 3D-0D cardiovascular model described in Section 2.6 represents a large-scale, nonlinear, parametrized, and monolithically coupled model. It features multiple sources of nonlinear system behavior and depends on several model parameters. Firstly, the structural model contains geometric nonlinearities due to the use of the Green-Lagrange strain tensor $\mathbf{E}(\mathbf{u})$. Secondly, the utilized material laws for myocardial tissue induce material nonlinearity. The third and last source of nonlinearity is given by the nonlinear coupling between the structural and the hemodynamical model due to the Neumann Windkessel boundary condition, acting in direction of the current normal vector of the endocardium. Furthermore, the model depends on many parameters $\boldsymbol{\mu} = [\mu_1, \dots, \mu_{n_p}]^T \in \Omega \subset \mathbb{R}^{n_p}$, classified in different categories. For instance, there exist parameters describing the constitutive behavior of the used materials (stiffness, viscosity, and incompressibility parameters), the additive active stress component \mathbf{S}_{act} (e.g. the contractility σ_0 , (un)binding rates α_{max} and α_{min} , timings t_{sys} and t_{dias}), the hemodynamics (e.g. resistances R , compliances C , inertance L_p), as well as the boundary conditions for the outside of the great vessels and the epicardium (spring stiffnesses k_v, k_e and dashpot viscosities c_v, c_e). Thus, the discrete nonlinear parametrized full order model (FOM) with residual \mathbf{R} reads

$$\mathbf{R}(\mathbf{d}, \mathbf{p}, \boldsymbol{\mu}) = \begin{bmatrix} \mathbf{R}^S(\mathbf{d}, \mathbf{p}, \boldsymbol{\mu}) \\ \mathbf{R}^W(\mathbf{d}, \mathbf{p}, \boldsymbol{\mu}) \end{bmatrix} \stackrel{!}{=} \mathbf{0}, \quad (4.1)$$

with structural residual \mathbf{R}^S , Windkessel residual \mathbf{R}^W and corresponding unknowns \mathbf{d} and \mathbf{p} , respectively. The use of a 0D lumped-parameter Windkessel model, instead of e.g. a 3D fluid dynamics model of the heart chambers and arteries, already simplifies the computational complex-

ity of the coupled system. However, the numerical analysis of the present model still demands a high computational effort due to the large number of structural degrees of freedom (DOFs). While this is no problem for a few standard forward simulations, it is extremely challenging - and might even prohibit - fast model calibration, inverse analysis, and clinical applications. Therefore, the aim is to employ projection-based model order reduction to obtain a cardiovascular reduced order model (ROM) that accurately approximates the original model with substantially less DOFs and, consequently, less numerical effort. To this end, in Section 4.1.2 a classical projection-based model order reduction framework is applied to the structural component of the cardiovascular problem. A suitable strategy to compute the required projection matrix \mathbf{V} for a fixed parameter set is explained in Section 4.1.3. In order to compute a parametric reduced order model (pROM) for any new parameter set, different subspace interpolation techniques are presented in Section 4.2. Finally, some implementation details are given in Section 4.3.2.

4.1.1 Subspace projection

A matrix $\mathbf{P} \in \mathbb{R}^{n \times n}$ is a projector if the repeated application to an n -dimensional vector $\mathbf{x} \in \mathbb{R}^n$ always yields the same projection $\mathbf{x}_P \in \mathbb{R}^n$:

$$\mathbf{x}_P = \mathbf{P}\mathbf{x} = \mathbf{P}(\mathbf{P}\mathbf{x}) = \mathbf{P}^2\mathbf{x}. \quad (4.2)$$

The property $\mathbf{P} = \mathbf{P}^2$ thus must hold for a matrix to be a projector. In the following, the projection matrix \mathbf{P} will be derived for projecting \mathbf{x} onto the q -dimensional subspace $\mathcal{V} \subset \mathbb{R}^n$ in the direction of the q -dimensional subspace $\mathcal{W} \subset \mathbb{R}^n$. The q orthogonal basis vectors $\mathbf{v}_i \in \mathbb{R}^n$ are contained in the columns of the matrix $\mathbf{V} = [\mathbf{v}_1, \dots, \mathbf{v}_q] \in \mathbb{R}^{n \times q}$, spanning the subspace \mathcal{V} :

$$\mathcal{V} = \text{span}(\mathbf{V}) = \left\{ \sum_{i=1}^q \lambda_i \mathbf{v}_i \mid \mathbf{v}_i \in \mathbf{V}, \lambda_i \in \mathbb{R} \right\}. \quad (4.3)$$

The projection \mathbf{x}_P of a vector \mathbf{x} onto \mathcal{V} can be expressed as the matrix-vector multiplication

$$\mathbf{x}_P = \mathbf{V}\mathbf{c}, \quad (4.4)$$

where $\mathbf{c} \in \mathbb{R}^q$ is a yet to be determined coefficient vector containing the amplitudes of the basis vectors \mathbf{v}_i . The component \mathbf{x}_\perp of \mathbf{x} is orthogonal to the projecting subspace \mathcal{V} spanned by the q orthogonal basis vectors $\mathbf{w}_i \in \mathbb{R}^n$, contained in the matrix $\mathbf{W} = [\mathbf{w}_1, \dots, \mathbf{w}_q] \in \mathbb{R}^{n \times q}$,

$$\mathbf{x}_\perp = \mathbf{x} - \mathbf{x}_P = \mathbf{x} - \mathbf{V}\mathbf{c}. \quad (4.5)$$

The orthogonality of \mathbf{x}_\perp and \mathbf{W} can be expressed by requiring

$$\mathbf{W}^\top \mathbf{x}_\perp = \mathbf{0}. \quad (4.6)$$

The component \mathbf{x}_\perp is thus perpendicular to all basis vectors \mathbf{w}_i of the subspace \mathcal{W} . Inserting the expression for the orthogonal component in (4.5) into the orthogonality condition (4.6) yields

$$\mathbf{W}^\top (\mathbf{x} - \mathbf{V}\mathbf{c}) = \mathbf{W}^\top \mathbf{x} - \mathbf{W}^\top \mathbf{V}\mathbf{c} = \mathbf{0}, \quad (4.7)$$

which can be solved for the coefficient vector

$$\mathbf{c} = (\mathbf{W}^T \mathbf{V})^{-1} \mathbf{W}^T \mathbf{x}, \quad (4.8)$$

if the inverse $\mathbf{W}^T \mathbf{V} \in \mathbb{R}^{q \times q}$ of the square matrix exists. Inserting the coefficient vector (4.8) into (4.4) yields

$$\mathbf{x}_P = \mathbf{V} (\mathbf{W}^T \mathbf{V})^{-1} \mathbf{W}^T \mathbf{x} = \mathbf{P} \mathbf{x} \quad (4.9)$$

and thus the definition of the projector

$$\mathbf{P} = \mathbf{V} (\mathbf{W}^T \mathbf{V})^{-1} \mathbf{W}^T \in \mathbb{R}^{n \times n}. \quad (4.10)$$

The special case of $\mathcal{V} = \mathcal{W}$ results in orthogonal projection, whereas the general case $\mathcal{V} \neq \mathcal{W}$ yields an oblique projection.

The spatially semi-discrete version of the coupled structural-Windkessel model proposed in Section 2.6 is

$$\mathbf{R}_{\text{semi}}^S(\mathbf{d}, \dot{\mathbf{d}}, \ddot{\mathbf{d}}, \mathbf{p}, \boldsymbol{\mu}) = \mathbf{M} \ddot{\mathbf{d}} + \mathbf{F}(\mathbf{d}, \dot{\mathbf{d}}, \mathbf{p}, \boldsymbol{\mu}) = \mathbf{0}. \quad (4.11)$$

Besides the model state characterized by \mathbf{p} , \mathbf{d} , and time derivatives thereof, the FOM depends on the model parameter set $\boldsymbol{\mu}$. The dimension of the discrete nodal displacements $\mathbf{d} \in \mathbb{R}^n$ is commonly high for cardiac problems and scales computation time and memory consumption. However, during the solution of a cardiac cycle, not all possible n configurations within the space \mathbb{R}^n are taken. Usually, the configurations can be contained in the much smaller q -dimensional subspace \mathcal{V} , with $q \ll n$. The displacements are therefore approximated by displacements \mathbf{d}_r ,

$$\mathbf{d} \approx \mathbf{V} \mathbf{d}_r, \quad (4.12)$$

where \mathbf{d}_r contains the amplitudes of the basis vectors v_i in \mathbf{V} . The approximation (4.12) can be inserted in the structural residual $\mathbf{R}_{\text{semi}}^S$

$$\mathbf{R}_{\text{semi}}^S(\mathbf{V} \mathbf{d}_r, \mathbf{V} \dot{\mathbf{d}}_r, \mathbf{V} \ddot{\mathbf{d}}_r, \mathbf{p}, \boldsymbol{\mu}) = \mathbf{e}, \quad (4.13)$$

introducing the error \mathbf{e} . In general, not all n equations in (4.13) can be satisfied by the q unknowns in \mathbf{d}_r . The error \mathbf{e} is zero only in two special cases. Firstly, for $q = n$ the projection turns into a basis transformation and the matrix \mathbf{V} has rank n . Secondly, when all admissible displacements \mathbf{d} actually span the subspace \mathcal{V} , e.g. prescribed through boundary conditions, repeated projection onto \mathcal{V} does not change the system of equations (4.11) due to property (4.2). Both cases are however not relevant for cardiac or other real-world problems.

In order to obtain a square system of equations, the equation for the reduced residual (4.13) is projected onto the subspace \mathcal{V} using the projector \mathbf{P} as derived in (4.9):

$$\mathbf{V} (\mathbf{W}^T \mathbf{V})^{-1} \mathbf{W}^T \mathbf{R}_{\text{semi}}^S(\mathbf{V} \mathbf{d}_r, \mathbf{V} \dot{\mathbf{d}}_r, \mathbf{V} \ddot{\mathbf{d}}_r, \mathbf{p}, \boldsymbol{\mu}) = \mathbf{V} (\mathbf{W}^T \mathbf{V})^{-1} \mathbf{W}^T \mathbf{e}_P. \quad (4.14)$$

The approximation error \mathbf{e}_P is set to be orthogonal to the projection space \mathcal{W} and thus

$$\mathbf{W}^T \mathbf{e}_P = \mathbf{0}. \quad (4.15)$$

Given that \mathbf{V} contains orthogonal basis vectors the matrix is of full rank and can thus be dropped from both sides of equation (4.14). Additionally, multiplying by $\mathbf{W}^T \mathbf{V}$ yields

$$\mathbf{W}^T \mathbf{R}_{\text{semi}}^S(\mathbf{V} \mathbf{d}_r, \mathbf{V} \dot{\mathbf{d}}_r, \mathbf{V} \ddot{\mathbf{d}}_r, \mathbf{p}, \boldsymbol{\mu}) = \mathbf{0}, \quad (4.16)$$

which is the Galerkin projection of the FOM.

Remark The general case $\mathbf{W} \neq \mathbf{V}$ is an oblique Petrov-Galerkin projection. Setting both projection matrices equal, i.e. $\mathbf{W} = \mathbf{V}$, yields an orthogonal Bubnov-Galerkin projection. Despite the naming convention, there is another analogy to the Galerkin method applied to Finite Elements in Section 2.2.2. For the Finite Element Method, the approximation error e_d in (2.47) made by restricting the infinite solution and weighting function spaces to finite-dimensional subspaces is orthogonal to the discrete weighting basis function space \mathcal{T}_h . For projection-based model order reduction, the approximation error e_P made by projecting the high-dimensional solution to a lower-dimensional space is orthogonal to the projecting space \mathcal{W} .

4.1.2 Cardiovascular reduced order model

Inserting the Bubnov-Galerkin projection into the coupled cardiac problem yields the space and time discrete coupled reduced residual

$$\mathbf{R}_r := \begin{bmatrix} \mathbf{W}^T \mathbf{R}^S(\mathbf{V}\mathbf{d}_r, \mathbf{p}, \mu) \\ \mathbf{R}^W(\mathbf{V}\mathbf{d}_r, \mathbf{p}, \mu) \end{bmatrix}_{n+1}, \quad (4.17)$$

at time step $n + 1$. Linearizing the residual yields

$$\begin{bmatrix} \mathbf{K}_r^S & \mathbf{K}_r^{SW} \\ \mathbf{K}_r^{WS} & \mathbf{K}_r^W \end{bmatrix}_{n+1}^i \cdot \begin{bmatrix} \Delta \mathbf{d}_r \\ \Delta \mathbf{p} \end{bmatrix}_{n+1}^{i+1} = - \begin{bmatrix} \mathbf{R}_r^S \\ \mathbf{R}_r^W \end{bmatrix}_{n+1}^i \quad (4.18)$$

which is solved for the increments $\Delta \mathbf{d}_r$ and $\Delta \mathbf{p}$ of reduced displacements and Windkessel unknowns, respectively, using the linearizations

$$\mathbf{K}_r^S = \frac{\partial \mathbf{R}_r^S}{\partial \mathbf{d}_r} = \frac{\partial}{\partial \mathbf{d}_r} [\mathbf{W}^T \mathbf{R}^S(\mathbf{V}\mathbf{d}_r, \mathbf{p}, \mu)] = \mathbf{W}^T \frac{\partial \mathbf{R}^S(\mathbf{d}, \mathbf{p}, \mu)}{\partial \mathbf{d}} \Big|_{\mathbf{d}=\mathbf{V}\mathbf{d}_r} \cdot \frac{\partial \mathbf{V}\mathbf{d}_r}{\partial \mathbf{d}_r} = \mathbf{W}^T \mathbf{K}^S \mathbf{V}, \quad (4.19)$$

$$\mathbf{K}_r^{SW} = \frac{\partial \mathbf{R}_r^S}{\partial \mathbf{p}} = \frac{\partial}{\partial \mathbf{p}} [\mathbf{W}^T \mathbf{R}^S(\mathbf{V}\mathbf{d}_r, \mathbf{p}, \mu)] = \mathbf{W}^T \frac{\partial \mathbf{R}^S(\mathbf{d}, \mathbf{p}, \mu)}{\partial \mathbf{p}} \Big|_{\mathbf{d}=\mathbf{V}\mathbf{d}_r} = \mathbf{W}^T \mathbf{K}^{SW}, \quad (4.20)$$

$$\mathbf{K}_r^{WS} = \frac{\partial \mathbf{R}_r^W}{\partial \mathbf{d}_r} = \frac{\partial}{\partial \mathbf{d}_r} [\mathbf{R}^W(\mathbf{V}\mathbf{d}_r, \mathbf{p}, \mu)] = \frac{\partial \mathbf{R}^W(\mathbf{d}, \mathbf{p}, \mu)}{\partial \mathbf{d}} \Big|_{\mathbf{d}=\mathbf{V}\mathbf{d}_r} \cdot \frac{\partial \mathbf{V}\mathbf{d}_r}{\partial \mathbf{d}_r} = \mathbf{K}^{WS} \mathbf{V}, \quad (4.21)$$

$$\mathbf{K}_r^W = \frac{\partial \mathbf{R}_r^W}{\partial \mathbf{p}} = \frac{\partial}{\partial \mathbf{p}} [\mathbf{R}^W(\mathbf{V}\mathbf{d}_r, \mathbf{p}, \mu)] = \frac{\partial \mathbf{R}^W(\mathbf{d}, \mathbf{p}, \mu)}{\partial \mathbf{p}} \Big|_{\mathbf{d}=\mathbf{V}\mathbf{d}_r} = \mathbf{K}^W. \quad (4.22)$$

Since only the structural dimension of the problem is reduced, the $(2, 2)$ -block remains unchanged, i.e. $\mathbf{K}_r^W = \mathbf{K}^W$. Using the Bubnov-Galerkin projection with $\mathbf{W} = \mathbf{V}$ yields the linearized coupled system

$$\begin{bmatrix} \mathbf{V}^T \mathbf{K}^S \mathbf{V} & \mathbf{V}^T \mathbf{K}^{SW} \\ \mathbf{K}^{WS} \mathbf{V} & \mathbf{K}^W \end{bmatrix}_{n+1}^i \cdot \begin{bmatrix} \Delta \mathbf{d}_r \\ \Delta \mathbf{p} \end{bmatrix}_{n+1}^{i+1} = - \begin{bmatrix} \mathbf{R}_r^S \\ \mathbf{R}_r^W \end{bmatrix}_{n+1}^i, \quad (4.23)$$

making use of the full-dimensional linearizations. The original (2.75) and reduced (4.23) block-Jacobians are visualized in Figure 4.1. Note that in each Newton-Raphson iteration i , the reduced displacements \mathbf{d}_r must be extrapolated to the full dimension using (4.12) to evaluate the residuals \mathbf{R}_r^S and \mathbf{R}^W as well as their linearizations. It is only after their full evaluation and assembly that their dimensions are reduced by projection. The update step thus becomes

$$\begin{bmatrix} \mathbf{d} \\ \mathbf{p} \end{bmatrix}_{n+1}^{i+1} = \begin{bmatrix} \mathbf{d} \\ \mathbf{p} \end{bmatrix}_{n+1}^i + \begin{bmatrix} \mathbf{V}\Delta\mathbf{d}_r \\ \Delta\mathbf{p} \end{bmatrix}_{n+1}^{i+1}. \quad (4.24)$$

Since the solution of the reduced system is within the projection space \mathcal{V} , convergence can only be achieved in that space. The convergence check is thus carried out with the reduced residual and reduced displacement increment

$$\|\mathbf{R}_r^S\|_\infty < \text{tol}_{\text{res},r}^S, \quad \|\Delta\mathbf{d}_r\|_\infty < \text{tol}_{\text{inc},r}^S. \quad (4.25)$$

The process of reducing the FOM within the computational framework is outlined in Algorithm 1.

Algorithm 1 Projection-based model order reduction.

- 1: generate projection matrix \mathbf{V} offline with methods from Sections 4.1.3 (constant) or 4.2 (parametric)
 - 2: **for** time step $j = 0, \dots, n_s$ **do**
 - 3: Newton iteration $i = 0$
 - 4: **while** convergence criterion from (4.25) not fulfilled **do**
 - 5: evaluate and assemble full Jacobian and residual (4.18)
 - 6: reduce structural dimensions in Jacobian and residual (4.23)
 - 7: solve reduced linear system (4.23)
 - 8: approximate full displacements (4.12)
 - 9: update solution (4.24)
 - 10: $i \leftarrow i + 1$
 - 11: **end while**
 - 12: **return** solution \mathbf{d}_j and \mathbf{p}_j
 - 13: **end for**
-

The convergence criteria for 0D Windkessel model remain unchanged. Likewise to the coupled full order model (2.75) in Section 2.6, the coupled ROM in (4.23) is valid for any full order structural and Windkessel residual \mathbf{R}^S and \mathbf{R}^W , respectively.

4.1.3 Subspace computation via POD

In this work, the method of Proper Orthogonal Decomposition (POD) is used to compute the reduced basis \mathbf{V} required for the projection-based reduction of the full problem. POD [34, 109] is a straightforward and well-known nonlinear model reduction approach, which relies on so-called *snapshots*, i.e. discrete-time observations of the solution of the FOM for a fixed parameter

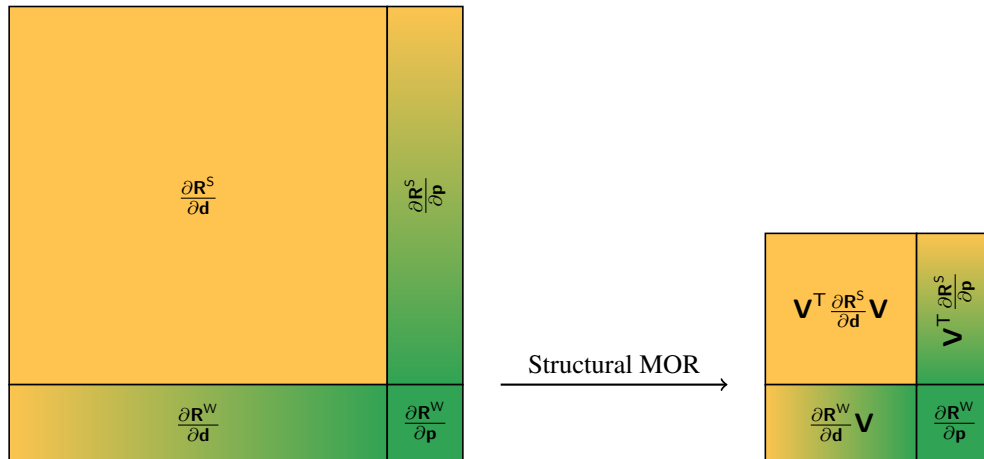


Figure 4.1: Visualization of the Jacobian for projection-based model order reduction of the block matrix system's structural dimension in (2.75) to (4.23). The diagonal structural and Windkessel blocks are colored yellow and green, respectively. Off-diagonal coupling blocks are shaded. Note that the dimension of the diagonal Windkessel block remains unchanged.

set $\boldsymbol{\mu}$, to construct the basis \mathbf{V} . Given n_s snapshots \mathbf{d}_i gained from a numerical simulation of the FOM sample point, the snapshot matrix then states

$$\mathbf{D} = [\mathbf{d}_1, \dots, \mathbf{d}_{n_s}] \in \mathbb{R}^{n \times n_s}. \quad (4.26)$$

Typically, the number of snapshots n_s corresponds to the number of time steps in the FOM simulation. The goal of POD is to construct a basis for an optimal approximation of the *solution manifold* spanned by the snapshot matrix. In other words, the aim is to generate a basis that optimally approximates the information gathered in the snapshots. Therefore, a singular value decomposition (SVD) of the snapshot matrix is performed

$$\mathbf{D} = \mathbf{U} \boldsymbol{\Sigma} \mathbf{T}^T \quad (4.27)$$

with the orthogonal matrices $\mathbf{U} \in \mathbb{R}^{n \times n}$ and $\mathbf{T} \in \mathbb{R}^{n_s \times n_s}$ containing the left and right singular vectors, respectively, stored column-wise. The diagonal matrix

$$\boldsymbol{\Sigma} = \text{diag}(\sigma_1, \dots, \sigma_{n_s}) \in \mathbb{R}^{n \times n_s}, \quad \text{where } \sigma_1 \geq \dots \geq \sigma_{n_s} \geq 0, \quad (4.28)$$

features all n_s singular values σ_i sorted in descending order on its main diagonal. Now, the first q singular vectors \mathbf{u}_i are selected from the columns of the left singular matrix \mathbf{U} corresponding to the q largest singular values σ_i in $\boldsymbol{\Sigma}$ to obtain the basis vectors

$$\mathbf{v}_i = \mathbf{u}_i, \quad \forall i \in \{1, \dots, q\} \quad (4.29)$$

of the projection matrix \mathbf{V} . The singular values σ_i are frequently used to define the relative information content (RIC)

$$\text{RIC}(q) = \frac{\sum_{i=1}^q \sigma_i^2}{\sum_{i=1}^{n_s} \sigma_i^2} \in [0, 1]. \quad (4.30)$$

This measure allows to select an appropriate basis dimension q such that $\text{RIC}(q) \geq 1 - \varepsilon_{\text{POD}}$ for a given small tolerance ε_{POD} . [20] The approximation error made by selecting $q < n_s$ basis vectors can be quantified by the sum of the squared truncated singular values

$$e(q) = \sum_{i=q+1}^{n_s} \sigma_i^2. \quad (4.31)$$

Note that this technique provides an optimal basis for the approximation of the snapshot matrix in a least-squares sense [102, 110, 121]. Thus, the efficiency of POD and the basis quality crucially depends on the selection of snapshots, which is required to represent the model's dynamical behavior sufficiently. Furthermore, POD requires the expensive simulation of the full forward model. In general, this requires the solution of many parameter sets to collect representative snapshots. Nevertheless, this data-driven approach is very well applicable for the reduction of any nonlinear system.

4.2 Interpolation of subspaces

The cardiac model described in Section 2.6 relies on many patient-specific parameters, describing e.g. constitutive behavior, hemodynamics, boundary conditions, or local fiber orientation. Consequently, a repeated model evaluation for many different parameter sets is indispensable to personalize the model. The aim of parametric model order reduction (pMOR) is to find a reduced cardiovascular model that preserves the parameter-dependency, thus allowing a variation of any of the parameters directly in the reduced model without having to repeat the whole reduction process each time. The parametric reduced model can then be used e.g. for patient-specific parameter estimation or uncertainty quantification purposes. Note that a parametric solution of the ROM still follows the process as outlined in Algorithm 1, since pMOR subspace interpolation only influences the (offline) generation of the projection matrix.

To efficiently reduce the parametric cardiovascular model, the pMOR procedure is decomposed into an offline and online stage. In the *offline phase*, the parametrized full order model with n_p parameters $\boldsymbol{\mu} = [\mu_1, \dots, \mu_{n_p}]^T \in \mathbb{R}^{n_p}$ is first simulated for several parameter sample points $\boldsymbol{\mu}_k, k = 1, \dots, K$. Afterwards, the corresponding local projection bases $\mathbf{V}(\boldsymbol{\mu}_k)$ are computed via POD from the obtained data. In the *online phase*, the projection matrix $\mathbf{V}(\boldsymbol{\mu}^*)$ is generated for a new parameter value $\boldsymbol{\mu}^*$ by interpolating between the precomputed subspaces. Note that the selection of suitable parameter samples is highly problem-specific, depending mainly on desired accuracy and the parameter set, and can be challenging especially for high dimensional parameter spaces.

In this thesis, different subspace interpolation techniques are examined and explained in the following. It is supposed that local basis matrices $\mathbf{V}_1 = \mathbf{V}(\boldsymbol{\mu}_1), \dots, \mathbf{V}_K = \mathbf{V}(\boldsymbol{\mu}_K) \in \mathbb{R}^{n \times q}$ have been computed in the offline phase from the snapshot matrices $\mathbf{D}(\boldsymbol{\mu}_1), \dots, \mathbf{D}(\boldsymbol{\mu}_K) \in \mathbb{R}^{n \times n_s}$ at the sample points $\boldsymbol{\mu}_1, \dots, \boldsymbol{\mu}_K$. Each basis matrix $\mathbf{V}(\boldsymbol{\mu}_k)$ is composed of the vectors $\{\mathbf{v}_i(\boldsymbol{\mu}_k)\}_{i=1}^q$. For the interpolation, appropriate weighting functions $w_k(\boldsymbol{\mu}^*)$ should be selected to compute the interpolated basis $\mathbf{V}(\boldsymbol{\mu}^*)$ in the online phase. Basically, any multivariate interpolation method could be used for this purpose. Examples are polynomial interpolation (Lagrange polynomials), piecewise polynomial interpolation (splines), radial basis functions (RBF), Kriging interpolation

(Gaussian regression), inverse distance weighting (IDW) based on nearest-neighbor interpolation or even sparse grid interpolation [14]. For simplicity, in this thesis the special case of piecewise linear interpolation is considered. In this work, four interpolation methods are compared: weighted concatenation of bases (CoB), weighted concatenation of snapshots (CoS), adjusted direct basis interpolation, and basis interpolation on a Grassman manifold. These methods were chosen as they already have been used previously in similar interpolation settings, see [4] (Grassmann manifold) and [31] (CoS). The other methods, CoB and adjusted direct basis interpolation, can be seen as straight-forward adaptations thereof.

4.2.1 Weighted concatenation of bases

A common and straightforward approach to obtain a global basis matrix \mathbf{V} from the precomputed local bases $\mathbf{V}(\boldsymbol{\mu}_1), \dots, \mathbf{V}(\boldsymbol{\mu}_K)$ is given by the method concatenation of bases (CoB). With this technique, the local bases are at first concatenated side-by-side, followed by a SVD of the resulting matrix to compute the global basis \mathbf{V} . This technique can be extended by introducing the weighting functions $w_k(\boldsymbol{\mu}^*)$ in the concatenation of bases, in order to compute a *parameter-dependent* interpolated basis $\mathbf{V}(\boldsymbol{\mu}^*)$ which takes the distance of the new query point $\boldsymbol{\mu}^*$ with respect to the sample points $\boldsymbol{\mu}_1, \dots, \boldsymbol{\mu}_K$ into account. The matrices $\mathbf{V}(\boldsymbol{\mu}_1), \dots, \mathbf{V}(\boldsymbol{\mu}_K)$ are first weighted with weights $w_k(\boldsymbol{\mu}^*)$ and concatenated afterwards. Then, the SVD of the concatenated matrix

$$\tilde{\mathbf{V}}(\boldsymbol{\mu}^*) = [w_1(\boldsymbol{\mu}^*) \mathbf{V}(\boldsymbol{\mu}_1), \dots, w_K(\boldsymbol{\mu}^*) \mathbf{V}(\boldsymbol{\mu}_K)] = \tilde{\mathbf{U}}(\boldsymbol{\mu}^*) \tilde{\boldsymbol{\Sigma}}(\boldsymbol{\mu}^*) \tilde{\mathbf{T}}(\boldsymbol{\mu}^*)^\top \in \mathbb{R}^{n \times K \cdot q} \quad (4.32)$$

is performed. The interpolated basis $\mathbf{V}(\boldsymbol{\mu}^*)$ is finally constructed by considering the first q left singular vectors $\{\tilde{\mathbf{u}}_i(\boldsymbol{\mu}^*)\}_{i=1}^q$ that best represent the weighted and concatenated matrix

$$\mathbf{V}(\boldsymbol{\mu}^*) = [\tilde{\mathbf{u}}_1(\boldsymbol{\mu}^*), \dots, \tilde{\mathbf{u}}_q(\boldsymbol{\mu}^*)] \in \mathbb{R}^{n \times q}. \quad (4.33)$$

Please note that the described weighting procedure is purely optional. The advantage of the weighted approach is that subspaces near the interpolation point $\boldsymbol{\mu}^*$ are favored and stronger considered than subspaces describing the dynamics of far-distant sample points. However, this extended technique requires more computational effort than the classical concatenation approach, since a SVD has to be performed for every new $\boldsymbol{\mu}^*$ to compute the parameter-dependent interpolated basis $\mathbf{V}(\boldsymbol{\mu}^*)$.

4.2.2 Weighted concatenation of snapshots

The concatenation of bases approach explained in the previous section provides a basis $\mathbf{V}(\boldsymbol{\mu}^*)$ comprising the most important directions among the (weighted) basis vectors from all local bases. The bases $\mathbf{V}(\boldsymbol{\mu}_k) = \mathbf{U}(\boldsymbol{\mu}_k)(:, 1 : q)$ for $k = 1, \dots, K$ are however calculated in present case by means of the SVD-based technique of POD and essentially approximate the snapshot matrices

$$\mathbf{D}(\boldsymbol{\mu}_k) = \mathbf{U}(\boldsymbol{\mu}_k) \boldsymbol{\Sigma}(\boldsymbol{\mu}_k) \mathbf{T}(\boldsymbol{\mu}_k)^\top. \quad (4.34)$$

Since finding a basis that optimally approximates the system dynamics over a range of parameters is of major interest, the POD-case motivates construction of an interpolated basis $\mathbf{V}(\boldsymbol{\mu}^*)$

from a (weighted) concatenation of snapshots rather than from a (weighted) concatenation of bases. With the former technique, the matrix $\mathbf{V}(\boldsymbol{\mu}^*)$ is constructed by considering the first q left singular vectors of the (weighted and) concatenated snapshot matrix

$$\tilde{\mathbf{D}}(\boldsymbol{\mu}^*) = [w_1(\boldsymbol{\mu}^*) \mathbf{D}(\boldsymbol{\mu}_1), \dots, w_K(\boldsymbol{\mu}^*) \mathbf{D}(\boldsymbol{\mu}_K)] = \tilde{\mathbf{U}}_{\tilde{\mathbf{D}}}(\boldsymbol{\mu}^*) \tilde{\boldsymbol{\Sigma}}_{\tilde{\mathbf{D}}}(\boldsymbol{\mu}^*) \tilde{\mathbf{T}}_{\tilde{\mathbf{D}}}(\boldsymbol{\mu}^*)^\top \in \mathbb{R}^{n \times K \cdot n_s}. \quad (4.35)$$

Remark: Connection between the concatenation methods It can be shown that the described (weighted) concatenation of snapshots approach corresponds to a *modified* (weighted) concatenation of bases, where each vector $\mathbf{v}_i(\boldsymbol{\mu}_k)$ is weighted with the corresponding singular value $\sigma_i(\boldsymbol{\mu}_k)$ for all non-zero singular values. Thus, the first q left singular vectors of the modified matrix

$$\tilde{\mathbf{V}}(\boldsymbol{\mu}^*) = [w_1(\boldsymbol{\mu}^*) \mathbf{V}(\boldsymbol{\mu}_1) \boldsymbol{\Sigma}_q(\boldsymbol{\mu}_1), \dots, w_K(\boldsymbol{\mu}^*) \mathbf{V}(\boldsymbol{\mu}_K) \boldsymbol{\Sigma}_q(\boldsymbol{\mu}_K)] = \tilde{\mathbf{U}}(\boldsymbol{\mu}^*) \tilde{\boldsymbol{\Sigma}}(\boldsymbol{\mu}^*) \tilde{\mathbf{T}}(\boldsymbol{\mu}^*)^\top, \quad (4.36)$$

where $\boldsymbol{\Sigma}_q(\boldsymbol{\mu}_k) = \boldsymbol{\Sigma}(\boldsymbol{\mu}_k)(1 : q, 1 : q) \in \mathbb{R}^{q \times q}$, span the same interpolated subspace $\mathcal{V}(\boldsymbol{\mu}^*)$ as the q leading vectors in $\tilde{\mathbf{U}}_{\tilde{\mathbf{D}}}(\boldsymbol{\mu}^*)$.

4.2.3 Adjusted direct basis interpolation

It is well-known that a straightforward interpolation of the basis vectors comprised in the local projection matrices $\mathbf{V}(\boldsymbol{\mu}_1), \dots, \mathbf{V}(\boldsymbol{\mu}_K)$ does generally not yield a meaningful basis. The basis vectors $\{\mathbf{v}_i(\boldsymbol{\mu}_k)\}_{i=1}^q$ of different sample points span diverse subspaces, which have a distinct physical interpretation and might possibly point in opposite directions in space. Therefore, the basis vectors should be first arranged to point in similar directions to span similar subspaces, before their entries are interpolated. This adjustment is performed using the Modal Assurance Criterion (MAC) [1, 2]

$$\text{MAC}(\mathbf{v}_i, \mathbf{v}_j) = \frac{|\mathbf{v}_i^\top \cdot \mathbf{v}_j|^2}{\|\mathbf{v}_i\|_2^2 \cdot \|\mathbf{v}_j\|_2^2} \in [0, 1], \quad (4.37)$$

which provides a measure of similarity or linear dependence between the vectors \mathbf{v}_i and \mathbf{v}_j . Using the symmetry of the MAC, (4.37) needs to be evaluated $q(q+1)/2$ times. The maximal value of the MAC is 1, which corresponds to linear dependent vectors, whereas orthogonal vectors take the minimal value 0. Hence, the idea is to only interpolate vectors which are strongly correlated to each other and maximize the MAC. To do so, first a reference subspace has to be selected with respect to which the adjustment of the bases should be performed. The reference subspace, spanned by the columns of $\mathbf{R}_\mathbf{V} \in \mathbb{R}^{n \times q}$, should ideally comprise the most important dynamics among all parameter sample points and be representative for all local bases. The simplest way to select $\mathbf{R}_\mathbf{V}$ is to take one particularly important local basis $\mathbf{R}_\mathbf{V} = \mathbf{V}_{k_0}$ with $k_0 \in \{1, \dots, K\}$. Another possibility is to construct the reference subspace similarly as described in Section 4.2.1, i.e. using the (weighted) concatenation of bases approach, yielding $\mathbf{R}_\mathbf{V} = \tilde{\mathbf{U}}(:, 1 : q)$ or $\mathbf{R}_\mathbf{V}(\boldsymbol{\mu}^*) = \tilde{\mathbf{U}}(\boldsymbol{\mu}^*)(:, 1 : q)$. Once the reference subspace has been selected, the vectors $\mathbf{v}_{i^*(j,k)}(\boldsymbol{\mu}_k)$ that fulfill

$$i^*(j, k) = \underset{i}{\operatorname{argmax}} \text{MAC}(\mathbf{v}_i(\boldsymbol{\mu}_k), \mathbf{R}_\mathbf{V}(:, j)) \quad \text{for } j = 1, \dots, q \text{ and } k = 1, \dots, K \quad (4.38)$$

are taken for interpolation. Furthermore, the orientation of the vectors $\mathbf{v}_{i^*(j,k)}(\boldsymbol{\mu}_k)$ and $\mathbf{R}_\mathbf{v}(:, j)$ is equalized by adapting the sign, in order to avoid that an interpolation between (almost) anti-parallel vectors results in a mutual cancellation. Finally, the interpolation of the vectors is given by

$$\bar{\mathbf{v}}_j(\boldsymbol{\mu}^*) = \sum_{k=1}^K w_k(\boldsymbol{\mu}^*) \cdot [\pm \mathbf{v}_{i^*(j,k)}(\boldsymbol{\mu}_k)] \quad \text{with} \quad \sum_{k=1}^K w_k(\boldsymbol{\mu}^*) = 1. \quad (4.39)$$

The interpolation of orthonormal vectors does not necessarily yield a set of orthonormal vectors. Therefore, the interpolated vectors $\{\bar{\mathbf{v}}_j(\boldsymbol{\mu}^*)\}_{j=1}^q$ are subsequently orthonormalized by employing the SVD of $\bar{\mathbf{V}}(\boldsymbol{\mu}^*)$

$$\bar{\mathbf{V}}(\boldsymbol{\mu}^*) = [\bar{\mathbf{v}}_1(\boldsymbol{\mu}^*), \dots, \bar{\mathbf{v}}_q(\boldsymbol{\mu}^*)] = \bar{\mathbf{U}}(\boldsymbol{\mu}^*) \bar{\boldsymbol{\Sigma}}(\boldsymbol{\mu}^*) \bar{\mathbf{T}}(\boldsymbol{\mu}^*)^\top \quad (4.40)$$

and considering the first q left singular vectors $\{\bar{\mathbf{u}}_j(\boldsymbol{\mu}^*)\}_{j=1}^q$ for the interpolated basis $\mathbf{V}(\boldsymbol{\mu}^*) \in \mathbb{R}^{n \times q}$.

Special case of two precomputed bases and one parameter In order to make the afore explained method clearer, the special case of two precomputed bases ($K = 2$) and one single parameter ($n_p = 1$) is now briefly presented. Let us assume that bases $\mathbf{V}(\mu_1)$ and $\mathbf{V}(\mu_2)$ have been computed at the parameter sample points μ_1 and μ_2 , and that the new parameter value μ^* lies between these two samples. Suppose that the reference basis is chosen e.g. as $\mathbf{R}_\mathbf{v} = \mathbf{V}(\mu_2)$. Then, the vectors $\mathbf{v}_{i^*(j)}(\mu_1)$ that fulfill

$$i^*(j) = \underset{i}{\operatorname{argmax}} \operatorname{MAC}(\mathbf{v}_i(\mu_1), \mathbf{v}_j(\mu_2)) \quad \text{for } j = 1, \dots, q \quad (4.41)$$

are selected to be combined with the vectors $\mathbf{v}_j(\mu_2)$. The interpolation reads

$$\bar{\mathbf{v}}_j(\boldsymbol{\mu}^*) = w(\boldsymbol{\mu}^*) \cdot [\pm \mathbf{v}_{i^*(j)}(\mu_1)] + (1 - w(\boldsymbol{\mu}^*)) \cdot \mathbf{v}_j(\mu_2) \quad (4.42)$$

with the weight

$$w(\boldsymbol{\mu}^*) = \frac{\mu^* - \mu_2}{\mu_1 - \mu_2} \in [0, 1] \quad \text{for } \mu^* \in [\mu_1, \mu_2], \quad (4.43)$$

providing that a linear interpolation is employed.

4.2.4 Basis interpolation on a Grassmannian manifold

As discussed before, a direct interpolation of the local bases is not meaningful, since they span different subspaces. In addition to the afore-explained adjustment of the bases before interpolation, one may also interpolate the underlying subspaces on a tangent space of a manifold. The method proposed by Amsallem and Farhat [4] constructs a basis matrix $\mathbf{V}(\boldsymbol{\mu}^*)$ for a new parameter point $\boldsymbol{\mu}^*$ by interpolating the subspaces corresponding to the bases $\{\mathbf{V}(\boldsymbol{\mu}_k)\}_{k=1}^K$ on the tangent space to the Grassmannian manifold $\mathcal{G}_q(\mathbb{R}^n)$.

The first step of the approach consists in choosing a local basis matrix \mathbf{V}_{k_0} for the reference point $\mathcal{V}_{k_0} \in \mathcal{G}_q(\mathbb{R}^n)$, at which the tangent space $\mathcal{T}_{\mathcal{V}_{k_0}}$ to the manifold $\mathcal{G}_q(\mathbb{R}^n)$ is constructed. Afterwards, all subspaces $\mathcal{V}(\boldsymbol{\mu}_k)$ spanned by the local bases $\mathbf{V}(\boldsymbol{\mu}_k)$ are mapped onto this tangent space by the so-called logarithmic mapping: $\text{span}(\boldsymbol{\Gamma}_k) = \text{Log}_{\mathcal{V}_{k_0}}(\mathcal{V}_k) \in \mathcal{T}_{\mathcal{V}_{k_0}}$. This is done basically by computing K thin SVDs

$$(\mathbf{I} - \mathbf{V}_{k_0} \mathbf{V}_{k_0}^\top) \mathbf{V}(\boldsymbol{\mu}_k) (\mathbf{V}_{k_0}^\top \mathbf{V}(\boldsymbol{\mu}_k))^{-1} = \mathbf{U}(\boldsymbol{\mu}_k) \boldsymbol{\Sigma}(\boldsymbol{\mu}_k) \mathbf{T}(\boldsymbol{\mu}_k)^\top \quad \text{for } k = 1, \dots, K \quad (4.44)$$

and then calculating

$$\boldsymbol{\Gamma}(\boldsymbol{\mu}_k) = \mathbf{U}(\boldsymbol{\mu}_k) \arctan(\boldsymbol{\Sigma}(\boldsymbol{\mu}_k)) \mathbf{T}(\boldsymbol{\mu}_k)^\top. \quad (4.45)$$

In order to compute the orthonormal basis $\mathbf{V}(\boldsymbol{\mu}^*)$ for a new parameter point $\boldsymbol{\mu}^*$, the matrices $\{\boldsymbol{\Gamma}(\boldsymbol{\mu}_k)\}_{k=1}^K$ are first interpolated using the weights $w_k(\boldsymbol{\mu}^*)$ to obtain

$$\boldsymbol{\Gamma}^* = \boldsymbol{\Gamma}(\boldsymbol{\mu}^*) = \sum_{k=1}^K w_k(\boldsymbol{\mu}^*) \boldsymbol{\Gamma}(\boldsymbol{\mu}_k). \quad (4.46)$$

The interpolated subspace $\text{span}(\boldsymbol{\Gamma}^*) \in \mathcal{T}_{\mathcal{V}_{k_0}}$ is then mapped back to the original manifold $\mathcal{G}_q(\mathbb{R}^n)$ by the so-called exponential mapping: $\mathcal{V}(\boldsymbol{\mu}^*) = \text{Exp}_{\mathcal{V}_{k_0}}(\text{span}(\boldsymbol{\Gamma}^*)) \in \mathcal{G}_q(\mathbb{R}^n)$. The back-mapping step is numerically achieved by computing a thin SVD

$$\boldsymbol{\Gamma}(\boldsymbol{\mu}^*) = \mathbf{U}(\boldsymbol{\mu}^*) \boldsymbol{\Sigma}(\boldsymbol{\mu}^*) \mathbf{T}(\boldsymbol{\mu}^*)^\top, \quad (4.47)$$

followed by

$$\mathbf{V}(\boldsymbol{\mu}^*) = \mathbf{V}_{k_0} \mathbf{T}(\boldsymbol{\mu}^*) \cos(\boldsymbol{\Sigma}(\boldsymbol{\mu}^*)) + \mathbf{U}(\boldsymbol{\mu}^*) \sin(\boldsymbol{\Sigma}(\boldsymbol{\mu}^*)). \quad (4.48)$$

The special case of two precomputed bases ($K = 2$) and one single parameter ($n_p = 1$) is extensively described in [4].

4.3 Numerical results and discussion

In this section, results are presented for the approximation of the FOM simulation with ROM simulations. It is distinguished between model order reduction and parametric model order reduction. For a fixed parameter set, using the contractility $\sigma_0 = 280$ kPa, the approximation qualities of POD are explored in Section 4.3.3. Afterwards, the approximation quality is analyzed with respect to a changing contractility in Section 4.3.4. As snapshots, all time steps of the simulation of a single heartbeat are used with $n_s = 874$.

4.3.1 Model definition

The discretized patient-specific four-chamber cardiac geometry from Section 3.5 with $n = 846\,864$ structural degrees of freedom is displayed in Figure 4.2. The weak form of the initial

boundary value problem (IBVP) is

$$\begin{aligned}
 0 = & \int_{\Omega_0} \rho_0 \ddot{\mathbf{u}} \cdot \delta \mathbf{u} \, dV + \int_{\Omega_0} \mathbf{S} : \delta \mathbf{E} \, dV + \int_{\Gamma_0^{\text{endo},l}} p_v \mathbf{F}^{-\top} \cdot \mathbf{N} \cdot \delta \mathbf{u} \, dA \\
 & + \int_{\Gamma^{\text{vess}}} [k_v \mathbf{u} + c_v \dot{\mathbf{u}}] \cdot \delta \mathbf{u} \, dA + \int_{\Gamma^{\text{epi}}} \mathbf{N} [k_p \mathbf{u} \cdot \mathbf{N} + c_p \dot{\mathbf{u}} \cdot \mathbf{N}] \cdot \delta \mathbf{u} \, dA,
 \end{aligned} \tag{4.49}$$

with structure-Windkessel coupling on the left ventricular endocardium $\Gamma_0^{\text{endo},l}$, left ventricular pressure p_v , omni-directional spring-dashpots on the outsides of the great vessels Γ^{vess} , and pericardial boundary conditions on the epicardial surface Γ^{epi} . Spring stiffnesses k_v , k_p and dashpot viscosities c_v , c_p model the attachments of the great vessels and the pericardium, respectively. The different colors in Figure 4.2 relate to different materials for adipose tissue (4.50), aorta, pulmonary artery, and atrial myocardium (4.51), and ventricular myocardium (4.52):

$$\mathbf{S} = \frac{\partial}{\partial \mathbf{E}} (\psi_{\text{NH}} + \psi_{\text{vol},a}) + \frac{\partial}{\partial \dot{\mathbf{E}}} \psi_{\text{visco}}, \tag{4.50}$$

$$\mathbf{S} = \frac{\partial}{\partial \mathbf{E}} (\psi_{\text{MR}} + \psi_{\text{vol},a}) + \frac{\partial}{\partial \dot{\mathbf{E}}} \psi_{\text{visco}}, \tag{4.51}$$

$$\mathbf{S} = \frac{\partial}{\partial \mathbf{E}} (\psi_{\text{MR}} + \psi_{\text{vol},a}) + \frac{\partial}{\partial \dot{\mathbf{E}}} \psi_{\text{visco}} + \mathbf{S}_{\text{act}}, \tag{4.52}$$

with isotropic Neo-Hooke material ψ_{NH} (2.60), isotropic Mooney-Rivlin material ψ_{MR} (2.62), volumetric penalty $\psi_{\text{vol},a}$ (2.63), viscous material ψ_{visco} (2.65), and active stress \mathbf{S}_{act} (2.66) from Section 2.4. Each material is composed of a hyperelastic and a viscous contribution. Only the ventricular myocardial tissue in (3.13) has an additional active stress component \mathbf{S}_{act} , using a $\pm 60^\circ$ fiber distribution. The model's parameters are given in Table A.7.

4.3.2 Implementation details

The coupled FOM and ROM in (2.75) and (4.23), respectively, are solved using the in-house parallel high-performance finite element software package BACI [181]. The code is implemented in C++ making use of the Trilinos library [81]. To solve FOM's large linear system in (2.75) a parallel iterative GMRES solver is used with 2×2 block SIMPLE-like preconditioning. For the ROM's small linear system in (4.23) a serial direct solver is used. All preliminary calculations, i.e. singular value decompositions and the interpolation of subspaces, are performed in MATLAB (Release 2017b, The MathWorks, Inc., Natick, MA, USA).

Remark As later outlined in Section 4.3.3.3, the matrix-matrix and vector-matrix multiplications required to reduce the FOM consume much more time than the actual solution of the reduced model itself. The computational efficiency of these multiplications is thus crucial for the speedup of the ROM. Thus, use is made of readily available C++ multiplication functions provided by the Epetra package within the Trilinos library. The projection matrix \mathbf{V} is dense with one dimension much smaller than the other due to $q \ll n$ and thus stored in an `Epetra_MultiVector`.

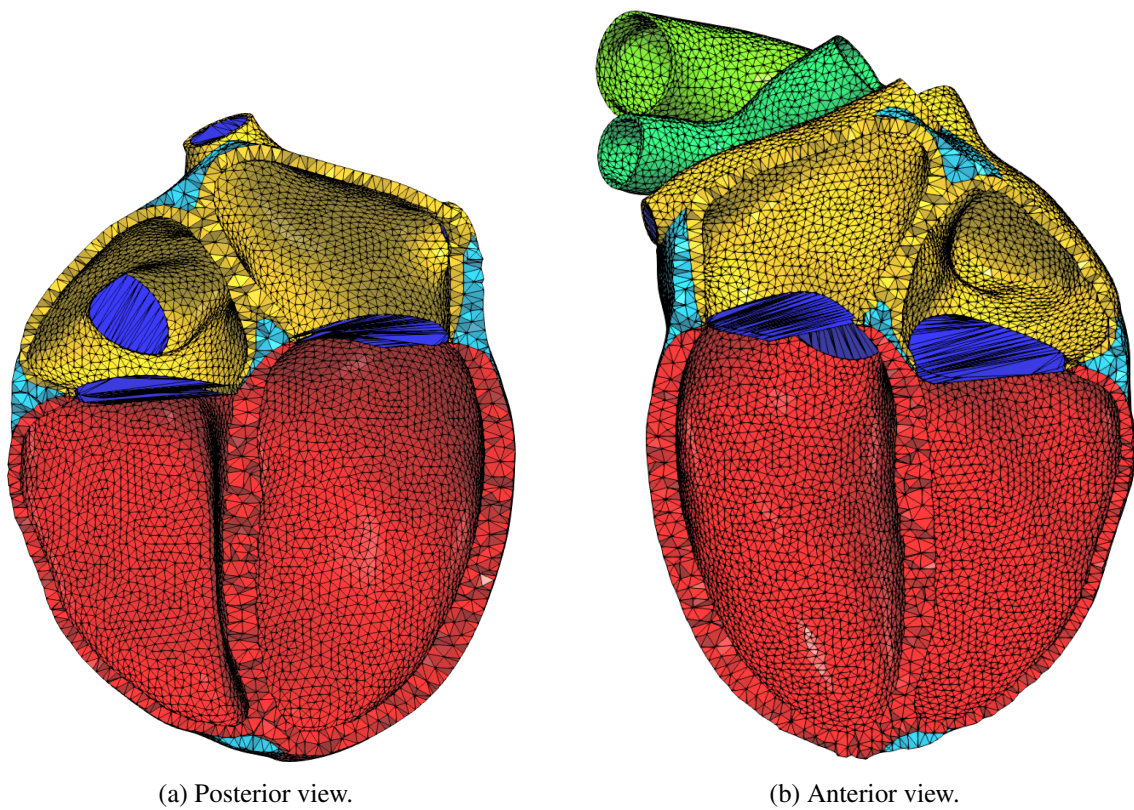


Figure 4.2: Computational mesh with quadratic tetrahedral elements cut in four-chamber view, colored by different materials: adipose tissue (cyan), atrial myocardium (yellow), ventricular myocardium (red), aorta and pulmonary artery (green), valve planes (blue).

4.3.3 Model order reduction

In this section, the reducibility of the coupled hemodynamical-structural simulation model of a cardiac cycle is demonstrated and computational costs are compared. Following analysis of the heart's eigenmodes in Section 4.3.3.1, the approximation quality of POD is investigated using a varying number of modes $q \in \{10, 50, 100, 200, 300, 400, 500\}$ in Section 4.3.3.2. The model ROM10 was the model with the smallest mode number, where the cardiac simulation converged to a result in all time steps. The highest mode number for ROM500 was chosen, since there is a plateau around $q = 500$ in the decay of singular values in Figure 4.4a. The computational speedup achieved by using POD is further demonstrated in Section 4.3.3.3 using again varying mode numbers.

4.3.3.1 POD-modes of the heart

To study the reducibility of the cardiac model, the decay of the singular values compared to the first one is analyzed. This gives a measure of relative importance of the modes selected by POD. In Figure 4.4a the normalized singular value σ_i/σ_1 of mode i is shown. For modes $i < 50$ there is a fast decay in relative importance, indicating good reducibility. There is a plateau for $250 < i < 700$, indicating that not much new information is gained by including those modes in the ROM.

The first modes of the heart are visualized in Figure 4.3, where the heart is cut in four-chamber-view. The simulation in reference configuration and at end-systole are shown in Figures 4.3a and 4.3b, respectively. Mode $i = 1$ in Figure 4.3c exhibits great similarity to the solution at end-systole and is characterized by a movement of the atrioventricular plane towards the apex with negligible change in outer shape of the heart. Mode $i = 2$ in Figure 4.3d consists of a more radial displacement of the outer walls of the ventricles and a pendulum motion of the intraventricular septum. Mode $i = 3$ in Figure 4.3e displays a rotating motion of the ventricles together with a large left-to-right movement of the intraventricular septum.

4.3.3.2 Approximation quality

To quantify the overall approximation quality of ROM simulations of a full heartbeat, a spatial error compared to the FOM solution is calculated. Here, the spatial $\epsilon_{\infty, \infty}$ -error is defined

$$\epsilon_{\infty, \infty} = \max_{t_j} \left[\max_k \left\| \mathbf{d}_{\text{ROM}}^k(t_j) - \mathbf{d}_{\text{FOM}}^k(t_j) \right\| \right] \quad (4.53)$$

with $\mathbf{d}_{\text{ROM}}^k(t_j)$ and $\mathbf{d}_{\text{FOM}}^k(t_j)$ as nodal displacements at node k at time step t_j of ROM and FOM respectively. The spatial $\epsilon_{\infty, \infty}$ -error thus gives the highest displacement error at any node at any time step and is an upper bound for all spatial approximation errors. The $\epsilon_{\infty, \infty}$ -error is shown in Figure 4.4b depending on the number of reduced modes q . It is clearly evident that the approximation error strongly decreases, when more modes are used for the approximation. Remarkably, even for the very low number of 10 modes a solution is obtained whose largest approximation error at any node at any time step is below 1 mm, which is the order of magnitude of the MRI resolution from which the geometry was obtained. Furthermore, using ROM simulations with a reduced order of $q > 300$ does not yield significant improvements in terms of accuracy. This

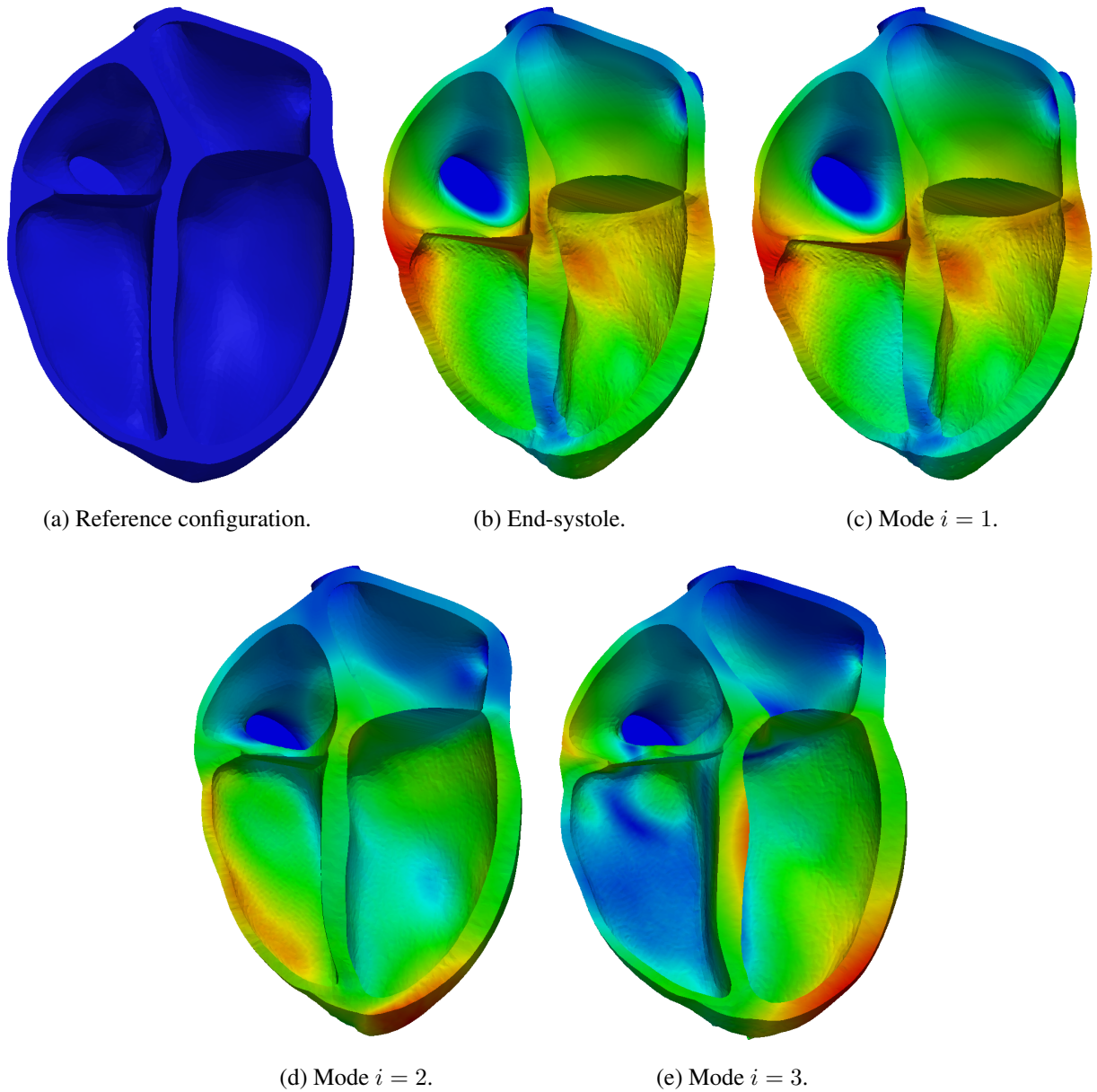
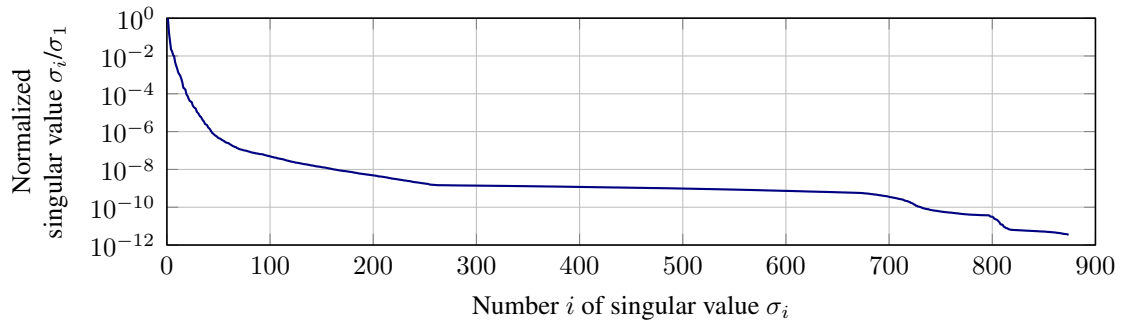
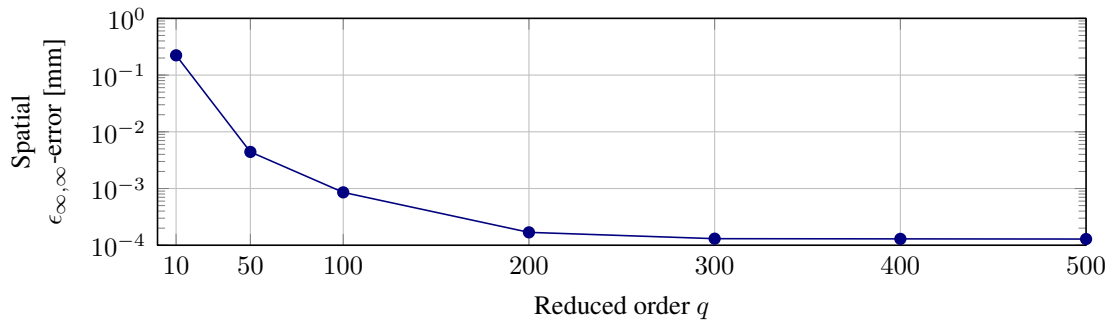


Figure 4.3: Visualized displacements in four-chamber-view. Displacements increase from blue to red regions.



(a) Decay of normalized singular values.



(b) Spatial $\epsilon_{\infty, \infty}$ -error compared to FOM depending on reduced order q .

Figure 4.4: Accuracy of ROM.

is in agreement with the decay of the normalized singular values in Figure 4.4a, where modes $q > 300$ contain little more information than the preceding ones.

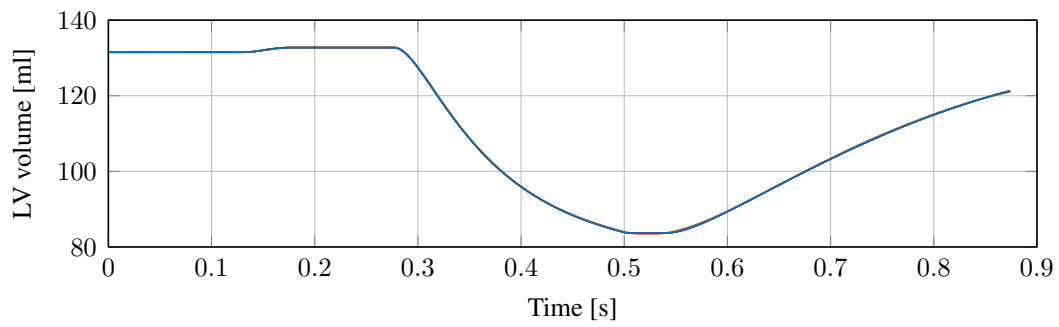
For many medical applications, it is not necessary to calculate an accurate spatial displacement field. Rather, there are a couple of scalar quantities which are used in clinical practice as a cardiac performance indicator or for the prediction of disease progression for instance. Such a quantity is the ejection fraction

$$\text{EF} = \frac{\max_t V(t) - \min_t V(t)}{\max_t V(t)}, \quad (4.54)$$

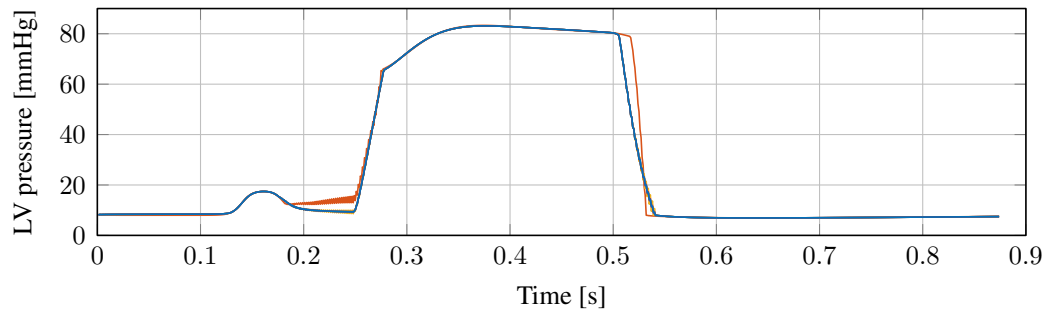
which is calculated from left or right ventricular volume. To evaluate the approximation of the EF by a ROM simulation, in Figure 4.5a the left ventricular (LV) volume curves of the FOM simulation is compared to ROM simulations of various reduced orders q . It shows that minimum and maximum volume are approximated well and the time curves are almost indistinguishable. Left ventricular pressure over time is further compared for all simulations in Figure 4.5b. Again, key features such as maximum pressure are approximated well. Minor oscillations occur for ROM10 and ROM50 after the closure of the mitral valve at $t \approx 0.2$. Furthermore, the closure of the aortic valve at $t \approx 0.5$ is delayed slightly for simulation ROM10.

4.3.3.3 Speedup

For performance measurements, all FOM and ROM simulations are run on a single node of our Linux cluster. One node features 64 GB of RAM and two Intel Xeon E5-2680 "Haswell"



(a) Left ventricular volume.



(b) Left ventricular pressure.

— FOM — ROM10 — ROM50 — ROM100 — ROM200 — ROM300 — ROM400 — ROM500

Figure 4.5: Scalar outputs of FOM and various ROMs over time.

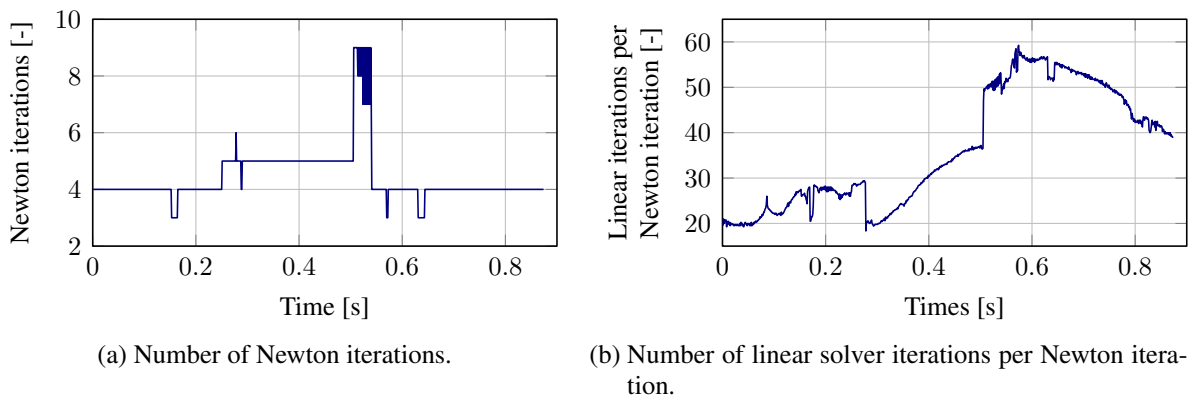


Figure 4.6: Solver performance of FOM in each time step.

processors, each equipped with 12 cores operating at a frequency of 2.5 GHz. In Figure 4.6 a brief overview of the numerical performance of the FOM simulation is given. In Figure 4.6a the number of Newton iterations is shown in each time step. The number of Newton iterations is between three and nine. It is elevated to five during ventricular systole and rises to nine at end-systole, where the aortic valve closes. The number of linear solver iterations of each Newton iteration at a given time step is shown in Figure 4.6b. The number of linear iterations is between 20 and 60 and shows similar trends as the number of Newton iterations. This performance is reasonable and assures a good basis to which ROM simulations can be compared to. In the following, simulation time is compared exclusively, excluding time for creating the projection matrix \mathbf{V} . The projection matrix is calculated once in a preliminary step using the same hardware and requires only about one minute. Due to the repeated evaluation of the MAC, the direct interpolation method is in this example about three times as expensive as the other interpolation methods, which perform equally.

The computation time of ROM simulations with various reduced orders q is compared to the total FOM simulation time in Figure 4.7. Firstly, the speedup factor α of ROM over FOM simulations is shown in Figure 4.7a. The effect of POD is evident for ROM simulations between $q = 500$ and $q = 10$, where a speedup of $\alpha \approx 5$ and $\alpha \approx 13$ over the FOM simulation, respectively, is achieved. Note that while achieving high speedups hardware demands are not lowered. The RAM consumption has actually increased slightly for ROM simulations, since the projection matrix \mathbf{V} needs to be stored additionally. Hyper-reduction might be used in future studies to lower RAM consumption as here the residual and Jacobian are only assembled partially.

In Figure 4.7b it is distinguished between three components of total computation time. Component *Linear system* includes the time required for the multiplications of the projection matrix \mathbf{V} with the blocks of the Jacobian matrix in (4.23) as well as the time to solve the reduced linear system. This component strongly depends on the reduced order q as it scales with the complexity of the matrix-matrix multiplications, which is the main time contributor. The solution time of the reduced linear system itself is negligible. Component *Evaluate elements* contains time spent during element evaluation to assemble the block Jacobian matrix and the right-hand side. As expected, this component is independent of q , since the full system is still built before projecting it to the q -dimensional subspace. Component *Other* sums up all other time spent during the simulation, e.g. file input and output or general overhead, and is also independent of q .

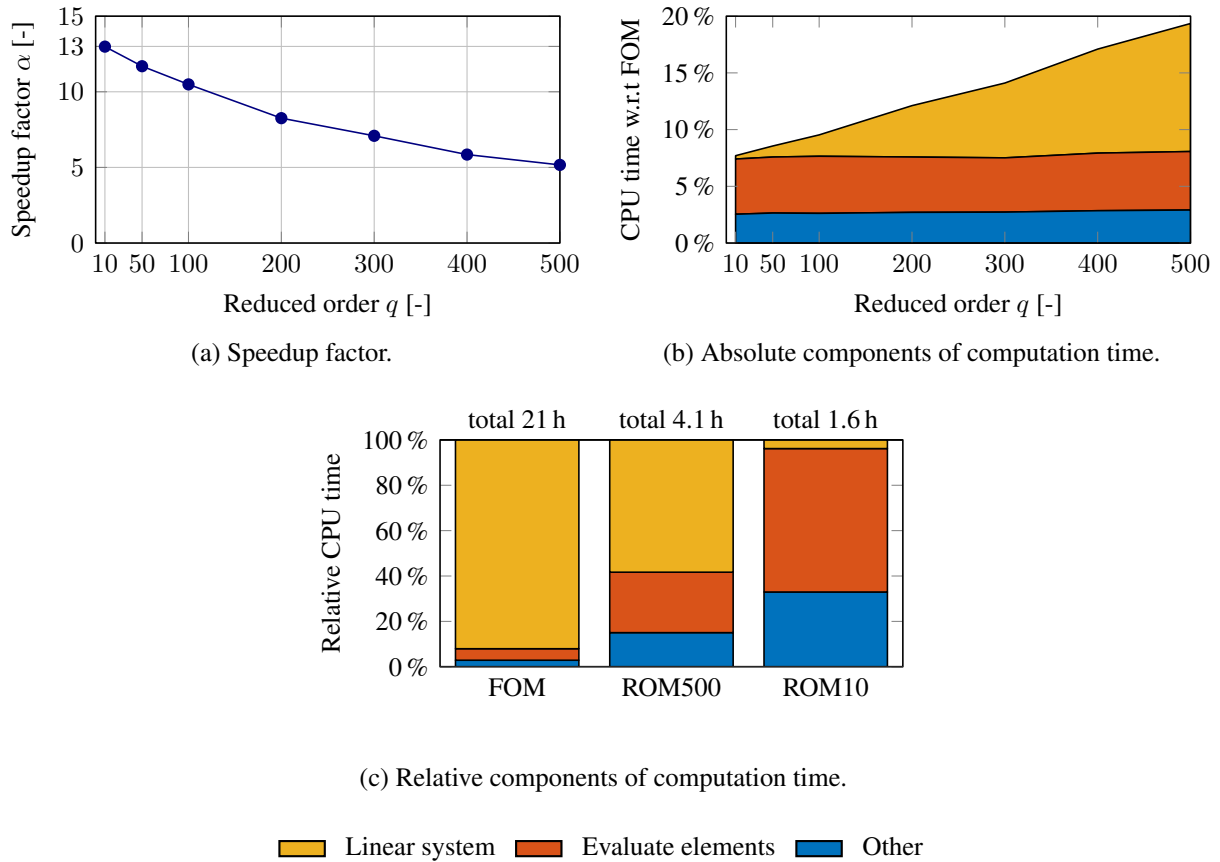


Figure 4.7: Simulation times of FOM and ROM.

In Figure 4.7c the relative distribution of simulation time for FOM, ROM500, and ROM10 is shown. For the 21 hours spent during a FOM simulation, 92% of simulation time are spent solving the linear system. This large proportion shows the potential for savings using MOR with POD and is in part a consequence of the efficient parallelization of the group's finite element code [181]. Reducing and solving the linear system in ROM10 only makes up 4% of the simulation time. However, the new bottleneck is now the element evaluation at 63% of the simulation time. This motivates the use of hyper-reduction methods, such as the discrete empirical interpolation method (DEIM) [35] for ROMs with very few degrees of freedom.

4.3.4 Parametric model order reduction

In this section a quantitative comparison of several subspace interpolation methods introduced in Section 4.2 is provided for parametric model order reduction (pMOR) to demonstrate the ability to evaluate the ROM simulations at parameter sets without prior FOM knowledge. The contractility σ_0 in (2.67) is varied, controlling the upper limit of the myocardium's active stress in fiber direction. It is a key parameter of cardiac contraction and has a major influence on elastodynamics as well as on several scalar cardiac measures. It is commonly calibrated to match the end-systolic volume of the left ventricle as measured in cine MRI. In this work, the contrac-

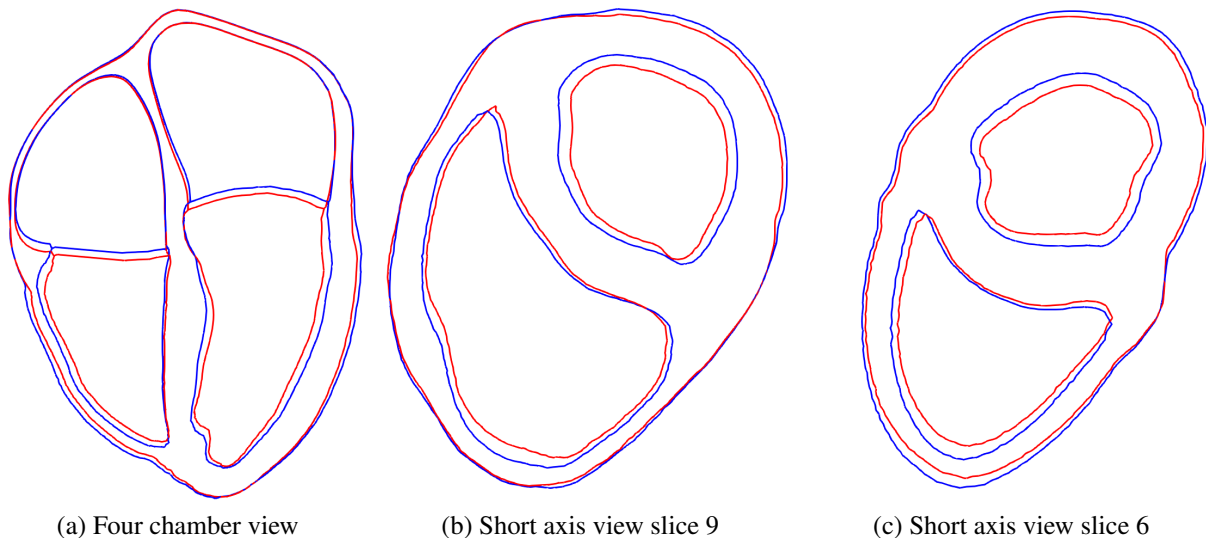


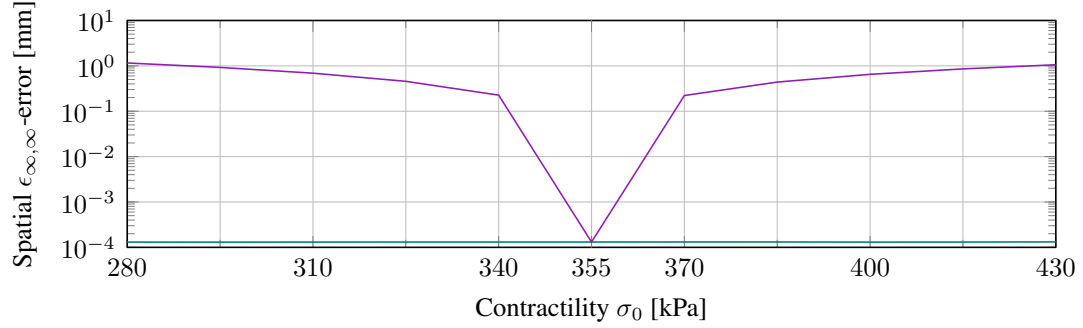
Figure 4.8: Simulation results of the FOM at end-systole for $\sigma_0 = 280$ kPa (blue) and $\sigma_0 = 430$ kPa (red). Views as defined in Figure 3.7.

tility $\sigma_0 \in [280 \text{ kPa}, 430 \text{ kPa}]$ is varied, as this range produces FOM simulation results that are in agreement with cine MRI. The displacement results at the limits of the parameter range are shown for the FOM in Figure 4.8. The dimension $q = 300$ is used for all ROM simulations in this section, since it was shown in Figure 4.4b that no further improvements are made in approximation quality for $q > 300$. In Section 4.3.4.1 the approximation quality is demonstrated with respect to the spatial displacement field. However, in many clinical applications a full solution of the displacements is not needed. Therefore, the approximation quality of pMOR is shown with respect to scalar cardiac quantities of clinical significance in Section 4.3.4.2.

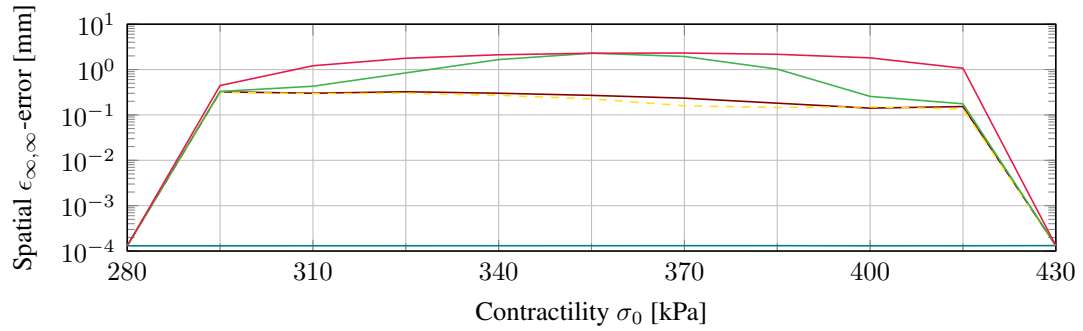
4.3.4.1 Approximation of displacements

In Figure 4.9 the spatial $\epsilon_{\infty, \infty}$ -error is compared for a varying contractility. pMOR simulations using snapshots of FOM simulations are compared from one, two, and four σ_0 -sample points in figures 4.9a, 4.9b, and 4.9c, respectively. For comparison, we additionally compute a non-parametric ROM, denoted as direct ROM simulations in the following. Here, for every σ_0 we evaluate the FOM to generate the corresponding projection matrix $\mathbf{V}(\sigma_0)$. This information is however not used in the pMOR solutions displayed and would not be available in a typical MOR scenario, rendering MOR useless. The direct ROM approximation error is mostly independent of the choice of parameter σ_0 .

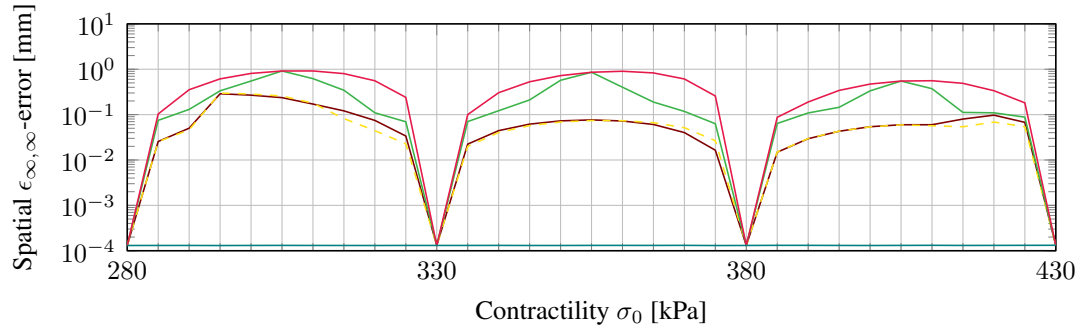
In Figure 4.9a the MOR approximation is shown with varying σ_0 and a constant projection matrix $\mathbf{V}(\sigma_{0,1})$ which was obtained from a single FOM simulation with sample point $\sigma_{0,1} = 355$ kPa. Technically, this would not be considered in pMOR, since the projection matrix is not adapted to the parameter set. It can be observed that MOR simulations with $\sigma_0 \neq \sigma_{0,1}$ provide reasonable results with a spatial error below 1 mm using $\mathbf{V}(\sigma_{0,1})$. However, with an increasing range of the parameter interval, the additional effort of subspace interpolation becomes advantageous. The approximation error of MOR simulations using two and four sample points are



(a) One sample point $\sigma_{0,1} = 355$ kPa, increment $\Delta\sigma = 15$ kPa.



(b) Two sample points $\sigma_{0,k} = \{280, 430\}$ [kPa], increment $\Delta\sigma = 15$ kPa.



(c) Four sample points $\sigma_{0,k} = \{280, 330, 380, 430\}$ [kPa], increment $\Delta\sigma_0 = 5$ kPa.



Figure 4.9: Spatial $\epsilon_{\infty, \infty}$ -error for direct ROM300, constant ROM300, and pROM300 with different interpolation techniques for a varying number of sample points.

displayed in Figures 4.9b and 4.9c, respectively. Both studies show similar results. The error is highest between sample points and approaches the error of the direct ROM simulations close to the sample points. The pMOR approximation errors are reduced when using a finer resolution of sample points. The subspace interpolation with the largest spatial error is obtained by the Grassmannian manifold and concatenation of bases (CoB) methods, coinciding in the middle between two sample points. An error of one order of magnitude smaller is achieved by using the concatenation of snapshots (CoS) and the adjusted direct interpolation methods, staying well below a spatial $\epsilon_{\infty, \infty}$ -error of 1 mm.

The adjusted direct interpolation method performs reasonably well in this example due to the POD of both snapshot matrices of the left and right sample point yielding modes that allow for a distinctive pairing according to the MAC. However, the same subspace can be spanned by two sets of orthogonal basis vectors which are not necessarily linearly dependent. If the information of a mode related to the left sample point is scattered among various modes corresponding to the right sample point, the direct interpolation method will most probably yield considerably worse results.

The CoS method is in the present case far superior to the CoB method. As outlined in Section 4.2, the CoS method allows for a direct usage of the snapshots at the sample points, while the CoB method uses the projection matrices computed at the sample points. The projection matrices, as compared to the snapshots, contain no information about the relative importance of the modes. The snapshots thus contain more information about the dynamics of the system, enabling the CoS method to select a more suitably interpolated subspace than the CoB method. Note that the CoS method can only be applied when using it in combination with an observation-based reduction technique like POD.

4.3.4.2 Approximation of scalar cardiac quantities

In Figure 4.10 scalar output quantities of the cardiac model are shown, evaluated for the same MOR simulations as in Figure 4.9 using one, two, and four sample points in figures 4.10a, 4.10b, and 4.10c, respectively. For each study ejection fraction (EF), maximum left ventricular pressure (LVP), and maximum left atrioventricular plane displacement (LAVPD) are evaluated and compared to the the FOM results. All three output quantities are important determinants of cardiac viability. They are also chosen because they allow the study of the approximation of different outputs of the coupled 3D-0D elasto-hemodynamical model with pMOR. EF, as defined in (4.54), is an integral value of the spatial displacement field. LVP is an output of the 0D Windkessel model and LAVPD is the average of a small subset of nodal directional displacements.

For one sample point, the FOM solution in Figure 4.10a is again compared to the solution of a ROM using a constant projection matrix. The parameter dependence of the three cardiac quantities on σ_0 is reproduced well by the constant ROM simulations. As expected, the deviations from the FOM solution are largest at evaluations furthest away from the sample point. However, the accuracy might still be sufficient for many applications. The cardiac quantities using two and four sample points are shown in Figures 4.10b and 4.10c, respectively. For clarity, only the results of the subspace interpolation methods which performed best and worst in Figure 4.9 are shown here, which are the CoS and Grassmann method, respectively. The outputs oscillate visibly between sample points when using the Grassmann interpolation method, improving as the

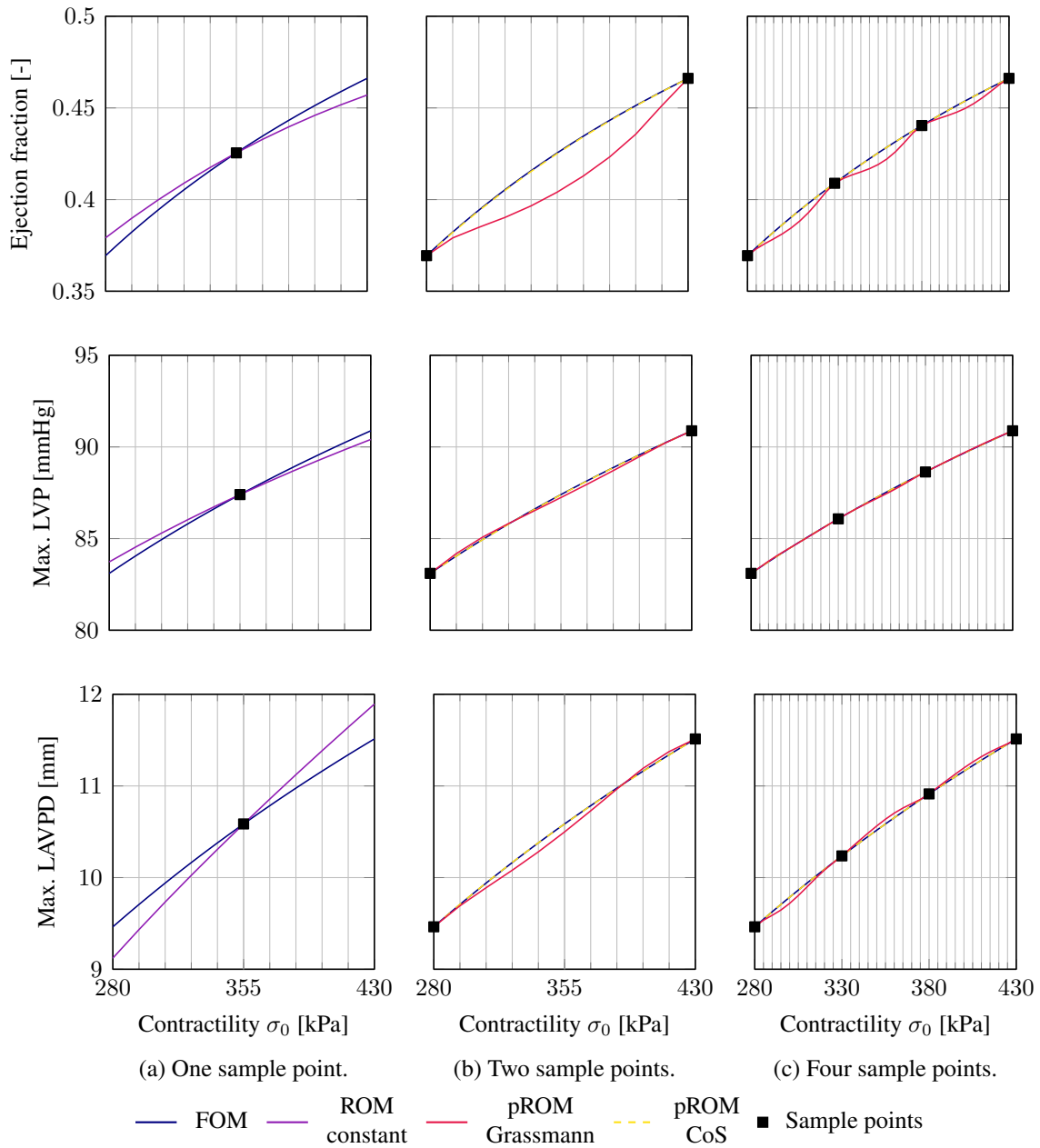


Figure 4.10: Scalar cardiac quantities ejection fraction (top), maximal left ventricular pressure (middle), and maximal left atrioventricular plane displacement (bottom) for varying contractility σ_0 in FOM and ROM300.

resolution of sample points is refined. As in Figure 4.9, the CoS method performs well, leading to a good approximation of the scalar cardiac quantities between sample points. Furthermore, comparing Figures 4.10b and 4.10c to Figure 4.10a, it is visible that using pROM with CoS interpolation yields not only a good approximation of the function *values* but also improves the *tangent* with respect to the contractility, compared to using constant ROM with a single sample point.

4.4 Conclusion

In this chapter, a new projection-based reduced order model for coupled structure-Windkessel cardiac models was proposed, where only the large structural dimension was reduced. Specifically, a nonlinear large deformation cardiac Finite Element model was used with pericardial boundary conditions. For subspace generation, proper orthogonal decomposition (POD) was applied to displacement snapshots of the full order model (FOM). The accuracy and speedup of the reduced order model (ROM) was demonstrated for a range of reduced dimensions $q \in \{10, \dots, 500\}$. In that range, the approximation error was found to lie between $2 \cdot 10^{-1}$ mm and $1 \cdot 10^{-4}$ mm, which is well below the resolution of state of the art cardiac imaging employed in current clinical practice. For these simulations, speedups between 13 and 5 times over the FOM were achieved. For highly reduced models, it was shown that the new bottleneck in simulation time is element evaluation. This motivates the inclusion of hyper-reduction methods, such as the discrete empirical interpolation method (DEIM) [35] or the energy conserving mesh sampling and weighting method (ECSW) [51], in future research. Due to the nonlinear structural finite element nature, ECSW is expected to perform better than DEIM for the cardiac problem. As the kinematics of a patient-specific heart can already be observed in motion MRI, it might be conceivable to incorporate this displacement information in the reduced space.

There exist many potential applications of MOR in cardiac many-query settings. One example is the task of obtaining a physiological periodic state, i.e. matching left and right ventricular output per cardiac cycle. In these scenarios, a cardiac simulation with constant parameters is run for multiple cycles, until the change from one cycle to the next is below a given tolerance. In [83] it was reported that in some cases more than ten cycles were necessary until converge to a periodic state. After simulating one FOM cycle and calculating the projection matrix, all preceding cycles could be run using a ROM since the shape of the cardiac contraction will be similar to the first cycle. In this use case, MOR can lead to drastic time savings, especially as the individual cardiac cycles cannot be run in parallel.

Four different methods of parametric model order reduction (pMOR) were further compared to allow ROM evaluations at parameter sets without prior FOM knowledge. The pMOR methods were evaluated by varying cardiac contractility, an important determinant of cardiac performance. The weighted concatenation of snapshots method was found to approximate the displacements of the FOM best for this example. Additionally, it was shown that the clinically important scalar cardiac quantities ejection fraction, maximum left ventricular pressure, and left atrioventricular plane displacement are also well approximated using pMOR. Next to model calibration and design exploration, a possible application of cardiac pMOR could be multi-fidelity uncertainty quantification [17].

5 Inverse analysis

Models of cardiac elasto-hemodynamics commonly depend on a large set of parameters, which need to be calibrated to patient-specific measurements using inverse analysis. This procedure is, however, computationally very expensive, as it requires many evaluations of the full order coupled structure-Windkessel model (2.75), which will be denoted forward model in the following. In this chapter, a novel approach for gradient-based inverse analysis is proposed, utilizing the parametric reduced order model (pROM) developed in Section 4.3.4. The full order model (FOM) forward evaluations typically required to obtain the gradient via finite differences is replaced by pROM forward evaluations (4.23). This method is illustrated using a simple Levenberg-Marquardt (LM) algorithm [120, 127] in Section 5.1. In Section 5.2, the proposed method's performance is demonstrated on a typical inverse analysis scenario using the cardiac forward problem introduced in Section 2.6. Concluding remarks are given in Section 5.3.

Parts of this chapter were submitted for publication in [147].

5.1 Parameter identification based on reduced models

Given m normalized model outputs $\mathbf{f}(\boldsymbol{\mu}) \in \mathbb{R}^m$ of a FOM depending on n_p normalized parameters $\boldsymbol{\mu} \in \mathbb{R}^{n_p}$ and $m \geq n_p$ normalized measurements \mathbf{y} the aim is to minimize the squared sum S of residuals \mathbf{r}

$$\hat{\boldsymbol{\mu}} = \underset{\boldsymbol{\mu}}{\operatorname{argmin}} S(\boldsymbol{\mu}), \quad (5.1)$$

$$\text{with } S(\boldsymbol{\mu}) = \frac{1}{2} \|\mathbf{r}(\boldsymbol{\mu})\|_2^2, \quad \mathbf{r}(\boldsymbol{\mu}) = \mathbf{y} - \text{FOM } \mathbf{f}(\boldsymbol{\mu}), \quad \mathbf{J}(\boldsymbol{\mu}) = \frac{\partial \mathbf{r}(\boldsymbol{\mu})}{\partial \boldsymbol{\mu}}$$

to obtain the optimal set of parameters $\hat{\boldsymbol{\mu}}$. The Jacobian of the residual vector with respect to the parameter vector is $\mathbf{J} \in \mathbb{R}^{m \times n_p}$. At the optimum $\hat{\boldsymbol{\mu}}$, the gradient $\nabla S = \mathbf{J}^T \mathbf{r} = \mathbf{0}$ vanishes and the Hessian $\nabla^2 S > \mathbf{0}$ is positive definite. Using the LM algorithm, yields the iterative procedure

$$\text{update } \boldsymbol{\mu}^{i+1} = \boldsymbol{\mu}^i + \Delta \boldsymbol{\mu}^{i+1} \quad (5.2)$$

$$\text{with } [\mathbf{J}^T \mathbf{J} + \lambda \operatorname{diag}(\mathbf{J}^T \mathbf{J})]^i \cdot \Delta \boldsymbol{\mu}^{i+1} = -[\mathbf{J}^T \mathbf{r}]^i, \quad (5.3)$$

$$\lambda^i = \lambda^{i-1} \cdot \frac{\|[\mathbf{J}^T \mathbf{r}]^i\|_2}{\|[\mathbf{J}^T \mathbf{r}]^{i-1}\|_2} \quad (5.4)$$

$$\text{until } \left\| [\mathbf{J}^T \mathbf{r}]^i \right\|_2 < \operatorname{tol}_{\text{grad}}^\mu \quad \text{and} \quad \left\| \Delta \boldsymbol{\mu}^{i+1} \right\|_2 < \operatorname{tol}_{\text{inc}}^\mu, \quad (5.5)$$

at iteration $i + 1$ with damping parameter λ . The LM algorithm approximates the Hessian as $\nabla^2 S \approx \mathbf{J}^T \mathbf{J}$. The damping parameter λ should tend to zero as the parameter set $\boldsymbol{\mu}$ approaches the optimal solution $\hat{\boldsymbol{\mu}}$. For $\lambda \rightarrow \infty$ the steepest descent method is approached, for $\lambda = 0$ the

Gauss-Newton method. In general, for a nonlinear model the analytical derivatives of the model evaluations \mathbf{f} with respect to the parameters $\boldsymbol{\mu}$ required for the Jacobian matrix are not easily available. The n_p columns \mathbf{J}_p^i of the Jacobian matrix \mathbf{J}^i are thus typically approximated by finite differences

$$\mathbf{J}_p^i \approx \pm \frac{\text{pROM } \mathbf{f}(\boldsymbol{\mu}_{\Delta p}^i) - \text{pROM } \mathbf{f}(\boldsymbol{\mu}^i)}{\epsilon_p}, \quad \text{with } \boldsymbol{\mu}_{\Delta p}^i = \boldsymbol{\mu}^i \pm \epsilon_p \mathbf{e}_p, \quad \forall p \in [1, \dots, n_p] \quad (5.6)$$

The gradient evaluation vector $\boldsymbol{\mu}_{\Delta p}^i$ is built from the p -th component ϵ_p of a finite distance vector $\boldsymbol{\epsilon} \in \mathbb{R}^p$ and the p -th unit vector $\mathbf{e}_p \in \mathbb{R}^p$ in the direction of each parameter. The sign in (5.6) is chosen for each parameter p so that the evaluation with parameter set $\boldsymbol{\mu}_{\Delta p}^i$ is within the range of all previously evaluated parameter sets.

Calculating the approximated Jacobian matrix requires $n_p + 1$ evaluations of the forward model which is computationally expensive in case of a large number of parameters n_p . The pROM introduced in Section 4.3.4 is very accurate for parameters in the proximity of the sampled parameter sets, as was shown in Section 4.3.4.1 for the cardiac contractility parameter σ_0 . As demonstrated in Section 4.3.4.2, using pMOR with two FOM sample points greatly improves the approximation of the tangent with respect to a changing contractility over using a single sample point. Therefore, it is proposed to use pROM evaluations of \mathbf{f} in (5.6) instead of FOM evaluations. The iterative procedure for the inverse analysis is sketched in Algorithm 2. Note that while using this approach, the algorithm still finds a local minimum of the objective function S in (5.1) with respect to the FOM.

Algorithm 2 Inverse analysis with pROM-gradient

- 1: initialize $\boldsymbol{\mu}^0, \lambda^0$
 - 2: $i = 0$
 - 3: **while** convergence criterion from (5.5) not fulfilled **do**
 - 4: evaluate FOM $\mathbf{f}(\boldsymbol{\mu}^i)$ and calculate residual \mathbf{r}^i from (5.1)
 - 5: store snapshots $\mathbf{D}(\boldsymbol{\mu}^i)$
 - 6: **for** $p = 0, \dots, n_p$ **do**
 - 7: build reduced basis $\mathbf{V}(\boldsymbol{\mu}_{\Delta p}^i)$ from (5.7)
 - 8: evaluate pROM $\mathbf{f}(\boldsymbol{\mu}_{\Delta p}^i)$
 - 9: **end for**
 - 10: calculate Jacobian \mathbf{J}^i from (5.6)
 - 11: update parameter vector $\boldsymbol{\mu}^{i+1}$ from (5.3)
 - 12: $i \leftarrow i + 1$
 - 13: **end while**
 - 14: **return** $\hat{\boldsymbol{\mu}} = \boldsymbol{\mu}^i$
-

Further note that the strategy introduced in Algorithm 2 requires in each iteration of the optimization that the FOM simulation is evaluated before the n_p gradients can be evaluated in parallel using the pROM simulations. Thus, considering a scenario of infinite available computing resources, this strategy would actually slightly increase computation time over the standard approach of using the FOM for all evaluations. Here, all $n_p + 1$ model evaluations can be run

in parallel. However, considering the more likely scenario where computing resources are just sufficient to calculate one or few FOM simulations at a time, the strategy outline in Algorithm 2 leads to considerable time savings especially for a large number of parameters n_p .

Algorithm 2 can be combined with any subspace interpolation method in step 7. The weighted concatenation of snapshots method (CoS) introduced in Section 4.2.2 is used here, as it performed best in the experiments in Section 4.3.4 and is easily applicable to multidimensional parameter sets. For the weights of the snapshot matrix for gradient evaluation p , a simple inverse distance weighting between two evaluation points is used

$$\begin{aligned} \tilde{\mathbf{D}}(\boldsymbol{\mu}_{\Delta p}^i) &= [w_1 \mathbf{D}(\boldsymbol{\mu}^i), w_2 \mathbf{D}(\boldsymbol{\mu}^k)], \quad w_1 = \frac{1/d_1}{1/d_1 + 1/d_2}, \quad w_2 = 1 - w_1, \\ d_1 &= \|\boldsymbol{\mu}_{\Delta p}^i - \boldsymbol{\mu}^i\|_2, \quad d_2 = \|\boldsymbol{\mu}_{\Delta p}^i - \boldsymbol{\mu}^k\|_2, \quad k = \underset{j \in [0, \dots, i-1]}{\operatorname{argmin}} \|\boldsymbol{\mu}_{\Delta p}^i - \boldsymbol{\mu}^j\|_2, \end{aligned} \quad (5.7)$$

with normalized distances d_1, d_2 and weights w_1, w_2 for the current evaluation i and the next closest evaluation k , respectively. Since at the beginning of the iteration $\epsilon_p \ll |\mu_p^i - \mu_p^k|$, the weight w_1 of the current snapshot matrix $\mathbf{D}(\boldsymbol{\mu}^i)$ is always close to one, whereas the weight w_2 is close to zero. This can be interpreted as "enriching" the snapshots of the current iteration with snapshots from a previous iteration to represent parametric dependence. As the optimization converges and the changes in parameters are close to the step size of the finite differences, the weights w_1 and w_2 equalize. For the first iteration of the optimization the algorithm relies on standard MOR evaluations using the constant projection matrix from the first FOM evaluation.

In the following, an equation is given for the speedup of gradient-based inverse analysis achieved by using pROM evaluations for the calculation of the Jacobian with respect to CPU time. Note that actual computation time depends on the parallelization of model evaluations. CPU time required to achieve convergence after n_i iterations is compared for a model with gradients calculated from pROM and FOM forward model evaluations, denoted by superscript pROM and FOM, respectively. The time spent during subspace generation is not included, as it is negligibly small compared to pROM and FOM evaluation time. The total CPU times T are

$$T^{\text{FOM}} = n_i^{\text{FOM}}(n_p + 1) T^{\text{FOM}}, \quad (5.8)$$

$$T^{\text{pROM}} = n_i^{\text{pROM}} [T^{\text{FOM}} + (n_p + 1) T^{\text{pROM}}], \quad (5.9)$$

where t is the time required for a single forward evaluation. It can be observed from (5.9) that the number of parameters only scales the pROM evaluation time but not the FOM evaluation time. Using the speedup α of a single pROM evaluation over a FOM evaluation, the total speedup β for the inverse problem with respect to CPU time is obtained as

$$\beta = \frac{T^{\text{FOM}}}{T^{\text{pROM}}} = \underbrace{\frac{n_i^{\text{FOM}}}{n_i^{\text{pROM}}}}_{\approx 1} \cdot \underbrace{\frac{1}{\frac{1}{\alpha} + \frac{1}{1+n_p}}}_{\rightarrow \alpha \text{ for } n_p \rightarrow \infty}, \quad \text{with } \alpha = \frac{T^{\text{FOM}}}{T^{\text{pROM}}}. \quad (5.10)$$

As will be shown in Section 5.2, the first factor is close to one as the number of iterations is comparable for both approaches when using a reasonably large number of reduced modes q . The second factor approaches α in the case of many parameters. Note that in practice there is a trade-off between the two factors. Choosing a very low-dimensional reduced model with

	σ_0 [kPa]	α_{\max} [$\frac{1}{s}$]	α_{\min} [$\frac{1}{s}$]	t_{sys} [S]	t_{dias} [S]
Initial	200	15	-15	0.35	0.60
Ground truth	280	10	-30	0.25	0.50

Table 5.1: Initial values and ground truth of estimated parameters during inverse analysis with $n_p = 5$.

few degrees of freedom q results in a high single call speedup α but may increase the number of iterations for the inverse analysis, as the tangents are now approximated worse than with a higher q . Further note that, after their respective number of iterations, both approximations achieve the same convergence criterion, which is always evaluated using the FOM.

Other variants of Algorithm 2 are feasible, e.g. replacing all FOM evaluations by pROM approximations as the inverse analysis algorithm converges closer to the optimum. Such algorithms however require more advanced strategies to switch between both model evaluations. The algorithm presented here demonstrates the most simple and straightforward approach of including a pROM within a finite difference gradient-based inverse analysis.

Remark Due to differences in the magnitude of the parameters' influence on cardiac dynamics, the distance-weighted interpolation proposed in (5.7) might not be the most robust choice. Here, as all parameters are treated equally, a very old iteration might be chosen for subspace interpolation. However, if the inverse analysis converges, the solutions of most recent iterations will always be closer to the current one. A more robust technique would thus be to simply use, for example, the last two iterations for subspace interpolation.

5.2 Numerical results and discussion

The ability of the inverse analysis method proposed in Section 5.1 to accurately and efficiently estimate parameters is demonstrated for a real-world cardiac estimation problem. Considered is the case of a cardiac simulation which is calibrated to a given volume curve, i.e. measurements of left ventricular volume over time during one cardiac cycle. The definition of the cardiac model is given in Section 4.3.1. No prior solutions of the FOM are available. Thus, the projection matrices need to be built from scratch starting at the first iteration of Algorithm 2.

The solution displayed in Figure 4.5a of a forward FOM simulation is chosen as the ground truth. As parameters, contractility σ_0 from (2.67) and myofiber activation rate α_{\max} , myofiber deactivation rate α_{\min} , onset of ventricular systole t_{sys} , and onset ventricular diastole t_{dias} from Section 2.4.3 are chosen. Thus, all parameters necessary to determine the shape of the input function of the model are estimated, i.e. the active stress over time $\tau(t)$. The parameters σ_0 , α_{\max} , and α_{\min} control cardiac output. However, due to their large variation they are commonly calibrated to a given patient [30]. These parameters are interconnected with the timing parameters t_{sys} and t_{dias} . The non-normalized parameters at the start of the inverse analysis and of the ground truth are listed in table 5.1. The damping parameter is initialized as $\lambda^0 = 0.1$. The number of reduced modes is further chosen as $q = 300$, as it offers a good trade-off between accuracy and speedup.

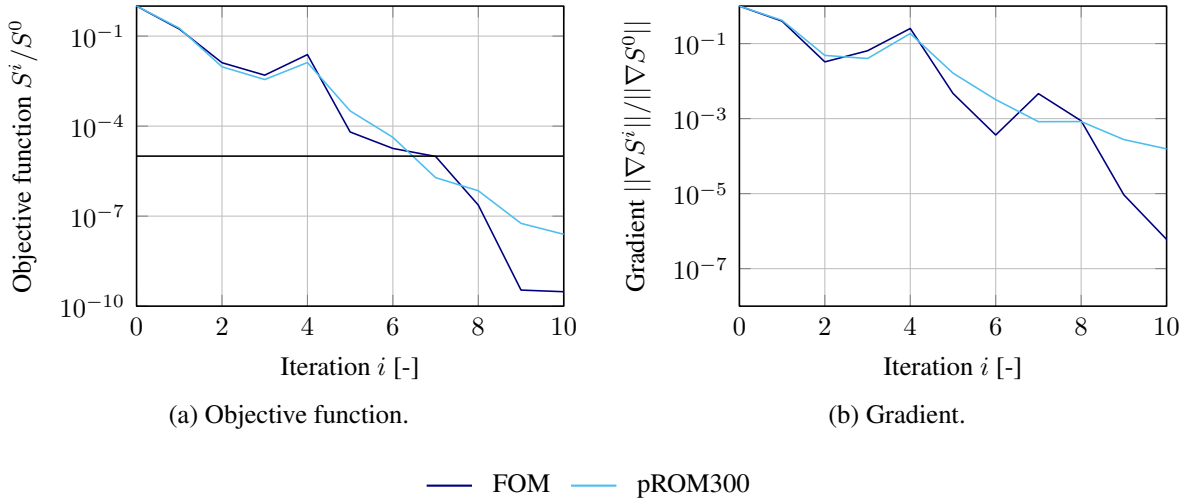


Figure 5.1: Convergence behavior during gradient-based inverse analysis with finite differences for gradient calculation. Shown are objective function and gradient for each iteration, comparing the use of FOM and pROM for gradient calculation.

In Figure 5.1 the performance of the pROM inverse analysis using Algorithm 2 is displayed, compared to the standard approach, where the gradients are evaluated using the FOM only. Figure 5.1a shows the decay of the objective function S from (5.1). As convergence criterion $S^i/S^0 < 10^{-5}$ is defined, which is achieved at $n_i^{\text{FOM}} = n_i^{\text{pROM}} = 7$. In Figure 5.1b the development of the gradient of the objective function with respect to the parameters is compared. As a synthetic case in the absence of noise is considered, both objective function and gradient should approach zero as $i \rightarrow \infty$. The fact that both measures are decreasing non-monotonically indicates a non-smooth optimization problem. However, the pROM300-gradient optimization is in excellent agreement with the FOM-gradient optimization.

The start, ground truth, and the converged solutions of both methods after seven iterations are shown in Figure 5.2. Here, the activation function, i.e. the input of the model, and the volume, i.e. the output of the model, are shown in figures 5.2a and 5.2b, respectively. It can be observed that both optimization methods match well with ground truth data for the given convergence criterion. The convergence of the five parameters relative to their initial values is shown in Figure 5.3 for both methods. Additionally, the iteration where the convergence criterion is achieved is indicated. Both methods show a similar trend towards the optimal parameters. With a single evaluation speedup of $\alpha \approx 7.1$, an overall speedup in CPU time of the pROM300 method over the FOM method of $\beta \approx 3.3$ is achieved, since $n_i^{\text{FOM}}/n_i^{\text{ROM}} = 1$ and $n_p = 5$ in the present case. simulations to evaluate the gradients reduces CPU time by 69% while achieving similar accuracy.

5.3 Conclusion

A novel method to include pROM into a finite difference gradient-based inverse analysis was introduced in this chapter. Using the Levenberg-Marquardt algorithm as an example, the use of

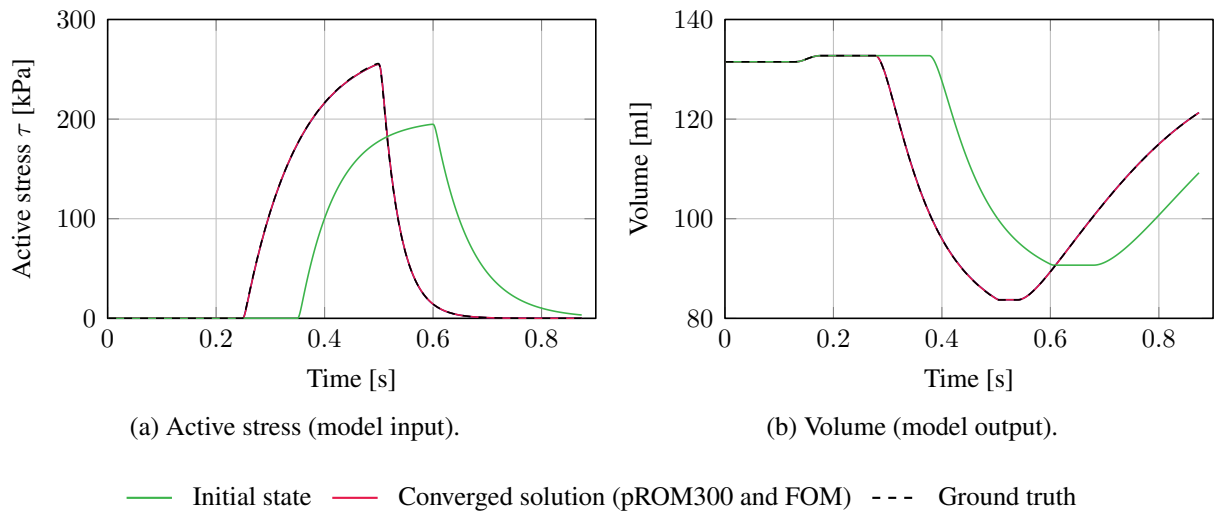
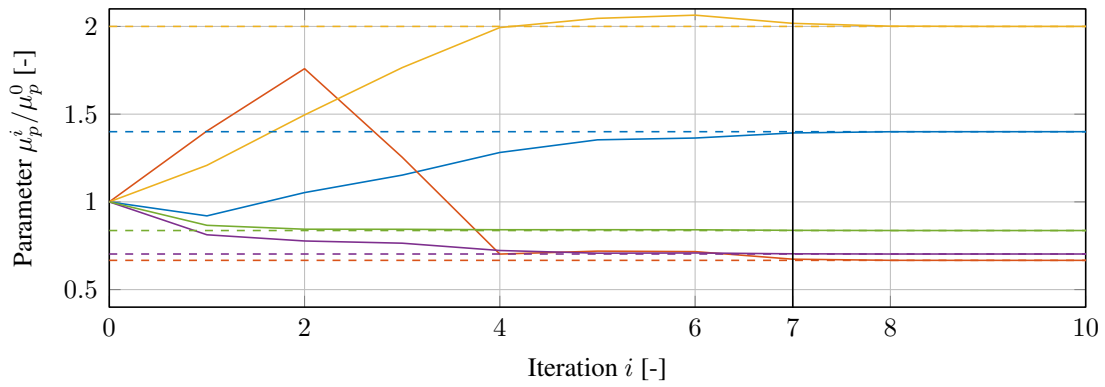


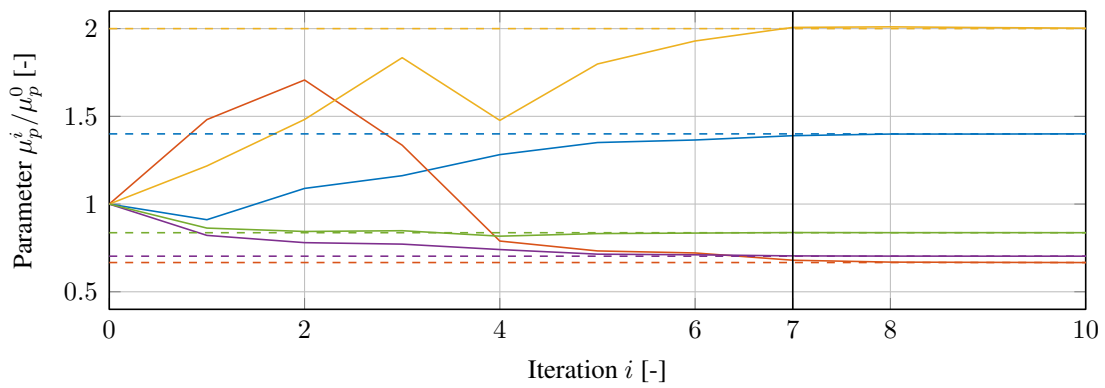
Figure 5.2: Initial state, converged solution, and ground truth of inverse analysis for model input (active stress) and model output (volume) over time.

the FOM for all objective function evaluations and pROM for all gradient evaluations was proposed, based on snapshots from the current and previous iterations. Using synthetic data in a real-world inverse analysis scenario, it was demonstrated that pROM-gradient-based optimization shows similar convergence properties as FOM-gradient-based optimization while achieving considerable CPU time savings. This method can be incorporated easily into existing optimization frameworks and could even be combined with commercial solvers for the structural problem. Using the inverse analysis approach proposed here, has the advantage that a full displacement field is still calculated in each evaluation of the forward model. Any spatial quantity can thus be evaluated, which is not possible when using 2D, 1D, or 0D surrogate models for the 3D structural model. In future research, this will allow to compute a spatial approximation error with respect to cine or tagged MRI to estimate patient-specific parameters from clinical observations. To the best of the author's knowledge, there is only one previous report about the application of parametric POD in the context of inverse problems in cardiac biomechanics. In [31], the parameter space was sampled with four parametric FOM solutions. These snapshots were concatenated to form a global POD basis. These modes were used to build a ROM of a cardiac biventricular model, where two contractility values were estimated using a Kalman filter approach. As the authors state themselves, the main issue with such an approach is that the number of (offline) FOM evaluations grows exponentially with the number of parameters. Although these evaluations can be run in parallel, this still might cause problems in practice since in real world problems the FOMs are already very large, i.e. one FOM already uses a large part of the available computational resources. Moreover, it is assumed that the parameter to be estimated is within the sampled parameter space.

It is the author's believe that the presented approach has the following advantages: (1) the number of FOM evaluations does not depend directly on the number of parameters but on the number of iterations in the optimization, which is usually independent on the number of parameters, and (2) there is no need to constrain the parameter space. It is noteworthy that at each optimization step



(a) FOM gradients.



(b) pROM300 gradients.

— σ — α_{\max} — α_{\min} — t_{sys} — t_{dias}

Figure 5.3: Convergence of parameters in inverse analysis. Dotted lines indicate ground truth of parameter.

higher order information of the least-squares functional (e.g. the Hessian) can be approximated using the POD modes at the same parameter, as it was done for the gradient. This should reduce the number of FOM evaluations to achieve a minimum. Furthermore, it is conceivable to replace some of the FOM evaluations of the objective function with pROM evaluations, depending on an error measure depicting the current quality of the pROM approximation.

6 Summary and Outlook

In this thesis, a computational mechanical model of the human heart was developed with the background to study post-infarction cardiac growth and remodeling (G&R) in the future. A patient-specific four-chamber geometry from high-resolution static 3D magnetic resonance imaging (MRI) was created, including ventricles, atria, adipose tissue, and great vessels. The cardiac model was formulated within a large displacement, constitutive nonlinear framework with nonlinear boundary conditions. It featured high-resolution quadratic tetrahedral finite elements for structural dynamics with implicit time integration. Blood pressure was incorporated through monolithic coupling of left and right ventricle to Windkessel models which include each the atrioventricular and semilunar valves. The reference configuration was prestressed in all four cardiac chambers. The passive myocardial material was composed of state of the art orthotropic exponential material law proposed in [88]. Myofiber contraction in atria and ventricles was modeled with an active stress approach. Passive and active material behavior were based on local fiber orientations.

Three objectives were addressed to improve the current state of cardiac mechanics modeling. Realistic and computationally cheap pericardial conditions were evaluated in a comprehensive study using patient-specific cine MRI data. A projection-based reduced order model of the monolithically coupled structural-Windkessel model was proposed as a general tool for speeding up model calibration, reducing the structural model using proper orthogonal decomposition. A strategy was suggested to use the reduced order model during gradient-based inverse analysis. The following sections provide an overview of the accomplishments of this thesis and of possible future directions of research.

Pericardial boundary conditions

The human heart is enclosed in the pericardial cavity. The pericardium consists of a layered thin sac and is separated from the myocardium by a thin film of fluid. It provides a fixture in space and frictionless sliding of the myocardium. Cardiac mechanics are formulated as an initial boundary value problem. A correct prediction of the kinematics of cardiac contraction as well as the internal stress state thus crucially depend on the boundary conditions. Accurate local stresses are essential, as they are an important trigger of cardiac G&R. Therefore, the influence of the pericardium is essential for predictive mechanical simulations of the heart. However, so far there is no consensus on physiologically exact but computationally tractable pericardial boundary conditions.

Following a comprehensive review of the biological details of the pericardium, a mechanical model is proposed for myocardial-pericardial interaction. A simplified boundary condition was derived leading to the formulation of a parallel spring and dashpot acting in normal direction on the epicardium. Using a four-chamber geometry, a model with pericardial boundary conditions was compared to a model with a fixed apex, a boundary condition commonly used in literature.

The influence on pericardial stiffness on cardiac contraction was studied in a parametric study. Ventricular dynamics were well approximated for low stiffness values, whereas ventricular-atrial interaction was best approximated for higher stiffness values.

In a second numerical study, simulation results for both boundary conditions were compared to measurements from cine magnetic resonance imaging. To incorporate the influence of fiber orientation in cardiac contraction, three different orientations, $\pm 50^\circ$, $\pm 60^\circ$, and $\pm 70^\circ$, were studied. For each combination of boundary condition and fiber orientation, cardiac contractility and onset of systole were calibrated to the left ventricular volume curve obtained from cine MRI. Simulations were compared with respect to left ventricular volume and pressure, atrioventricular plane displacement, ventricular endocardial spatial error, passive atrial filling, and pericardial contact-stress. Using pericardial boundary conditions yielded a better approximation with respect to atrioventricular plane displacement, atrial filling, and overall spatial approximation error. In general, more vertical fiber orientations yielded higher atrioventricular plane displacement, whereas more horizontal fiber orientations yield a more radial contraction of the ventricles. Most importantly, the stresses acting on the pericardium were unphysiologically high in case of a fixed apex. For pericardial boundary conditions, stresses were distributed evenly over the epicardial surface and on average within the range ± 20 mmHg.

In general, this thesis demonstrated that a simple model of pericardial-myocardial interaction can correctly predict the pumping mechanisms of the heart as previously assessed in clinical studies. To make a fair judgment of pericardial boundary conditions, they were compared to a cardiac model with a fixed apex, representing the state of the art of simplified epicardial boundary conditions. The cardiac model with pericardial boundary conditions predicted cardiac motion in better agreement with cine MRI of tested characteristics of cardiac contraction. It further yielded physiologically more correct contact stresses, which were highly elevated when using boundary conditions with a fixed apex. Especially the second finding is important for future studies of cardiac G&R. In the future, utilizing a pericardial model can not only provide much more realistic cardiac mechanics simulations but also allows new insights into pericardial-myocardial interaction which cannot be assessed in clinical measurements yet.

A major improvement of pericardial boundary conditions is given by spatially varying pericardial stiffness parameters. A finding in this thesis was that different regions of the heart are well approximated for different stiffness parameters. This suggests that the model might benefit from a regional variation of pericardial stiffness. This hypothesis is supported by the fact that the pericardial tissue is in contact with various organs of different material properties. As the pericardium transmits forces between the heart and its surrounding organs, the organs' stiffness is expected to influence cardiac contraction.

The simulation results in this thesis were solely compared to cine MRI data. Cine MRI is an Eulerian observation of cardiac movement, as imaging is fixed in space throughout the cardiac cycle. This observation, however, cannot detect any rotational movement with respect to the long axis, as the left ventricle is almost rotationally symmetric. To properly validate any rotational movement of the myocardium, a comparison to data from 3D tagged MRI is necessary, which is a Lagrangian observation of cardiac motion.

To validate the stresses acting on the epicardium during cardiac contraction predicted by the pericardial boundary condition, experiments are necessary. Pericardial contact stress can be measured by a flat balloon catheter. However, previous clinical studies did either only consider end-diastolic stresses [165, 177] or measured pericardial liquid pressure instead of contact pressure

[85]. For a comprehensive analysis, *in vivo* measurements of pericardial contract stress must be performed at different regions of the epicardial surface throughout the whole cardiac cycle.

Model order reduction

Predictive high-fidelity finite element simulations of human cardiac mechanics commonly require a large number of structural degrees of freedom. Additionally, these models are often coupled with lumped-parameter models of hemodynamics. High computational demands, however, slow down model calibration and therefore limit the use of cardiac simulations in clinical practice. As cardiac models rely on several patient-specific parameters, just one solution corresponding to one specific parameter set does not at all meet clinical demands. Moreover, while solving the nonlinear problem, 90% of the computation time is spent solving linear systems of equations. This motivates the use of projection-based model order reduction.

In this thesis, a novel approach was derived to reduce only the structural model of the monolithically coupled structure-Windkessel system by projection onto a lower-dimensional subspace. The Windkessel model remains unchanged during the reduction. Proper orthogonal decomposition was used to obtain a projection matrix, based on a solution of one cardiac cycle of the full order model. Several methods were reviewed for subspace interpolation to incorporate parametric variations into the reduced order model and enable its solution of parametric simulations without prior knowledge of the full order solution.

The performance of all proposed methods was demonstrated using a high-fidelity patient-specific four-chamber cardiac model with about 850'000 degrees of freedom. In the most extreme case, a reduced order model with only ten degrees of freedom yielded an approximation accuracy below 0.2 mm while achieving a speedup of a factor of 13 over the full order model. Cardiac contractility was varied and simulations were compared to test different subspace interpolation methods for different resolutions of full order model sample points. Although reduced order model approximation accuracy decreases significantly in between sample points, the subspace interpolation methods successfully incorporated parametric changes, obtaining a good approximation of the displacement field as well as of key scalar cardiac outputs.

It was found for reduced order models with very few degrees of freedom that element evaluation dominates total simulation time. In the future, these reduced order models could thus be further sped up by introducing hyper-reduction. Such methods have already been proposed, see, e.g. the discrete empirical interpolation method (DEIM) [35] or the energy conserving mesh sampling and weighting method (ECSW) [51]. However, the stability of those methods within the monolithically coupled structure-Windkessel model is yet unknown.

Projection-based reduced order modeling has some interesting applications in cardiac mechanics, especially in a many-query setting, where many model outputs are required. It was reported in [83] that more than ten cycles can be necessary until a closed-loop cardiovascular model converges to a periodic state. In multifidelity uncertainty quantification, repeated model evaluations are required while switching between models of varying fidelity [17]. Furthermore, repeated cycling over an extended period of time might be necessary to trigger laws of cardiac G&R. In all scenarios, some of the cardiac cycles could potentially be replaced by reduced order models in the future.

Inverse analysis

It was shown that projection-based model order reduction can be easily integrated into a gradient-based optimization when using finite differences to calculate the gradient. The method proposed in this thesis uses the full order model to evaluate the objective function and reduced order models to evaluate gradients, based on solutions of the full order model in the current and prior iterations of the optimization. This simple approach can be easily integrated in existing optimization frameworks and could even be compatible with commercial solvers for the forward model.

The performance was demonstrated in a real-world multivariate inverse analysis scenario with the Levenberg-Marquardt method, using a volume curve as model output and the active stress curve as model input. Using the presented projection-based model order reduction approach yielded convergence properties competitive with the standard approach. Using a reduced order model with 300 degrees of freedom and a speedup of a factor of 7.1 compared to the full order model yielded an optimization speedup of a factor of 3.3.

The proposed method could be further improved by embedding it within a tailored optimization method, benefiting from cheap gradient evaluations. With a suitable algorithm to estimate the required accuracy of an iteration of the optimization, even some of the objective function evaluations could be sped up by reduced order models. The accuracy of the reduced order models, in this case easily adapted by the number of reduced degrees of freedom, could be chosen dynamically, depending on the purpose of the model evaluation, i.e. objective function, gradient, or second derivative.

The scenario where parameters are estimated for a cardiac model from 3D tagged MRI is a special case in model order reduction, since the optimal displacements of the model are known *a priori*. It might thus be conceivable to extract displacement modes from the MRI observation. The subspaces used within the optimization algorithm could then be enriched by the ones from MRI. As the optimization converges towards the optimal parameter set, the modes obtained from MRI assure a good approximation of the reduced order model close to the optimum.

Modeling of cardiac growth and remodeling

It was hypothesized at the beginning of this thesis that adverse cardiac G&R following myocardial infarction (MI) results from an imbalance of several competing adaption mechanisms, namely hypertrophy, extracellular matrix remodeling, and myofiber reorientation. To test this hypothesis, knowledge of the evolution of the mechanical state of the myocardium, i.e., local stress, stiffness, and microstructure, needs to be obtained at multiple points in time during healing from MI.

The mechanical state of the myocardium cannot be assessed *in vivo* by routine clinical examination. Nevertheless, it can be estimated using an advanced cardiac computational model as developed in this thesis. All cardiac models crucially rely on active and passive constitutive properties of the myocardium, as well as local tissue anisotropy resulting from myocardial microstructure. Cardiac material parameters have been estimated in the past from motion MRI or ultrasound through inverse analysis [30, 52, 77, 129, 135, 144]. However, none of the findings obtained from computational modeling was compared to *ex vivo* mechanical testing for valida-

tion. Furthermore, it is expected that the regional constitutive properties of myocardial tissue following remodeling are significantly altered compared to the healthy state [76].

There have been attempts to quantify *in vivo* mechanical changes in cardiac tissue undergoing G&R. Based on the theory of kinematic growth [153], models for eccentric (strain-driven) and concentric (stress-driven) hypertrophy have been proposed [72, 107, 187]. The kinematic growth theory is, however, unable to differentiate between constituents of myocardial tissue, i.e., myocytes, collagen fibers, and ground matrix, which all might have different G&R mechanisms and triggers. Furthermore, kinematic growth models often grow unboundedly unless they are restrained *a priori*. These models are thus not suitable for predicting the stability of a heart's adaption processes. Constrained mixture models of G&R model the continuous deposition and degradation of different constituents of biological tissue, taking into account their individual preferred homeostatic stress state [93]. Recently, a homogenized constrained mixture theory was developed and applied to aneurysms, combining the microstructural detail of constrained mixture models with computational efficiency [25, 42]. Although past computational studies of cardiac G&R were able to confirm trends observed in previous *ex vivo* experiments [62, 73, 101, 103, 117, 118], the quantitative results of these studies are limited.

The central aspect of future research of cardiac G&R should therefore be a longitudinal experimental and computational study of cardiac regeneration. Animals induced with MI could be monitored using a comprehensive *in vivo* measuring protocol, including 3D static MRI, cine MRI, 3D tagged MRI, diffusion tensor MRI, and catheter pressure measurements at multiple points in time throughout the adaption process. Inverse finite element simulations of the contracting heart could be employed to obtain *in vivo* spatially distributed constitutive parameters. The changes in fiber architecture could be quantified through a reconstruction from *in vivo* diffusion tensor MRI. This study protocol would allow to completely characterize the change in mechanical properties of healing myocardial tissue over time. At the end point of the longitudinal *in vivo* study, the hearts could be excised and undergo *ex vivo* triaxial shear and biaxial tensile testing. Mechanical testing would enable the comparison of constitutive parameters obtained from inverse finite element simulations of the contracting heart with parameters from *ex vivo* measurements. Based on these accurate models of the hearts' mechanical state at several points in time, homogenized constrained mixture models could be calibrated to identify triggers of cardiac G&R.

A physiological patient-specific predictive computational model of cardiac G&R will be extremely beneficial for patients in many scenarios, e.g., to determine *a priori* whether a patient is likely to respond to a specific therapy and for optimizing treatments on a patient-specific basis to maximize post-MI recovery. For example, the optimal pacing site in cardiac resynchronization therapy could be selected as predicted by a computational model to maximize *long-term* cardiac rehabilitation, rather than maximizing *short-term* response according to currently available clinical predictors.

A Simulation parameters

All parameters for all simulations in this work are summarized in this appendix.

A.1 Pericardial boundary conditions: Prolate spheroid geometry

These parameters are used in Section 3.4 for the prolate spheroid geometry from Section 2.3.2.

Name	Parameter	Value	Unit
Tissue density	ρ_0	10^3	$\left[\frac{\text{kg}}{\text{m}^3}\right]$
Viscosity	η	10.0	[Pa · s]
Volumetric penalty	κ	10^4	[kPa]
Ventricular contractility	σ_v	185	[kPa]
Mooney-Rivlin	C_1	10.0	[kPa]
	C_2	40.0	[Pa]
Spring stiffness base	k_b	1.0	$\left[\frac{\text{kPa}}{\text{mm}}\right]$
Dashpot viscosity base	c_b	0.0	$\left[\frac{\text{kPa}\cdot\text{s}}{\text{mm}}\right]$
<i>Pericardial spring stiffness</i>			
Case <i>free</i>	k_p	0.0	$\left[\frac{\text{kPa}}{\text{mm}}\right]$
Case <i>pericardium</i>	k_p	20.0	$\left[\frac{\text{kPa}}{\text{mm}}\right]$
Case <i>pseudo-contact</i>	k_p	20.0	$\left[\frac{\text{kPa}}{\text{mm}}\right]$
All cases	c_p	0.0	$\left[\frac{\text{kPa}\cdot\text{s}}{\text{mm}}\right]$

Table A.1: Parameters of the elastodynamical model.

Name	Parameter	Value	Unit
Proximal inertance	L_p	$1.3 \cdot 10^5$	$\left[\frac{\text{kg}}{\text{m}^4}\right]$
Proximal capacity	C_p	$7.7 \cdot 10^{-9}$	$\left[\frac{\text{m}^4 \cdot \text{s}^2}{\text{kg}}\right]$
Distal capacity	C_d	$8.7 \cdot 10^{-9}$	$\left[\frac{\text{m}^4 \cdot \text{s}^2}{\text{kg}}\right]$
Proximal resistance	R_p	$7.3 \cdot 10^6$	$\left[\frac{\text{kg}}{\text{m}^4 \cdot \text{s}}\right]$
Distal resistance	R_d	$1.0 \cdot 10^8$	$\left[\frac{\text{kg}}{\text{m}^4 \cdot \text{s}}\right]$
Reference pressure	p_{ref}	0	[Pa]
Closed valve resistance	R_{max}	$1.0 \cdot 10^{13}$	$\left[\frac{\text{kg}}{\text{m}^4 \cdot \text{s}}\right]$
Open valve resistance	R_{min}	$1.0 \cdot 10^6$	$\left[\frac{\text{kg}}{\text{m}^4 \cdot \text{s}}\right]$
Valve steepness	k_p	$1.0 \cdot 10^{-3}$	[Pa]

Table A.2: Parameters of the cardiovascular Windkessel model.

Name	Parameter	Value	Unit
Atrial pressure	$p_{\text{at}}(0)$	0.0	[mmHg]
Ventricular pressure	$p_{\text{v}}(0)$	0.0	[mmHg]
Proximal pressure	$p_p(0)$	80.0	[mmHg]
Distal pressure	$p_d(0)$	72.3	[mmHg]
Proximal flow	$q_p(0)$	97.4	$\left[\frac{\text{cm}^3}{\text{s}}\right]$

Table A.3: Initial conditions of the reduced order cardiovascular model.

Parameter	Value
<i>Generalized-α</i>	
$\gamma, \alpha_f, \alpha_m$	0.5
β	0.25
<i>One-step-θ</i>	
θ	1.0

Table A.4: Numerical time integration parameters.

A.2 Pericardial boundary conditions: Patient-specific four-chamber geometry

These parameters are used in Section 3.5 for the patient-specific four-chamber geometry from Section 2.3.1. The parameters for the left and right ventricular Windkessel model are identical to the ones in Table A.2. The numerical time integration parameters are identical to the ones in A.4.

Name	Parameter	Value	Unit
<i>All tissues</i>			
Tissue density	ρ_0	10^3	$\left[\frac{\text{kg}}{\text{m}^3}\right]$
Viscosity	η	0.1	[kPa · s]
Volumetric penalty	κ	10^3	[kPa]
<i>Active myocardial tissue</i>			
Atrial contractility	σ_a	9.72	kPa
Ventricular contractility	σ_v	see Table 3.1b	
Activation rate	α_{\max}	+5	$\left[\frac{1}{\text{s}}\right]$
Deactivation rate	α_{\min}	-30	$\left[\frac{1}{\text{s}}\right]$
Atrial systole	t_{sys}	70	[ms]
Atrial diastole	t_{dias}	140	[ms]
Ventricular systole	t_{sys}	see Table 3.1b	
Ventricular diastole	t_{dias}	484	[ms]
<i>Passive myocardial tissue ([88] table 1, shear, figure 7)</i>			
Matrix	a	0.059	[kPa]
	b	8.023	[-]
Fiber	a_f	18.472	[kPa]
	b_f	16.026	[-]
Sheet	a_s	2.481	[kPa]
	b_s	11.120	[-]
Fiber-sheet	a_{fs}	0.216	[kPa]
	b_{fs}	11.436	[-]

Table A.5 – Continued from previous page

Name	Parameter	Value	Unit
<i>Great vessels</i>			
Mooney-Rivlin	C_1	5.0	[kPa]
	C_2	0.04	[kPa]
Spring stiffness	k_v	$2.0 \cdot 10^3$	$\left[\frac{\text{kPa}}{\text{mm}}\right]$
Dashpot viscosity	c_v	$1.0 \cdot 10^{-2}$	$\left[\frac{\text{kPa}\cdot\text{s}}{\text{mm}}\right]$
<i>Adipose tissue</i>			
Neo-Hooke	μ	1.0	[kPa]
<i>Pericardial boundary condition:</i> see Table 3.1a			

Table A.5: Parameters of the elastodynamical model.

Name	Parameter	Value		Unit
		Left	Right	
Atrial pressure	$p_{\text{at}}(0)$	6.0	4.0	[mmHg]
Ventricular pressure	$p_v(0)$	8.0	6.0	[mmHg]
Proximal pressure	$p_p(0)$	61.8	24.0	[mmHg]
Distal pressure	$p_d(0)$	59.7	23.2	[mmHg]
Proximal flow	$q_p(0)$	38.3	14.9	$\left[\frac{\text{cm}^3}{\text{s}}\right]$

Table A.6: Initial conditions of the reduced order cardiovascular model.

A.3 Model order reduction: Patient-specific four-chamber geometry

These parameters are used in Chapters 4 and 5 for the patient-specific four-chamber geometry from Section 2.3.1. The parameters for the left and right ventricular Windkessel model are identical to the ones in Table A.2. The numerical time integration parameters are identical to the ones in A.4.

A.3 Model order reduction: Patient-specific four-chamber geometry

Name	Parameter	Value	Unit
<i>All tissues</i>			
Tissue density	ρ_0	10^3	$\left[\frac{\text{kg}}{\text{m}^3}\right]$
Viscosity	η	5.0	$[\text{kPa} \cdot \text{s}]$
Volumetric penalty	κ	10^4	$[\text{kPa}]$
<i>Active myocardial tissue</i>			
Ventricular contractility	σ_0	[280, ... ,430]	kPa
Activation rate	α_{\max}	+10	$\left[\frac{1}{\text{s}}\right]$
Deactivation rate	α_{\min}	-30	$\left[\frac{1}{\text{s}}\right]$
Ventricular systole	t_{sys}	246	[ms]
Ventricular diastole	t_{dias}	502	[ms]
<i>Passive myocardial tissue and great vessels</i>			
Mooney-Rivlin	C_1	10.0	[kPa]
	C_2	40.0	[Pa]
Spring stiffness	k_v	$2.0 \cdot 10^3$	$\left[\frac{\text{kPa}}{\text{mm}}\right]$
Dashpot viscosity	c_v	$1.0 \cdot 10^{-2}$	$\left[\frac{\text{kPa} \cdot \text{s}}{\text{mm}}\right]$
<i>Adipose tissue</i>			
Neo-Hooke	μ	1.0	[kPa]
<i>Pericardial boundary condition:</i> see Table 3.1a			

Table A.7: Parameters of the elastodynamical model.

Bibliography

- [1] R. J. Allemang, The modal assurance criterion—twenty years of use and abuse, *Sound and Vibration* **37**, 14–23, 2003.
- [2] R. J. Allemang and D. L. Brown, A correlation coefficient for modal vector analysis, *Proceedings of the 1st International Modal Analysis Conference* **1**, 110–116, 1982.
- [3] D. Ambrosi and S. Pezzuto, Active stress vs. active strain in mechanobiology: Constitutive issues, *Journal of Elasticity* **107**, 199–212, 2012.
- [4] D. Amsallem and C. Farhat, Interpolation method for adapting reduced-order models and application to aeroelasticity, *AIAA Journal* **46**, 1803–1813, 2008.
- [5] T. Arts, R. S. Reneman, and P. C. Veenstra, A model of the mechanics of the left ventricle, *Annals of Biomedical Engineering* **7**, 299–318, 1979.
- [6] A. H. Arutunyan, Atrioventricular plane displacement is the sole mechanism of atrial and ventricular refill, *American Journal of Physiology-Heart and Circulatory Physiology* **308**, H1317–H1320, 2015.
- [7] P. M. Arvidsson, M. Carlsson, S. J. Kovacs, and H. Arheden, Letter to the editor: Atrioventricular plane displacement is not the sole mechanism of atrial and ventricular refill, *American Journal of Physiology-Heart and Circulatory Physiology* **309**, H1094–H1096, 2015.
- [8] H. Ashikaga et al., Feasibility of image-based simulation to estimate ablation target in human ventricular arrhythmia, *Heart Rhythm* **10**, 1109–1116, 2013.
- [9] L. Asner, M. Hadjicharalambous, R. Chabiniok, D. Peresutti, E. Sammut, J. Wong, G. Carr-White, P. Chowienczyk, J. Lee, A. King, N. Smith, R. Razavi, and D. Nordsletten, Estimation of passive and active properties in the human heart using 3D tagged MRI, *Biomechanics and Modeling in Mechanobiology*, 1–19, 2015.
- [10] C. M. Augustin, A. Neic, M. Liebmann, A. J. Prassl, S. A. Niederer, G. Haase, and G. Plank, Anatomically accurate high resolution modeling of human whole heart electromechanics: A strongly scalable algebraic multigrid solver method for nonlinear deformation, *Journal of Computational Physics* **305**, 622–646, 2016.
- [11] B. Baillargeon, N. Rebelo, D. D. Fox, R. L. Taylor, and E. Kuhl, The living heart project: A robust and integrative simulator for human heart function, *European Journal of Mechanics—A/Solids* **48**, 38–47, 2014.

- [12] F. Ballarin, E. Faggiano, A. Manzoni, A. Quarteroni, G. Rozza, S. Ippolito, C. Antona, and R. Scrofani, Numerical modeling of hemodynamics scenarios of patient-specific coronary artery bypass grafts, *Biomechanics and Modeling in Mechanobiology* **16**, 1373–1399, 2017.
- [13] C. A. Beltrami, N. Finato, M. Rocco, G. A. Feruglio, C. Puricelli, E. Cigola, F. Quaini, E. H. Sonnenblick, G. Olivetti, and P. Anversa, Structural basis of end-stage failure in ischemic cardiomyopathy in humans, *Circulation* **89**, 151–63, 1994.
- [14] P. Benner, S. Gugercin, and K. Willcox, A survey of projection-based model reduction methods for parametric dynamical systems, *SIAM Review* **57**, 483–531, 2015.
- [15] C. Bertoglio, P. Moireau, and J.-F. Gerbeau, Sequential parameter estimation for fluid-structure problems: Application to hemodynamics, *International Journal for Numerical Methods in Biomedical Engineering* **28**, 434–455, 2012.
- [16] J. Bestel, F. Clément, and M. Sorine, A biomechanical model of muscle contraction, In *Medical Image Computing and Computer-Assisted Intervention–MICCAI 2001*, pages 1159–1161. Springer, 2001.
- [17] J. Biehler, M. W. Gee, and W. A. Wall, Towards efficient uncertainty quantification in complex and large-scale biomechanical problems based on a bayesian multi-fidelity scheme, *Biomechanics and Modeling in Mechanobiology* **14**, 489–513, 2015.
- [18] E. J. Birks, P. D. Tansley, J. Hardy, R. S. George, C. T. Bowles, M. Burke, N. R. Banner, A. Khaghani, and M. H. Yacoub, Left ventricular assist device and drug therapy for the reversal of heart failure, *New England Journal of Medicine* **355**, 1873–1884, 2006.
- [19] J. Bonet, *Nonlinear continuum mechanics for finite element analysis*, Cambridge university press, 2008.
- [20] D. Bonomi, A. Manzoni, and A. Quarteroni, A matrix DEIM technique for model reduction of nonlinear parametrized problems in cardiac mechanics, *Computer Methods in Applied Mechanics and Engineering* **324**, 300–326, 2017.
- [21] D. Bonomi, A. Manzoni, and A. Quarteroni, A matrix deim technique for model reduction of nonlinear parametrized problems in cardiac mechanics, *Computer Methods in Applied Mechanics and Engineering* **324**, 300–326, 2017.
- [22] M. Boulakia, E. Schenone, and J.-F. Gerbeau, Reduced-order modeling for cardiac electrophysiology. application to parameter identification, *International Journal for Numerical Methods in Biomedical Engineering* **28**, 727–744, 2012.
- [23] P. H. Bovendeerd, Modeling of cardiac growth and remodeling of myofiber orientation, *Journal of Biomechanics* **45**, 872–881, 2012.
- [24] A. W. Bowman and S. J. Kovcs, Assessment and consequences of the constant-volume attribute of the four-chambered heart, *American Journal of Physiology-Heart and Circulatory Physiology* **285**, H2027–H2033, 2003.

-
- [25] F. A. Bräu, A. Seitz, R. C. Aydin, and C. J. Cyron, Homogenized constrained mixture models for anisotropic volumetric growth and remodeling, *Biomechanics and Modeling in Mechanobiology*, 2016.
- [26] J. S. Burchfield, M. Xie, and J. A. Hill, Pathological ventricular remodeling: Mechanisms: Part 1 of 2, *Circulation* **128**, 388–400, 2013.
- [27] B. Cansız, H. Dal, and M. Kaliske, Computational cardiology: A modified hill model to describe the electro-visco-elasticity of the myocardium, *Computer Methods in Applied Mechanics and Engineering* **315**, 434–466, 2017.
- [28] M. Carlsson, M. Ugander, H. Mosén, T. Buhre, and H. Arheden, Atrioventricular plane displacement is the major contributor to left ventricular pumping in healthy adults, athletes, and patients with dilated cardiomyopathy, *American Journal of Physiology–Heart and Circulatory Physiology* **292**, H1452–H1459, 2007.
- [29] M. Caruel, R. Chabiniok, P. Moireau, Y. Lecarpentier, and D. Chapelle, Dimensional reductions of a cardiac model for effective validation and calibration, *Biomechanics and Modeling in Mechanobiology* **13**, 897–914, 2014.
- [30] R. Chabiniok, P. Moireau, P.-F. Lesault, A. Rahmouni, J.-F. Deux, and D. Chapelle, Estimation of tissue contractility from cardiac cine-MRI using a biomechanical heart model, *Biomechanics and Modeling in Mechanobiology* **11**, 609–630, 2012.
- [31] D. Chapelle, A. Gariah, P. Moireau, and J. Sainte-Marie, A Galerkin strategy with proper orthogonal decomposition for parameter-dependent problems – analysis, assessments and applications to parameter estimation, *ESAIM: Mathematical Modelling and Numerical Analysis* **47**, 18211843, 2013.
- [32] D. Chapelle, P. Le Tallec, P. Moireau, and M. Sorine, An energy-preserving muscle tissue model: formulation and compatible discretizations, *International Journal for Multiscale Computational Engineering* **10**, 189–211, 2012.
- [33] P. Chareonthaitawee, T. F. Christian, K. Hirose, R. J. Gibbons, and J. A. Rumberger, Relation of initial infarct size to extent of left ventricular remodeling in the year after acute myocardial infarction, *Journal of the American College of Cardiology* **25**, 567–573, 1995.
- [34] A. Chatterjee, An introduction to the proper orthogonal decomposition, *Current Science*, 808–817, 2000.
- [35] S. Chaturantabut and D. C. Sorensen, Nonlinear model reduction via discrete empirical interpolation, *SIAM Journal on Scientific Computing* **32**, 2737–2764, 2010.
- [36] C. E. Chávez, N. Zemzemi, Y. Coudière, F. Alonso-Atienza, and D. Álvarez, Inverse problem of electrocardiography: Estimating the location of cardiac ischemia in a 3D realistic geometry, In H. van Assen, P. Bovendeerd, and T. Delhaas (eds.), *Functional Imaging and Modeling of the Heart*, pages 393–401, Cham, 2015, Springer International Publishing.

- [37] J. Chen, S.-K. Song, W. Liu, M. McLean, J. S. Allen, J. Tan, S. A. Wickline, and X. Yu, Remodeling of cardiac fiber structure after infarction in rats quantified with diffusion tensor MRI, *American Journal of Physiology–Heart and Circulatory Physiology* **285**, H946–H954, 2003.
- [38] J. Chung and G. Hulbert, A time integration algorithm for structural dynamics with improved numerical dissipation: the generalized- α method, *Journal of Applied Mechanics* **60**, 371–375, 1993.
- [39] M. V. Cohen, X.-M. Yang, T. Neumann, G. Heusch, and J. M. Downey, Favorable remodeling enhances recovery of regional myocardial function in the weeks after infarction in ischemically preconditioned hearts, *Circulation* **102**, 579–583, 2000.
- [40] J. N. Cohn, R. Ferrari, and N. Sharpe, Cardiac remodeling – concepts and clinical implications: a consensus paper from an international forum on cardiac remodeling, *Journal of the American College of Cardiology* **35**, 569–582, 2000.
- [41] C. Corrado, J.-F. Gerbeau, and P. Moireau, Identification of weakly coupled multiphysics problems. application to the inverse problem of electrocardiography, *Journal of Computational Physics* **283**, 271–298, 2015.
- [42] C. J. Cyron, R. C. Aydin, and J. D. Humphrey, A homogenized constrained mixture (and mechanical analog) model for growth and remodeling of soft tissue, *Biomechanics and Modeling in Mechanobiology* **15**, 1389–1403, 2016.
- [43] E. P. Daskalopoulos, B. J. Janssen, and W. M. Blankesteyn, Myofibroblasts in the infarct area: concepts and challenges, *Microscopy and Microanalysis* **18**, 35–49, 2012.
- [44] L. L. Demer and F. C. Yin, Passive biaxial mechanical properties of isolated canine myocardium., *The Journal of Physiology* **339**, 615–630, 1983.
- [45] S. Dokos, B. H. Smaill, A. A. Young, and I. J. LeGrice, Shear properties of passive ventricular myocardium, *American Journal of Physiology–Heart and Circulatory Physiology* **283**, H2650–H2659, 2002.
- [46] S. N. Doost, D. Ghista, B. Su, L. Zhong, and Y. S. Morsi, Heart blood flow simulation: a perspective review, *BioMedical Engineering OnLine* **15**, 101, 2016.
- [47] K. Emilsson, L. Brudin, and B. Wandt, The mode of left ventricular pumping: is there an outer contour change in addition to the atrioventricular plane displacement?, *Clinical Physiology* **21**, 437–446, 2001.
- [48] T. S. E. Eriksson, A. J. Prassl, G. Plank, and G. A. Holzapfel, Modeling the dispersion in electromechanically coupled myocardium, *International Journal for Numerical Methods in Biomedical Engineering* **29**, 1267–1284, 2013.
- [49] T. Eriksson, A. Prassl, G. Plank, and G. Holzapfel, Influence of myocardial fiber/sheet orientations on left ventricular mechanical contraction, *Mathematics and Mechanics of Solids*, 2013.

- [50] P. W. Farah, *Mortar Methods for Computational Contact Mechanics Including Wear and General Volume Coupled Problems*, Dissertation, Technical University of Munich, 2018.
- [51] C. Farhat, T. Chapman, and P. Avery, Structure-preserving, stability, and accuracy properties of the energy-conserving sampling and weighting method for the hyper reduction of nonlinear finite element dynamic models, *International Journal for Numerical Methods in Engineering* **102**, 1077–1110, 2015.
- [52] H. Finsberg, C. Xi, J. L. Tan, L. Zhong, M. Genet, J. Sundnes, L. C. Lee, and S. T. Wall, Efficient estimation of personalized biventricular mechanical function employing gradient-based optimization, *International Journal for Numerical Methods in Biomedical Engineering* **34**, e2982, 2018.
- [53] G. M. Fomovsky, A. D. Rouillard, and J. W. Holmes, Regional mechanics determine collagen fiber structure in healing myocardial infarcts, *Journal of Molecular and Cellular Cardiology* **52**, 1083–1090, 2012.
- [54] D. Fraccarollo, P. Galuppo, and J. Bauersachs, Novel therapeutic approaches to post-infarction remodelling, *Cardiovascular Research* **94**, 293–303, 2012.
- [55] J. S. Frank and G. A. Langer, The myocardial interstitium: its structure and its role in ionic exchange, *Journal of Cell Biology* **60**, 586–601, 1974.
- [56] T. Fritz, C. Wieners, G. Seemann, H. Steen, and O. Dössel, Simulation of the contraction of the ventricles in a human heart model including atria and pericardium, *Biomechanics and Modeling in Mechanobiology* **13**, 1–15, 2013.
- [57] K. Fujii, M. Ozaki, T. Yamagishi, K. Ishine, Y. Furutani, H. Nagano, K. Yamamoto, A. Saiki, and M. Matsuzaki, Effect of left ventricular contractile performance on passive left atrial filling clinical study using radionuclide angiography, *Clinical Cardiology* **17**, 258–262, 1994.
- [58] P. Gaudron, C. Eilles, I. Kugler, and G. Ertl, Progressive left ventricular dysfunction and remodeling after myocardial infarction. Potential mechanisms and early predictors, *Circulation* **87**, 755–63, 1993.
- [59] M. W. Gee, C. Reeps, H. H. Eckstein, and W. A. Wall, Prestressing in finite deformation abdominal aortic aneurysm simulation, *Journal of Biomechanics* **42**, 1732–1739, 2009.
- [60] M. W. Gee, C. Förster, and W. A. Wall, A computational strategy for prestressing patient-specific biomechanical problems under finite deformation, *International Journal for Numerical Methods in Biomedical Engineering* **26**, 52–72, 2010.
- [61] M. W. Gee, C. T. Kelley, and R. B. Lehoucq, Pseudo-transient continuation for nonlinear transient elasticity, *International Journal for Numerical Methods in Engineering* **78**, 1209–1219, 2009.
- [62] M. Genet, L. Lee, B. Baillargeon, J. Guccione, and E. Kuhl, Modeling pathologies of diastolic and systolic heart failure, *Annals of Biomedical Engineering* **44**, 112–127, 2016.

- [63] J.-F. Gerbeau, D. Lombardi, and E. Schenone, Reduced order model in cardiac electrophysiology with approximated lax pairs, *Advances in Computational Mathematics* **41**, 1103–1130, 2015.
- [64] J.-F. Gerbeau and D. Lombardi, Approximated lax pairs for the reduced order integration of nonlinear evolution equations, *Journal of Computational Physics* **265**, 246–269, 2014.
- [65] A. Gerbi, L. Dede, and A. Quarteroni, A monolithic algorithm for the simulation of cardiac electromechanics in the human left ventricle, *Mathematics in Engineering* **1**, 1–46, 2018.
- [66] C. Geuzaine and J.-F. Remacle, Gmsh: A 3-D finite element mesh generator with built-in pre-and post-processing facilities, *International Journal for Numerical Methods in Engineering* **79**, 1309–1331, 2009.
- [67] D. Gil, A. Borràs, R. Aris, M. Vázquez, P. Lafortune, G. Houzeaux, J. Aguado, M. Ballester, C. H. Li, and F. Carreras, What a difference in biomechanics cardiac fiber makes, In O. Camara, T. Mansi, M. Pop, K. Rhode, M. Sermesant, and A. Young (eds.), *Statistical Atlases and Computational Models of the Heart. Imaging and Modelling Challenges*, Volume 7746 of *Lecture Notes in Computer Science*, pages 253–260, Springer Berlin Heidelberg, 2013.
- [68] S. H. Gilbert, A. P. Benson, P. Li, and A. V. Holden, Regional localisation of left ventricular sheet structure: integration with current models of cardiac fibre, sheet and band structure, *European Journal of Cardio-Thoracic Surgery* **32**, 231–249, 2007.
- [69] O. Gjesdal, D. A. Bluemke, and J. A. Lima, Cardiac remodeling at the population level – risk factors, screening, and outcomes, *Nature Reviews Cardiology* **8**, 673–685, 2011.
- [70] S. A. Glantz, G. A. Misbach, W. Y. Moores, D. G. Mathey, J. Lekven, D. F. Stowe, W. W. Parmley, and J. V. Tyberg, The pericardium substantially affects the left ventricular diastolic pressure-volume relationship in the dog, *Circulation Research* **42**, 433–441, 1978.
- [71] D. D. Glower, J. A. Spratt, N. D. Snow, J. S. Kabas, J. W. Davis, C. O. Olsen, G. S. Tyson, D. C. Sabiston, and J. S. Rankin, Linearity of the frank-starling relationship in the intact heart: the concept of preload recruitable stroke work, *Circulation* **71**, 994–1009, 1985.
- [72] S. Göktepe, O. J. Abilez, K. K. Parker, and E. Kuhl, A multiscale model for eccentric and concentric cardiac growth through sarcomerogenesis, *Journal of Theoretical Biology* **265**, 433–442, 2010.
- [73] S. Göktepe, O. J. Abilez, and E. Kuhl, A generic approach towards finite growth with examples of athlete’s heart, cardiac dilation, and cardiac wall thickening, *Journal of the Mechanics and Physics of Solids* **58**, 1661–1680, 2010.
- [74] A. Griewank, Achieving logarithmic growth of temporal and spatial complexity in reverse automatic differentiation, *Optimization Methods and software* **1**, 35–54, 1992.

- [75] O. Gültekin, G. Sommer, and G. A. Holzapfel, An orthotropic viscoelastic model for the passive myocardium: continuum basis and numerical treatment, *Computer Methods in Biomechanics and Biomedical Engineering* **19**, 1647–1664, 2016.
- [76] K. B. Gupta, M. B. Ratcliffe, M. A. Fallert, L. H. Edmunds, and D. K. Bogen, Changes in passive mechanical stiffness of myocardial tissue with aneurysm formation, *Circulation* **89**, 2315–26, 1994.
- [77] M. Hadjicharalambous, L. Asner, R. Chabiniok, E. Sammut, J. Wong, D. Peressutti, E. Kerfoot, A. King, J. Lee, R. Razavi, N. Smith, G. Carr-White, and D. Nordsletten, Non-invasive model-based assessment of passive left-ventricular myocardial stiffness in healthy subjects and in patients with non-ischemic dilated cardiomyopathy, *Annals of Biomedical Engineering* **45**, 605–618, 2017.
- [78] S. A. Hall, C. G. Cigarroa, L. Marcoux, R. C. Risser, P. A. Grayburn, and E. J. Eichhorn, Time course of improvement in left ventricular function, mass and geometry in patients with congestive heart failure treated with beta-adrenergic blockade, *Journal of the American College of Cardiology* **25**, 1154–1161, 1995.
- [79] H. K. Hammond, F. C. White, V. Bhargava, and R. Shabetai, Heart size and maximal cardiac output are limited by the pericardium, *American Journal of Physiology–Heart and Circulatory Physiology* **263**, H1675–H1681, 1992.
- [80] E. Heiberg, J. Sjogren, M. Ugander, M. Carlsson, H. Engblom, and H. Arheden, Design and validation of segment–freely available software for cardiovascular image analysis, *BMC Medical Imaging* **10**, 1, 2010.
- [81] M. A. Heroux et al., An overview of the Trilinos project, *ACM Transactions on Mathematical Software (TOMS)* **31**, 397–423, 2005.
- [82] B. A. Hills and B. D. Butler, Phospholipids identified on the pericardium and their ability to impart boundary lubrication, *Annals of Biomedical Engineering* **13**, 573–586, 1985.
- [83] M. Hirschvogel, M. Bassilious, L. Jagschies, S. Wildhirt, and M. Gee, A monolithic 3d-0d coupled closed-loop model of the heart and the vascular system: Experiment-based parameter estimation for patient-specific cardiac mechanics, *International Journal for Numerical Methods in Biomedical Engineering* **33**, e2842, 2016.
- [84] J. W. Holmes, Candidate mechanical stimuli for hypertrophy during volume overload, *Journal of Applied Physiology* **97**, 1453–1460, 2004.
- [85] J. P. Holt, E. A. Rhode, H. Kines, and H. Ruth, Pericardial and ventricular pressure, *Circulation Research* **8**, 1171–1181, 1960.
- [86] J. P. Holt, The normal pericardium, *The American Journal of Cardiology* **26**, 455–465, 1970.
- [87] G. A. Holzapfel, *Nonlinear solid mechanics*, Volume 24, Wiley Chichester, 2000.

- [88] G. A. Holzapfel and R. W. Ogden, Constitutive modelling of passive myocardium: a structurally based framework for material characterization, *Philosophical Transactions of the Royal Society A: Mathematical, Physical and Engineering Sciences* **367**, 3445–3475, 2009.
- [89] J. M. Hörmann, C. Bertoglio, M. Kronbichler, M. R. Pfaller, R. Chabiniok, and W. A. Wall, An adaptive Hybridizable Discontinuous Galerkin approach for cardiac electrophysiology, *International Journal for Numerical Methods in Biomedical Engineering* **34**, e2959, 2018.
- [90] J. M. Hörmann, M. R. Pfaller, C. Bertoglio, L. Avena, and W. A. Wall, Automatic mapping of atrial fiber orientations for patient-specific modeling of cardiac electromechanics using image-registration, *submitted to International Journal for Numerical Methods in Biomedical Engineering*, 2018.
- [91] J. M. Hörmann. Multiscale electrophysiology simulation of human atria. Master’s thesis, Technical University of Munich, 2013.
- [92] J. M. Hörmann, C. Bertoglio, A. Nagler, M. R. Pfaller, F. Bourier, M. Hadamitzky, I. Deisenhofer, and W. A. Wall, Multiphysics modeling of the atrial systole under standard ablation strategies, *Cardiovascular Engineering and Technology* **8**, 205–218, 2017.
- [93] J. Humphrey and K. Rajagopal, A constrained mixture model for growth and remodeling of soft tissues, *Mathematical Models and Methods in Applied Sciences* **12**, 407–430, 2002.
- [94] S. A. Hunt et al., ACC/AHA 2005 guideline update for the diagnosis and management of chronic heart failure in the adult: A report of the American College of Cardiology/American Heart Association task force on practice guidelines developed in collaboration with the American College of Chest Physicians and the International Society for Heart and Lung Transplantation, *Circulation* **112**, e154–e235, 2005.
- [95] G. M. Hutchins and B. H. Bulkley, Infarct expansion versus extension: Two different complications of acute myocardial infarction, *The American Journal of Cardiology* **41**, 1127–1132, 1978.
- [96] P. A. Iaizzo, *Handbook of cardiac anatomy, physiology, and devices*, Springer Science & Business Media, 2015.
- [97] P. D. Jöbssis, H. Ashikaga, H. Wen, E. C. Rothstein, K. A. Horvath, E. R. McVeigh, and R. S. Balaban, The visceral pericardium: macromolecular structure and contribution to passive mechanical properties of the left ventricle, *American Journal of Physiology–Heart and Circulatory Physiology* **293**, H3379–H3387, 2007.
- [98] J. Kajstura et al., Cardiomyogenesis in the adult human heart, *Circulation Research* **107**, 305–315, 2010.
- [99] Y. Kanzaki, F. Terasaki, M. Okabe, S. Fujita, T. Katashima, K. Otsuka, and N. Ishizaka, Three-dimensional architecture of cardiomyocytes and connective tissue in human heart revealed by scanning electron microscopy, *Circulation* **122**, 1973–1974, 2010.

- [100] R. C. Kerckhoffs, M. L. Neal, Q. Gu, J. B. Bassingthwaite, J. H. Omens, and A. D. McCulloch, Coupling of a 3D finite element model of cardiac ventricular mechanics to lumped systems models of the systemic and pulmonic circulation, *Annals of Biomedical Engineering* **35**, 1–18, 2007.
- [101] R. C. Kerckhoffs, J. H. Omens, and A. D. McCulloch, A single strain-based growth law predicts concentric and eccentric cardiac growth during pressure and volume overload, *Mechanics Research Communications* **42**, 40–50, 2012.
- [102] G. Kerschen, J.-C. Golinval, A. F. Vakakis, and L. A. Bergman, The method of proper orthogonal decomposition for dynamical characterization and order reduction of mechanical systems: an overview, *Nonlinear Dynamics* **41**, 147–169, 2005.
- [103] D. Klepach, L. C. Lee, J. F. Wenk, M. B. Ratcliffe, T. I. Zohdi, J. L. Navia, G. S. Kassab, E. Kuhl, and J. M. Guccione, Growth and remodeling of the left ventricle: A case study of myocardial infarction and surgical ventricular restoration, *Mechanics Research Communications* **42**, 134–141, 2012.
- [104] K. Komamura, R. P. Shannon, T. Ihara, Y. T. Shen, I. Mirsky, S. P. Bishop, and S. F. Vatner, Exhaustion of Frank-Starling mechanism in conscious dogs with heart failure, *American Journal of Physiology—Heart and Circulatory Physiology* **265**, H1119–H1131, 1993.
- [105] M. A. Konstam, D. G. Kramer, A. R. Patel, M. S. Maron, and J. E. Udelson, Left ventricular remodeling in heart failure, *JACC: Cardiovascular Imaging* **4**, 98–108, 2011.
- [106] A. Krishnamurthy, C. T. Villongco, J. Chuang, L. R. Frank, V. Nigam, E. Belezouli, P. Stark, D. E. Krummen, S. Narayan, J. H. Omens, et al., Patient-specific models of cardiac biomechanics, *Journal of Computational Physics* **244**, 4–21, 2013.
- [107] W. Kroon, T. Delhaas, T. Arts, and P. Bovendeerd, Computational modeling of volumetric soft tissue growth: application to the cardiac left ventricle, *Biomechanics and Modeling in Mechanobiology* **8**, 301–309, 2009.
- [108] P. Krysl, S. Lall, and J. E. Marsden, Dimensional model reduction in non-linear finite element dynamics of solids and structures, *International Journal for Numerical Methods in Engineering* **51**, 479–504, 2001.
- [109] K. Kunisch and S. Volkwein, Control of the Burgers equation by a reduced-order approach using proper orthogonal decomposition, *Journal of Optimization Theory and Applications* **102**, 345–371, 1999.
- [110] K. Kunisch and S. Volkwein, Galerkin proper orthogonal decomposition methods for a general equation in fluid dynamics, *SIAM Journal on Numerical Analysis* **40**, 492–515, 2002.
- [111] A. Laadhari, R. Ruiz-Baier, and A. Quarteroni, Fully eulerian finite element approximation of a fluid-structure interaction problem in cardiac cells, *International Journal for Numerical Methods in Engineering* **96**, 712–738, 2013.

- [112] M. A. Laflamme and C. E. Murry, Heart regeneration, *Nature* **473**, 326–335, 2011.
- [113] M. A. Laflamme, D. Myerson, J. E. Saffitz, and C. E. Murry, Evidence for cardiomyocyte repopulation by extracardiac progenitors in transplanted human hearts, *Circulation Research* **90**, 634–640, 2002.
- [114] S. Land and S. A. Niederer, Influence of atrial contraction dynamics on cardiac function, *International Journal for Numerical Methods in Biomedical Engineering* **34**, e2931, 2017.
- [115] T. Lassila, A. Manzoni, A. Quarteroni, and G. Rozza, A reduced computational and geometrical framework for inverse problems in hemodynamics, *International Journal for Numerical Methods in Biomedical Engineering* **29**, 741–776, 2013.
- [116] J. M. Lee and D. R. Boughner, Mechanical properties of human pericardium. Differences in viscoelastic response when compared with canine pericardium, *Circulation Research* **57**, 475–481, 1985.
- [117] L. Lee, M. Genet, G. Acevedo-Bolton, K. Ordovas, J. Guccione, and E. Kuhl, A computational model that predicts reverse growth in response to mechanical unloading, *Biomechanics and Modeling in Mechanobiology* **14**, 217–229, 2015.
- [118] L. Lee, J. Sundnes, M. Genet, J. Wenk, and S. Wall, An integrated electromechanical-growth heart model for simulating cardiac therapies, *Biomechanics and Modeling in Mechanobiology*, 1–13, 2015.
- [119] L. Lee, J. Sundnes, M. Genet, J. Wenk, and S. Wall, An integrated electromechanical-growth heart model for simulating cardiac therapies, *Biomechanics and Modeling in Mechanobiology*, 1–13, 2015.
- [120] K. Levenberg, A method for the solution of certain non-linear problems in least squares, *Quarterly of Applied Mathematics* **2**, 164–168, 1944.
- [121] Y. Liang, H. Lee, S. Lim, W. Lin, K. Lee, and C. Wu, Proper orthogonal decomposition and its applications – Part I: Theory, *Journal of Sound and Vibration* **252**, 527–544, 2002.
- [122] B. H. Lorell and B. A. Carabello, Left ventricular hypertrophy: Pathogenesis, detection, and prognosis, *Circulation* **102**, 470–479, 2000.
- [123] J. Lumens, T. Delhaas, B. Kirn, and T. Arts, Three-wall segment (triseg) model describing mechanics and hemodynamics of ventricular interaction, *Annals of Biomedical Engineering* **37**, 2234–2255, 2009.
- [124] E. Maksuti, A. Bjllmark, and M. Broom, Modelling the heart with the atrioventricular plane as a piston unit, *Medical Engineering & Physics* **37**, 87–92, 2015.
- [125] T. Mansi, *Image-based physiological and statistical models of the heart: application to tetralogy of Fallot*, Theses, École Nationale Supérieure des Mines de Paris, 2010.

- [126] S. Marchesseau, H. Delingette, M. Sermesant, and N. Ayache, Fast parameter calibration of a cardiac electromechanical model from medical images based on the unscented transform, *Biomechanics and Modeling in Mechanobiology* **12**, 815–831, 2013.
- [127] D. W. Marquardt, An algorithm for least-squares estimation of nonlinear parameters, *Journal of the Society for Industrial and Applied Mathematics* **11**, 431–441, 1963.
- [128] F. H. Martini, M. J. Timmons, and R. B. Tallitsch, *Human Anatomy*, number 8, Pearson Education, 2015.
- [129] J. R. McGarvey, D. Mojsejenko, S. M. Dorsey, A. Nikou, J. A. Burdick, J. H. G. III, B. M. Jackson, J. J. Pilla, R. C. Gorman, and J. F. Wenk, Temporal changes in infarct material properties: An in vivo assessment using magnetic resonance imaging and finite element simulations, *The Annals of Thoracic Surgery* **100**, 582–589, 2015.
- [130] R. G. McKay, M. A. Pfeffer, R. C. Pasternak, J. E. Markis, P. C. Come, S. Nakao, J. D. Alderman, J. J. Ferguson, R. D. Safian, and W. Grossman, Left ventricular remodeling after myocardial infarction: a corollary to infarct expansion., *Circulation* **74**, 693–702, 1986.
- [131] C. Mekkaoui, S. Huang, H. H. Chen, G. Dai, T. G. Reese, W. J. Kostis, A. Thiagalingam, P. Maurovich-Horvat, J. N. Ruskin, U. Hoffmann, M. P. Jackowski, and D. E. Sosnovik, Fiber architecture in remodeled myocardium revealed with a quantitative diffusion CMR tractography framework and histological validation, *Journal of Cardiovascular Magnetic Resonance* **14**, 70, 2012.
- [132] R. Milani, A. Quarteroni, and G. Rozza, Reduced basis method for linear elasticity problems with many parameters, *Computer Methods in Applied Mechanics and Engineering* **197**, 4812–4829, 2008.
- [133] P. Moireau, C. Bertoglio, N. Xiao, C. Figueroa, C. Taylor, D. Chapelle, and J.-F. Gerbeau, Sequential identification of boundary support parameters in a fluid-structure vascular model using patient image data, *Biomechanics and Modeling in Mechanobiology* **12**, 475–496, 2013.
- [134] P. Moireau, N. Xiao, M. Astorino, C. A. Figueroa, D. Chapelle, C. A. Taylor, and J.-F. Gerbeau, External tissue support and fluid–structure simulation in blood flows, *Biomechanics and Modeling in Mechanobiology* **11**, 1–18, 2012.
- [135] R. Molléro, X. Pennec, H. Delingette, A. Garny, N. Ayache, and M. Sermesant, Multifidelity-CMA: a multifidelity approach for efficient personalisation of 3d cardiac electromechanical models, *Biomechanics and Modeling in Mechanobiology* **17**, 285–300, 2018.
- [136] M. J. Moulton, B. D. Hong, and T. W. Secomb, Simulation of left ventricular dynamics using a low-order mathematical model, *Cardiovascular Engineering and Technology* **8**, 480–494, 2017.

- [137] A. Nagler, C. Bertoglio, M. Ortiz, and W. A. Wall, A spatially varying mathematical representation of the biventricular cardiac fiber architecture, Technical report, Institute for Computational Mechanics, Technical University of Munich, 2016.
- [138] A. Nagler, C. Bertoglio, C. T. Stoeck, S. Kozerke, and W. A. Wall, Maximum likelihood estimation of cardiac fiber bundle orientation from arbitrarily spaced diffusion weighted images, *Medical Image Analysis* **39**, 56–77, 2017.
- [139] N. M. Newmark, A method of computation for structural dynamics, *Journal of the engineering mechanics division* **85**, 67–94, 1959.
- [140] A. Nikou, R. C. Gorman, and J. F. Wenk, Sensitivity of left ventricular mechanics to myofiber architecture: A finite element study, *Proceedings of the Institution of Mechanical Engineers, Part H: Journal of Engineering in Medicine* **230**, 594–598, 2016.
- [141] D. Nordsletten, S. Niederer, M. Nash, P. Hunter, and N. Smith, Coupling multi-physics models to cardiac mechanics, *Progress in Biophysics and Molecular Biology* **104**, 77–88, 2011.
- [142] G. Olivetti, J. M. Capasso, E. H. Sonnenblick, and P. Anversa, Side-to-side slippage of myocytes participates in ventricular wall remodeling acutely after myocardial infarction in rats., *Circulation Research* **67**, 23–34, 1990.
- [143] S. Pagani, A. Manzoni, and A. Quarteroni, Numerical approximation of parametrized problems in cardiac electrophysiology by a local reduced basis method, *Computer Methods in Applied Mechanics and Engineering* **340**, 530–558, 2018.
- [144] A. Palit, S. K. Bhudia, T. N. Arvanitis, G. A. Turley, and M. A. Williams, In vivo estimation of passive biomechanical properties of human myocardium, *Medical & Biological Engineering & Computing*, 2018.
- [145] F. Pashakhanloo, D. A. Herzka, S. Mori, M. Zviman, H. Halperin, N. Gai, D. A. Bluemke, N. A. Trayanova, and E. R. McVeigh, Submillimeter diffusion tensor imaging and late gadolinium enhancement cardiovascular magnetic resonance of chronic myocardial infarction, *Journal of Cardiovascular Magnetic Resonance* **19**, 9, 2017.
- [146] B. Peherstorfer, K. Willcox, and M. Gunzburger, Survey of multifidelity methods in uncertainty propagation, inference, and optimization, *SIAM Review* **60**, 550–591, 2018.
- [147] M. R. Pfaller, M. Cruz Varona, J. Lang, C. Bertoglio, and W. A. Wall, Parametric model order reduction and its application to inverse analysis of large nonlinear coupled cardiac problems, *submitted to International Journal for Numerical Methods in Biomedical Engineering*, eprint [arXiv:1810.12033](https://arxiv.org/abs/1810.12033), 2018.
- [148] M. R. Pfaller, J. M. Hörmann, M. Weigl, A. Nagler, R. Chabiniok, C. Bertoglio, and W. A. Wall, The importance of the pericardium for cardiac biomechanics: from physiology to computational modeling, *Biomechanics and Modeling in Mechanobiology* **18**, 503–529, 2019.

- [149] M. A. Pfeffer and E. Braunwald, Ventricular remodeling after myocardial infarction. experimental observations and clinical implications., *Circulation* **81**, 1161–72, 1990.
- [150] A. Popp, *Mortar Methods for Computational Contact Mechanics and General Interface Problems*, Dissertation, Technical University of Munich, 2012.
- [151] S. W. Rabkin, Epicardial fat: properties, function and relationship to obesity, *Obesity Reviews* **8**, 253–261, 2007.
- [152] S. Rabkin and P. Hsu, Mathematical and mechanical modeling of stress-strain relationship of pericardium, *American Journal of Physiology – Legacy Content* **229**, 896–900, 1975.
- [153] E. K. Rodriguez, A. Hoger, and A. D. McCulloch, Stress-dependent finite growth in soft elastic tissues, *Journal of Biomechanics* **27**, 455–467, 1994.
- [154] T. J. Ryan et al., ACC/AHA guidelines for the management of patients with acute myocardial infarction: a report of the american college of cardiology/american heart association task force on practice guidelines (committee on management of acute myocardial infarction), *Journal of the American College of Cardiology* **28**, 1328–1419, 1996.
- [155] M. S. Sacks, Incorporation of experimentally-derived fiber orientation into a structural constitutive model for planar collagenous tissues, *Journal of Biomechanical Engineering* **125**, 280–287, 2003.
- [156] J. Sainte-Marie, D. Chapelle, R. Cimrman, and M. Sorine, Modeling and estimation of the cardiac electromechanical activity, *Computers & Structures* **84**, 1743–1759, 2006.
- [157] W. P. Santamore, M. S. Constantinescu, D. Bogen, and W. E. Johnston, Nonuniform distribution of normal pericardial fluid, *Basic Research in Cardiology* **85**, 541–549, 1990.
- [158] A. Santiago, M. Zavala-Ak, J. Aguado-Sierra, R. Doste, S. Gmez, R. Ars, J. C. Cajas, E. Casoni, and M. Vzquez, Fully coupled fluid-electro-mechanical model of the human heart for supercomputers, *International Journal for Numerical Methods in Biomedical Engineering*, 2018.
- [159] W. H. A. Schilders and A. Lutowska, pages 1–49, *A Novel Approach to Model Order Reduction for Coupled Multiphysics Problems*, A. Quarteroni and G. Rozza (eds.), Springer International Publishing, 2014.
- [160] M. Sermesant, P. Moireau, O. Camara, J. Sainte-Marie, R. Andriantsimiavona, R. Cimrman, D. Hill, D. Chapelle, and R. Razavi, Cardiac function estimation from MRI using a heart model and data assimilation: Advances and difficulties, *Medical Image Analysis* **10**, 642–656, 2006.
- [161] M. Sermesant, R. Chabiniok, P. Chinchapatnam, T. Mansi, F. Billet, P. Moireau, J. Peyrat, K. Wong, J. Relan, K. Rhode, M. Ginks, P. Lambiase, H. Delingette, M. Sorine, C. Rinaldi, D. Chapelle, R. Razavi, and N. Ayache, Patient-specific electromechanical models of the heart for the prediction of pacing acute effects in CRT: A preliminary clinical validation, *Medical Image Analysis* **16**, 201–215, 2012.

- [162] R. Shabetai, *The Pericardium*, Volume 249 of *Developments in Cardiovascular Medicine*, Springer, 2003.
- [163] Y. Shi, P. Lawford, and R. Hose, Review of zero-D and 1-D models of blood flow in the cardiovascular system, *BioMedical Engineering Online* **10**, 33, 2011.
- [164] M. L. Simoons, P. W. Serruys, M. van den Brand, J. Res, F. W. Verheugt, X. H. Krauss, W. J. Remme, F. Bär, C. d. Zwaan, A. v. d. Laarse, F. Vermeer, and J. Lubsen, Early thrombolysis in acute myocardial infarction: Limitation of infarct size and improved survival, *Journal of the American College of Cardiology* **7**, 717–728, 1986.
- [165] O. A. Smiseth, M. A. Fraiss, I. Kingma, E. R. Smith, and J. V. Tyberg, Assessment of pericardial constraint in dogs, *Circulation* **71**, 158–64, 1985.
- [166] G. Sommer, A. J. Schriefl, M. Andr, M. Sacherer, C. Viertler, H. Wolinski, and G. A. Holzapfel, Biomechanical properties and microstructure of human ventricular myocardium, *Acta Biomaterialia* **24**, 172–192, 2015.
- [167] D. H. Spodick, The normal and diseased pericardium: Current concepts of pericardial physiology, diagnosis and treatment, *Journal of the American College of Cardiology* **1**, 240–251, 1983.
- [168] D. H. Spodick, *The pericardium: a comprehensive textbook*, Volume 27, Informa Health Care, 1996.
- [169] S. Standring, *Gray's Anatomy: The Anatomical Basis of Clinical Practice*, Volume 41, Elsevier Health Sciences, 2015.
- [170] F. Sudak, Intrapericardial and intracardiac pressures and the events of the cardiac cycle in mustelus canis (mitchill), *Comparative Biochemistry and Physiology* **14**, 689–705, 1965.
- [171] J. Sutton and D. G. Gibson, Measurement of postoperative pericardial pressure in man., *British Heart Journal* **39**, 1–6, 1977.
- [172] M. S. J. Sutton, M. A. Pfeffer, L. Moye, T. Plappert, J. L. Rouleau, G. Lamas, J. Rouleau, J. O. Parker, M. O. Arnold, B. Sussex, E. Braunwald, and for the SAVE Investigators, Cardiovascular death and left ventricular remodeling two years after myocardial infarction: Baseline predictors and impact of long-term use of captopril: Information from the survival and ventricular enlargement (save) trial, *Circulation* **96**, 3294–3299, 1997.
- [173] B. Swynghedaww, Molecular mechanisms of myocardial remodeling, *Physiological Reviews* **79**, 215–262, 1999.
- [174] C. A. Taylor, T. J. Hughes, and C. K. Zarins, Finite element modeling of blood flow in arteries, *Computer Methods in Applied Mechanics and Engineering* **158**, 155–196, 1998.
- [175] K. Thygesen, J. S. Alpert, and H. D. White, Universal definition of myocardial infarction, *Journal of the American College of Cardiology* **50**, 2173–2195, 2007.

- [176] A. Tsamis, A. Cheng, T. C. Nguyen, F. Langer, D. C. Miller, and E. Kuhl, Kinematics of cardiac growth: In vivo characterization of growth tensors and strains, *Journal of the Mechanical Behavior of Biomedical Materials* **8**, 165–177, 2012.
- [177] J. V. Tyberg, G. C. Taichman, E. R. Smith, N. W. Douglas, O. A. Smiseth, and W. J. Keon, The relationship between pericardial pressure and right atrial pressure: an intraoperative study, *Circulation* **73**, 428–32, 1986.
- [178] S. Ubbink, P. Bovendeerd, T. Delhaas, T. Arts, and F. van de Vosse, Towards model-based analysis of cardiac MR tagging data: Relation between left ventricular shear strain and myofiber orientation, *Medical Image Analysis* **10**, 632–641, 2006.
- [179] S. Uribe, T. Tangchaoren, V. Parish, I. Wolf, R. Razavi, G. Greil, and T. Schaeffter, Volumetric Cardiac Quantification by Using 3D Dual-Phase Whole-Heart MR Imaging, *Radiology* **248**, 606–614, 2008.
- [180] J. C. Walker, J. M. Guccione, Y. Jiang, P. Zhang, A. W. Wallace, E. W. Hsu, and M. B. Ratcliffe, Helical myofiber orientation after myocardial infarction and left ventricular surgical restoration in sheep, *Journal of Thoracic and Cardiovascular Surgery* **129**, 382–390, 2005.
- [181] W. A. Wall et al., Baci: a parallel multiphysics simulation environment, Technical report, Technical report, Institute for Computational Mechanics, Technische Universität München, 2018.
- [182] N. Westerhof, J.-W. Lankhaar, and B. E. Westerhof, The arterial windkessel, *Medical & Biological Engineering & Computing* **47**, 131–141, 2008.
- [183] H. D. White, R. M. Norris, M. A. Brown, P. W. Brandt, R. M. Whitlock, and C. J. Wild, Left ventricular end-systolic volume as the major determinant of survival after recovery from myocardial infarction., *Circulation* **76**, 44–51, 1987.
- [184] H. D. White and D. P. Chew, Acute myocardial infarction, *The Lancet* **372**, 570–584, 2008.
- [185] L. Wiechert, R. Metzke, and W. A. Wall, Modeling the mechanical behavior of lung tissue at the microlevel, *Journal of Engineering Mechanics* **135**, 434–438, 2009.
- [186] R. Willenheimer, C. Cline, L. Erhardt, and B. Israelsson, Left ventricular atrioventricular plane displacement: an echocardiographic technique for rapid assessment of prognosis in heart failure, *Heart* **78**, 230–236, 1997.
- [187] C. M. Witzenburg and J. W. Holmes, A comparison of phenomenologic growth laws for myocardial hypertrophy, *Journal of Elasticity*, 1–25, 2017.
- [188] K. C. Wong, F. Billet, T. Mansi, R. Chabiniok, M. Sermesant, H. Delingette, and N. Ayaiche, Cardiac motion estimation using a proactive deformable model: evaluation and sensitivity analysis, In *International Workshop on Statistical Atlases and Computational Models of the Heart*, pages 154–163. Springer, 2010.

- [189] S. P. Wong, J. K. French, A.-M. Lydon, S. O. Manda, W. Gao, N. G. Ashton, and H. D. White, Relation of left ventricular sphericity to 10-year survival after acute myocardial infarction, *The American Journal of Cardiology* **94**, 1270–1275, 2004.
- [190] E. X. Wu, Y. Wu, J. M. Nicholls, J. Wang, S. Liao, S. Zhu, C.-P. Lau, and H.-F. Tse, MR diffusion tensor imaging study of postinfarct myocardium structural remodeling in a porcine model, *Magnetic Resonance in Medicine* **58**, 687–695, 2007.
- [191] M. Xie, J. S. Burchfield, and J. A. Hill, Pathological ventricular remodeling: Therapies: Part 2 of 2, *Circulation* **128**, 1021–1030, 2013.
- [192] F. C. Yin, R. K. Strumpf, P. H. Chew, and S. L. Zeger, Quantification of the mechanical properties of noncontracting canine myocardium under simultaneous biaxial loading, *Journal of Biomechanics* **20**, 577–589, 1987.
- [193] Y. Yue and K. Meerbergen, Accelerating optimization of parametric linear systems by model order reduction, *SIAM Journal on Optimization* **23**, 1344–1370, 2013.

Verzeichnis der betreuten Studienarbeiten

Im Rahmen dieser Dissertation entstanden am Lehrstuhl für Numerische Mechanik in den Jahren von 2014 bis 2018 unter wesentlicher wissenschaftlicher, fachlicher und inhaltlicher Anleitung des Autors die im Folgenden aufgeführten studentischen Arbeiten. Der Autor dankt allen Studierenden für Ihr Engagement bei der Unterstützung dieser wissenschaftlichen Arbeit.

Student(in)	Studienarbeit
Jonas Schollenberger	<i>A Lumped Parameter Model of Cerebral Blood Flow Regulation: Applications to Simulation of Carotid Endarterectomy</i> , Masterarbeit, 2015
Christina Insam	<i>A Reduced-Order Model of Left Ventricular Mechanics using a Prolate Spheroid Geometry</i> , Bachelorarbeit, 2015
Martina Weigl	<i>Segmentation of a Four-Chamber Cardiac Geometry und Implementation of a Laplace Fiber Lifting Class in Python</i> , Wissenschaftliche Hilfskraft, 2015–2016, eingeflossen in Kapitel 2.3.1 , 2.4.1 und 3
Sebastian Kaltenbach	<i>Reduced-Order Mathematical Modeling of Cardiac Growth and Remodeling</i> , Semestarbeit, 2016
Janina Datz	<i>Estimation of Cardiac Muscle Fiber Architecture from Diffusion-Weighted Magnetic Resonance Imaging</i> , Bachelorarbeit, 2016
Mirjam Bastian	<i>Influence of Pericardial Boundary Conditions on Systolic Cardiac Function in Mechanical Simulations</i> , Semestarbeit, 2017
Johannes Lang	<i>Projection-based Parametric Model Order Reduction for 3D-0D Coupled Cardiac Mechanics</i> , Masterarbeit, 2017, eingeflossen in Kapitel 4
Magnus Mechler	<i>Projection-based Hyper-reduction for 3D-0D Coupled Cardiovascular Mechanics</i> , Masterarbeit, 2018
Maximilian Gruber	<i>Electrophysiological Simulation of Atrial Fibrillation</i> , Semestarbeit, 2018
Lukas Kühle	<i>Implementation and Verification of a Gauß-point-based Fiber Formulation</i> , Bachelorarbeit, 2018
Amadeus Gebauer	<i>Growth and Remodeling for Cardiac Mechanics Simulations</i> , Masterarbeit, 2019